Quantum Sensing for Low-Light Imaging

Savannah Lea Cuozzo

Tampa, Florida

Master of Science, College of William & Mary, 2019
Bachelor of Science, University of South Florida, 2017

A Dissertation presented to the Graduate Faculty
of The College of William & Mary in Candidacy for the Degree of
Doctor of Philosophy

Department of Physics

College of William & Mary
May 2022

APPROVAL PAGE

This Dissertation is submitted in partial fulfillment of
the requirements for the degree of

Doctor of Philosophy

Savannah Lea Cuozzo

Approved by the Committee March 2022

Committee Chair
Eugeniy E. Mikhailov, Associate Professor, Physics
College of William & Mary

Irina Novikova, Professor, Physics
College of William & Mary

Todd Averett, Professor, Physics
College of William & Mary

William Cooke, Professor, Physics
College of William & Mary

Lior Cohen, Research Assistant Professor, Electrical, Computer
and Energy Engineering
University of Colorado, Boulder

ABSTRACT

In high-precision optical measurements, noise due to quantum fluctuations in the amplitude and phase of the probing field becomes the limiting factor in detection sensitivity. While this quantum noise is fundamental and not a result of detection, it is possible to engineer a quantum state that has reduced noise in either amplitude or phase (at the cost of increasing noise in the other) called a quadrature-squeezed state. In this dissertation, we study the use of quadrature-squeezed vacuum states for low-light imaging and develop a quantum detection method to measure the spatial dependence of the quantum noise using a camera instead of the traditional homodyne detection. Our novel quantum imaging scheme paves the way for ultra-low-light imaging due to the inherently few photons in the squeezed vacuum state. We also expand the method beyond camera limitations using single-pixel imaging techniques, making the detection method accessible to a broad range of wavelengths where quantum-limited cameras may be difficult to find.

TABLE OF CONTENTS

ACKNOWLEDGMENTS

I am incredibly grateful for all the people who have supported me throughout the years.

First, I would like to thank my adviser, Eugeniy Mikhailov, for his countless hours of teaching and mentoring. He has not only made me a better scientist, but a better human. I also want to thank Irina Novikova for for her constant guidance and strong example of female leadership in physics.

I want to thank the fellow members of the quantum optics group at William & Mary. I will never forget the patient guidance from Nik Prajapati, Scott Madaras, and Jason Creeden. Thank you for teaching me the ropes when I was just starting out! I also want to thank Ziqi Niu, Nic DeStefano, Charris Gabaldon, and Rob Behary for making the lab a fun and collaborative place to work.

I cannot fail to recognize the impact my theory collaborators at Louisiana State University have had on my development as a scientist. I thank Elisha Matekole, Narayan Bhusal, Pratik Barge, Hwang Lee, Lior Cohen, and the late Jonathan Dowling for the many hours of helpful scientific discussion. Being your colleague has been a great privilege.

Finally, I would like to thank my family and friends for their love and encouragement throughout the years. Thank you to my parents for giving all the opportunities life has to offer, my sister for always rooting for me, and my dear friends at WCC for their uplifting spirit. Last but not least, I want to thank my husband, Joe. Without his unwavering support and confidence in me, I would never have come this far.

Dedicated to my husband Joe.

LIST OF FIGURES

QUANTUM SENSING FOR LOW-LIGHT IMAGING

CHAPTER 1

Introduction

1.1 The Effects of Quantum Noise on Measurements and What We Can Do About It

The task of understanding noise in an experiment always poses a challenge to scientists. While in the past, most measurements were limited by the noise of the detectors, as the precision of sensors and measurements have improved, we have run into noise limits that are imposed by quantum mechanics. For optical measurements, this quantum noise is inherent to our probing field. This is not something that can be overcome with better detectors or any classical noise suppression, but rather is deeply tied to the quantum-mechanical nature of light. This intrinsic noise originates from the uncertainty principle that constrains the precision of measuring the amplitude and phase of the light - similar to the position/momentum uncertainty relationship in a simple harmonic oscillator [4, 5, 6]. To circumvent this apparent limit, scientists have developed ways to manipulate the noise distribution so that it can be suppressed in either the amplitude or the phase (at the cost of increasing the noise in the other) [7]. This noise manipulation, known as squeezing,

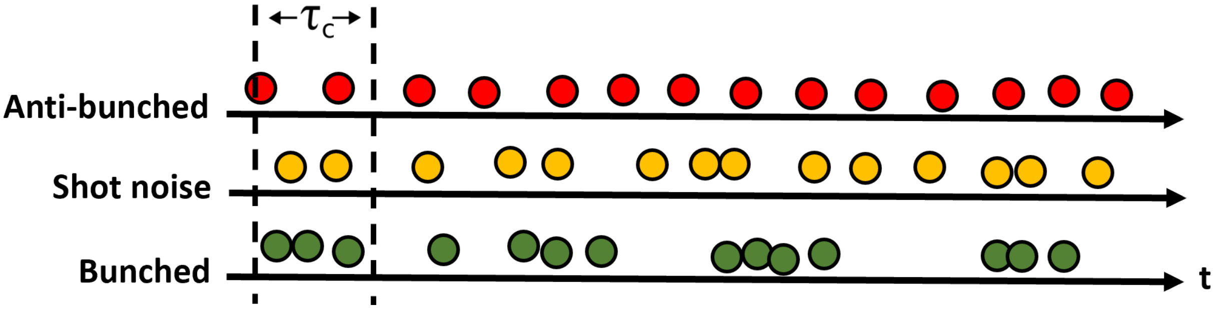

FIG. 1.1: Example of photons statistics over a characteristic time, τ_c. Here the x-axis represents time and each circle represents a photon arriving to the detector at a given time, t.

proves very useful for applications such as precision interferometry [8, 9], where the phase sensitivity is limited by the shot noise of the vacuum, and imaging [10, 11, 12, 13], where the noise in the image is often limited by the shot noise statistics of the illuminating field.

1.2 A Brief Historical Overview of Squeezing

While many optical processes can be described using a classical or semi-classical approach, for a electromagnetic field containing only a few photons the quantum nature is more apparent - the statistical fluctuations in the light now become relevant. Hanbury-Brown and Twiss developed an understanding of intensity correlations [14, 4] (to use for stellar interferometry) by monitoring the photo-currents from two detectors illuminated with the same light source. This demonstrated how thermal photons were bunched and opened the door to further exploration of photon statistics/photon counting of light. Once lasers became available, it was shown that lasers do not exhibit bunching but instead obey Poissonian statistics. As a result, the laser intensity will always have a certain amount of noise associated with it. This noise was dubbed ”shot noise” [4].

Roy J. Glauber’s theory of optical coherence [15] predicted that in addition to super-Poissonian statistics (bunching) of the thermal light there should also be photon anti-bunching – giving rise to sub-Poissonian statistics. This meant that the fluctuations in the photo-current from the detector should be *less* than the shot noise. Figure 1.1 shows a qualitative example of shot noise, bunched, and anti-bunched statistics as a function of time. Photon anti-bunching can not be understood with a classical theory since, to produce these types of statistics, you would need negative field amplitude probabilities which are unphysical [4]. This non-classical feature was demonstrated by Kimble et al [16] in 1977 using resonance fluorescence from a two-level atom and sparked interest in a new quantum state where the noise distribution could be manipulated: the squeezed state [4].

Over the next decade, theoretical advances in understanding and generating these squeezed states took off. In 1979, Yuen [17] outlined a way to generate two-photon states using four-wave mixing. A few years later, Caves showed how using squeezing could improve interferometric measurements [18], followed by a comprehensive review by Walls [19].

The experimental demonstration soon followed. Slusher generated squeezed states using four-wave mixing in a cavity [20] and Shelby demonstrated squeezed states in an optical fiber [21]. Kimble's group was able to obtain some of the largest amounts of early squeezing (-4dBs below shot noise) using an optical parametric oscillator (OPO) [22]. The same group also showed interferometric improvement using squeezed states [23]. Squeezing has also been generated in atomic systems. Slusher demonstrated squeezing using a four-wave mixing process in sodium [24], and Lett's group demonstrated four-wave mixing in rubidium [25, 26]. Of course, further developments have been made throughout the past decades [27, 28, 29, 30], with the highest reported squeezing being -15 dBs below shot noise [31]. These quantum states have been used to develop secure optical communication channels [32, 33, 34], sub-shot-noise imaging techniques [12], and high precision detectors like the gravitation wave detector LIGO [9].

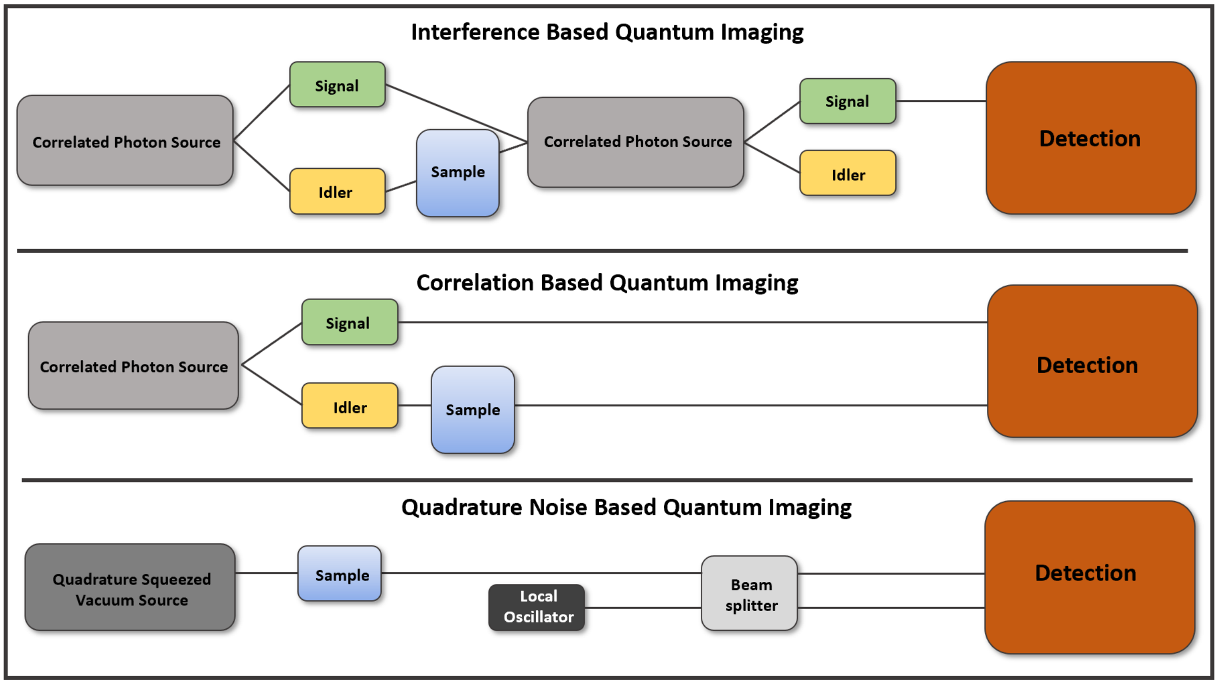

FIG. 1.2: Examples of standard quantum imaging schemes adapted from [1] compared to the quadrature noise based imaging scheme presented in this thesis.

1.3 Quantum Imaging

For the past few decades, the notion of exploiting the quantum properties of light has gained traction in the quantum optics world as a way of imaging beyond the shot noise limit [35, 1]. Up to this point, several different imaging schemes have been explored. Figure 1.2 shows a simple schematic of three types of imaging that have been studied.

1) *Correlation-based Imaging* utilizes twin photons. These twin photons are produced via two-mode squeezing where a single photon is down converted into two intensity correlated photons. In this case, one beam interrogates the object, and the other acts as a reference. When the two beams are subtracted the image that is formed contains sub-shot-noise statistics. While there are many ways to exploit these correlated photons [36, 37, 26, 38].

2) *Interference-based Imaging* also uses correlated photons as the basis of the imaging scheme. However, in this case, one of the correlated photons interacts with the object and

is then recombined with its partner using a linear or nonlinear beam splitter. Then one of the ports is monitored using a camera and the object can be imaged [39, 11, 40].

Many variations on these schemes exist, however, there have not been many studies using the change in quantum quadrature variance as a means of imaging. Throughout this dissertation, I will explore the particular case of using a single-mode squeezing vacuum as the primary probe and study the spatial dependence of the quadrature noise variance as a new way of imaging [41, 42]. While the method I will present does not create shot-noise-limited images, it does allow us to work around technical issues of camera dark noise (see Chapter 4), and when using a single-pixel scheme extract phase information from the probed object (see Chapter 5).

1.4 Outline of Dissertation

In Chapter 2, I will first give an overview of the theoretical framework needed to understand quantum and nonlinear optical interactions. Then, in Chapter 3 review standard detection schemes and methods for manipulating the quantum noise statistics of light. I will then move on to Chapter 4, the work done in quadrature imaging, and discuss how we use quadrature noise measurements to image using very few photons and end discussing imaging in Chapter 5 by presenting the work done towards understanding the mode structure of the squeezed light via single-pixel imaging. Finally, in Chapter 6.1, I will discuss the advantages of dispersion-enhanced optical cavity for inertial sensing applications and the work toward implementation.

CHAPTER 2

Theoretical Description of EM Fields

2.1 Classical Description of an Electromagnetic Field

We can describe the nature of light propagating through a medium using Maxwell's equations which gives us a relationship between the electric field, $\vec{\boldsymbol{E}}$, and magnetic field, $\vec{\boldsymbol{B}}$,

$$\nabla \cdot \vec{\boldsymbol{B}} = 0 \tag{2.1a}$$

$$\nabla \cdot \vec{\boldsymbol{E}} = \frac{\rho}{\epsilon_0} \tag{2.1b}$$

$$\nabla \times \vec{\boldsymbol{E}} = -\frac{\partial \vec{\boldsymbol{B}}}{\partial t} \tag{2.1c}$$

$$\nabla \times \vec{\boldsymbol{B}} = \mu_0 \epsilon_0 \frac{\partial \vec{\boldsymbol{E}}}{\partial t} + \mu_0 \vec{\boldsymbol{J}}, \tag{2.1d}$$

where μ_0 is the magnetic permeability of vacuum, ϵ_0 is the electric permittivity of vacuum, ρ is the charge density, and $\vec{\boldsymbol{J}}$ is the current density. Assuming the field is constrained to a one-dimensional cavity in the z-direction, where $\vec{\boldsymbol{E}}$ is polarized in the x-direction and $\vec{\boldsymbol{B}}$

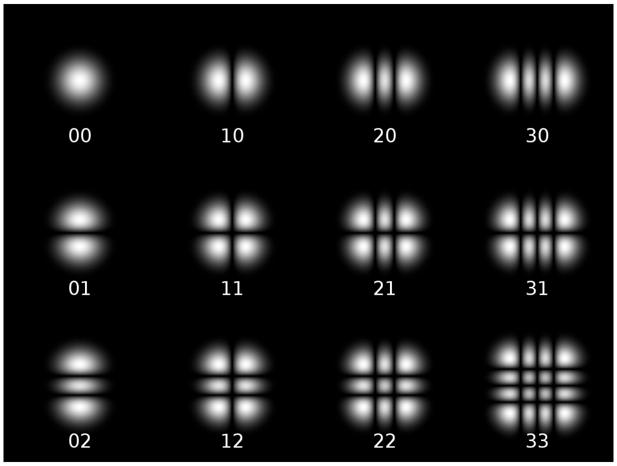

FIG. 2.1: Examples of the HG modes taken from [2].

is in the y-direction,

$$E_x(z,t) = \left(\frac{2\omega^2}{V\epsilon_0}\right)^{1/2} q(t)\sin(kz) \tag{2.2a}$$

$$B_y(z,t) = \frac{\mu_0\epsilon_0}{k}\left(\frac{2\omega^2}{V\epsilon_0}\right)^{1/2} \dot{q}(t)\cos(kz) \tag{2.2b}$$

where ω is the frequency, $k = \omega/c$ is the wave number, V is the effective volume of the cavity, and $q(t)$ will act as an canonical position.

2.2 Spatial Modes

The spatial distribution of the electromagnetic field in free space can be described as a superposition of plane waves. When boundary conditions are imposed, it becomes natural to describe the transverse spatial distribution of the field in terms of spatial modes commonly referred to as transverse electromagnetic modes (TEM modes). In a laser with cylindrical symmetry, combinations of Laguerre polynomials make up the spatial modes (called Laguerre-Gauss modes). If there is rectangular symmetry, Hermite polynomials determine the mode shape (called Hermite-Gauss modes),

$$
\begin{aligned}
E_{mn}(x,y,z) = E_0 \frac{w_0}{w(z)} H_m \left(\frac{\sqrt{2}x}{w(z)} \right) H_n \left(\frac{\sqrt{2}y}{w(z)} \right) \times \cdots \\
\exp \left[-(x^2+y^2) \left(\frac{1}{w(z)^2} + \frac{ik}{2R(z)} \right) - ikz - i(m+n+1)\psi(z) \right],
\end{aligned}
\tag{2.3}
$$

where E_0 is amplitude, ω_0 is the beam waist, ω is the spot size, H_m is the mth Hermite polynomial, R is the radius of curvature, and ψ is the Gouy phase. The waist is defined by distance away from the z axis where the field amplitude is $1/e$ the field amplitude on the axis. The Gouy phase is a phase the is acquired near the focus of the beam given by $\psi(z) = \arctan(z/z_R)$ where $z_R = \frac{\pi\omega_0^2 n}{\lambda}$ is the Rayleigh range, n is the index of refraction, and λ is the wavelength.

For the lowest order hermite polynomial, we recover the gaussian beam profile (H_{00}). We can write the cross-section of the electric field as, $E_{00}(x,y,z) = E_0 \exp(-\frac{x^2+y^2}{w(z)^2})$. The Gaussian beam (or TEM_{00}) is considered ideal to work with for many applications. Its single spatial mode allows for clean imaging (see Section 3.1) and a direct understanding of the local oscillator overlap with the squeezed field in homodyne detection (see Section 2.7).

2.3 Quantization of the Electric Field

The classical Hamiltonian of the field, for a particular polarization, is written as

$$
\mathcal{H} = \frac{1}{2} \int (\epsilon_0 E_x^2 + \frac{1}{\mu_0} B_y^2)\, dV, \tag{2.4}
$$

where we take the integral over the volume of the cavity (described in section 2.1). By substituting Eq. 2.2 into Eq. 2.4 and integrating over the volume of the cavity, we see

$$\mathcal{H} = \frac{1}{2}(p^2 + \omega^2 q^2), \tag{2.5}$$

where p is the canonical momentum and $p = \dot{q}$. Eq. 2.5 is exactly the same the simple harmonic oscillator (SHO), which has a well established commutation relationship, $[\hat{q}, \hat{p}] = i\hbar$. For convenience, we may rewrite the observables, $\hat{p}$ and $\hat{q}$, into "creation" and "annihilation" operators, $\hat{a}^\dagger$ and $\hat{a}$,

$$\hat{a}^\dagger = (2\hbar\omega)^{-1/2}(\omega\hat{q} - i\hat{p}) \tag{2.6a}$$

$$\hat{a} = (2\hbar\omega)^{-1/2}(\omega\hat{q} + i\hat{p}), \tag{2.6b}$$

with the following commutation relation: $[\hat{a}, \hat{a}^\dagger] = 1$. The electric field now becomes, $\hat{E}_x(z,t) = \mathcal{E}_0(\hat{a} + \hat{a}^\dagger)\text{sin}(kz)$, and we can write the Hamiltonian operator as

$$\hat{H} = \hbar\omega(\hat{a}^\dagger\hat{a} + \frac{1}{2}). \tag{2.7}$$

Defining $|n\rangle$ as an energy eigenstate of the single mode field given by Eq. 2.5,

$$\hat{H}|n\rangle = \hbar\omega(\hat{a}^\dagger\hat{a} + \frac{1}{2})|n\rangle = E_n|n\rangle, \tag{2.8}$$

where $E_n = \hbar\omega(n + \frac{1}{2}), n \in \mathbb{Z}^+$, we see this is analogous to the simple harmonic oscillator. The lowest possible energy (zero-point energy) is commonly referred to as the vacuum and has $E_0 = \hbar\omega\frac{1}{2}$.

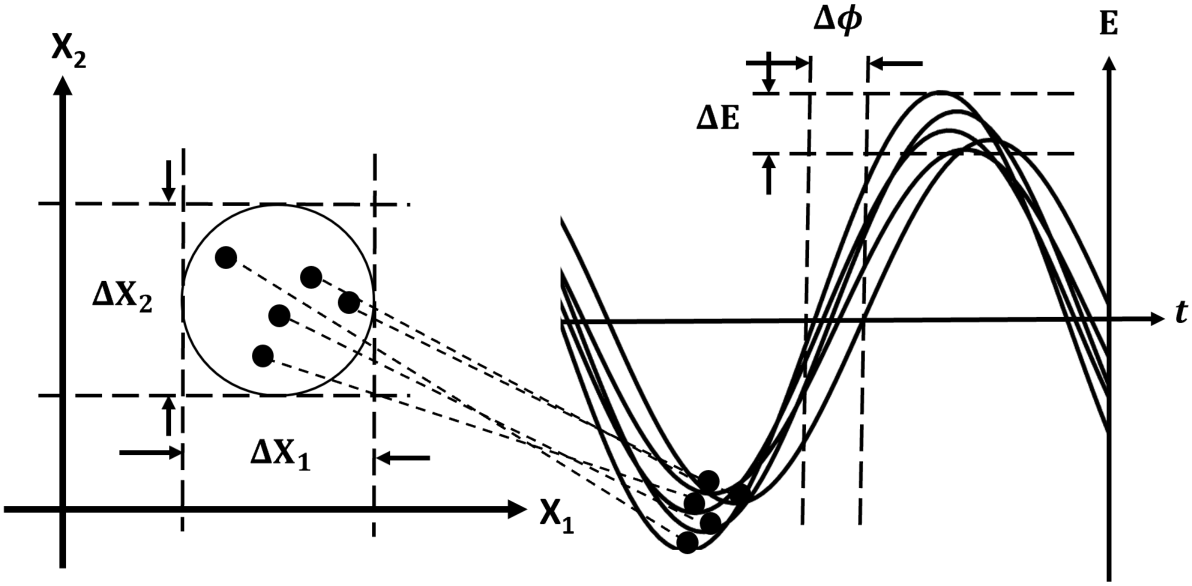

FIG. 2.2: A representation of the field fluctuations in quadrature (phase-space) representation.

2.4 Quadrature Operators

Analogous to position and momentum operators in the SHO, we define the quadratures,

$$\hat{X}_1 = \frac{1}{2}(\hat{a} + \hat{a}^\dagger), \tag{2.9a}$$

$$\hat{X}_2 = \frac{1}{2i}(\hat{a} - \hat{a}^\dagger). \tag{2.9b}$$

These quadratures satisfy the communtation relation $[\hat{X}_1, \hat{X}_2] = \frac{i}{2}$. The electric field can be rewritten in terms of the quadratures as: $2\mathcal{E}_0\sin(kz)[\hat{X}_1\cos(\omega t) + \hat{X}_2\sin(\omega t)]$. In this representation, $\hat{X}_1$ is the real part of the electric field and $\hat{X}_2$ is the imaginary part of the electric field. Again analogous to position and momentum, quadrature variance is given by [5],

$$\langle(\Delta\hat{X}_1)^2\rangle\langle(\Delta\hat{X}_2)^2\rangle \geq \frac{1}{16}. \tag{2.10}$$

This leads us to see that there is a minimum amount of noise that must always exist in our electric fields that is intrinsic to the quantum nature of the light. Equation 2.10 is called the standard quantum limit (SQL) when $\langle(\Delta\hat{X}_1)^2\rangle\langle(\Delta\hat{X}_2)^2\rangle = \frac{1}{16}$. Figure 2.2 illustrates how the quadratures are related to the field amplitude and phase. Variations in the are the electromagnetic field are denoted by ΔE and $\Delta\phi$. These variations are then mapped to the quadrature space and the spread of these points correspond to the noise in a give quadrature.

2.5 Classical Detection

There are many applications where the quantum noise in your probing field is irrelevant because the measurement is dominated by classical noise, so classical detection of the electric field will suffice. This classical noise can arise from many sources including: electronic, thermal and vibrational noise. The good news is many of these classical noises can be circumvented through thoughtful detection discussed below.

2.5.1 Classical Noise

Typical examples of classical noise include laser intensity fluctuations, temperature instability in the environment, current fluctuations from power supplies, vibrational noise (acoustic or otherwise), etc. A simple and common way to remove noise from your probing beam is to split it in two using a beam splitter, and then look at the differential signal. Now any common noise in the two beams will be removed. Other noise reduction techniques include laser frequency locks which reduce noise introduced by frequency drifts, laser amplitude stabilizers (noise eaters), and acoustic isolation. But as discussed in Section 2.4, no matter how well you control the classical noises in your system, you will always run up against the shot-noise limit.

2.5.2 Coherent States and the Shot-Noise Limit

We classically described light as a continuous wave propagating through a medium in Section 2.1. However, this is not entirely realistic. In reality, light sources emit radiation over a finite period of time causing the detected signal to be an average of all of these "bursts" with fluctuations around that average. These fluctuations manifest in both the amplitude and phase of the light and are intrinsic to the quantum nature of the light, giving rise to the SQL.

The coherent state is a minimum uncertainty state. It has the smallest amount of noise possible while the two quadratures are equal, $\langle(\Delta X_1)^2\rangle = \langle(\Delta X_2)^2\rangle = \frac{1}{4}$, and is known as the shot-noise limit. It is the smallest amount of noise attainable in a classical measurement before having to employ quantum mechanics. Figure 2.3 (a) shows the "ball on a stick" representation of the coherent state. The length of the stick represents the field amplitude, i.e. displacement, and the angle, θ away from the x-axis represents the phase. The fuzzy "noise ball" on the end of the stick represents the uncertainty associated with the amplitude and phase.

The coherent state, commonly written as $|\alpha\rangle$, can be generated by applying the displacement operator,

$$\mathbf{D}(\alpha) = \exp(\alpha\hat{a}^\dagger - \alpha^*\hat{a}) \tag{2.11}$$

to a vacuum state $|0\rangle$, $|\alpha\rangle = \mathbf{D}(\alpha)|0\rangle$. Here, α is the complex amplitude of the classical field. This is the most commonly used field and is what good lasers produce.

2.6 Squeezed Light

In Section 2.5 we discussed the coherent state, where the limits set by the quantum noise affect the phase and amplitude quadratures equally. However, it is possible to create

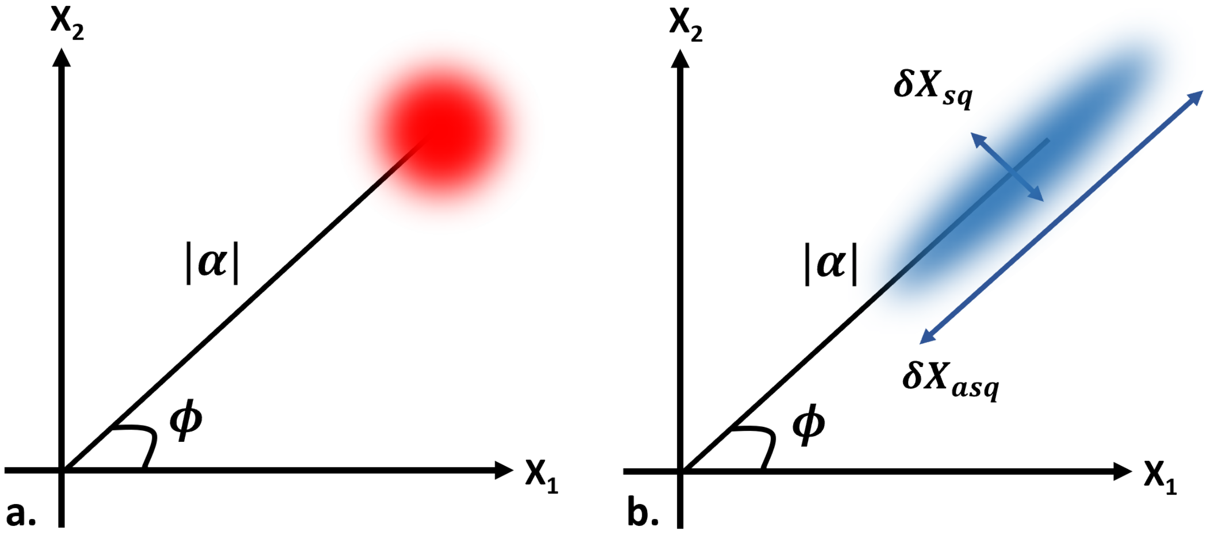

FIG. 2.3: a) noise ball depiction of a coherent state. b) noise ball depiction of a squeezed state.

a state where one of the quadratures has less noise than the shot noise limit. A squeezed state exists when, $\langle(\Delta X_1)^2\rangle \neq \langle(\Delta X_2)^2\rangle$, and

$$\langle(\Delta X_1)^2\rangle\langle(\Delta X_2)^2\rangle = \frac{1}{16}. \tag{2.12}$$

To generate these types of noise statics we need to invoke the squeezing operator, S,

$$S(\xi) = \exp(\frac{1}{2}\xi^*\hat{a}^2 - \frac{1}{2}\xi\hat{a}^{\dagger 2}), \tag{2.13}$$

where $\hat{a}$ and $\hat{a}^\dagger$ are the same creation and annihilation operators defined in eq. 2.6, ξ is defined as

$$\xi = re^{i\theta}, \tag{2.14}$$

where r is squeezing parameter which determines the degree of squeezing, and θ is the squeezing angle. To generate a squeezed coherent state, we act the squeezing operator on the displaced vacuum,

$$|\alpha,\xi\rangle = D(\alpha)S(\xi)|0\rangle. \tag{2.15}$$

Figure 2.3 (b) shows the "ball on a stick" representation of a phase-squeezed state. Here $|\alpha|$ is the amplitude (determined by the displacement operator) and the elliptical "fuzz" represents the noise in the amplitude and phase of the squeezed state. Setting $\theta = 0$ for simplicity, we can calculate the the average fluctuations of the squeezed and antisqueezed quadratures,

$$\langle\alpha,\xi|(\Delta X_1)^2|\alpha,\xi\rangle = \frac{1}{4}\exp(-2r) \tag{2.16a}$$

$$\langle\alpha,\xi|(\Delta X_2)^2|\alpha,\xi\rangle = \frac{1}{4}\exp(2r), \tag{2.16b}$$

with the average photon number of the squeezed state being

$$\langle\alpha,\xi|\hat{n}|\alpha,\xi\rangle = |\alpha|^2 + \sinh^2(r). \tag{2.17}$$

For the vacuum state $|\alpha|^2 = \xi = 0 \rightarrow \langle\alpha,\xi|\hat{n}|\alpha,\xi\rangle = 0$. If the vacuum is squeezed $|\alpha|^2 = 0$ still, but now the squeezing parameter is nonzero. Figure 2.4 shows an example of how the quadrature changes with phase of the electric field.

2.6.1 Generating Squeezed Light

Generating the squeezed field comes through nonlinear light-atom interactions in a medium. We can describe the polarization response to the field in the medium as,

$$P(t) = \epsilon[\chi^{(1)}E(t) + \chi^{(2)}E^2(t) + \chi^{(3)}E^3(t) + \cdots], \tag{2.18}$$

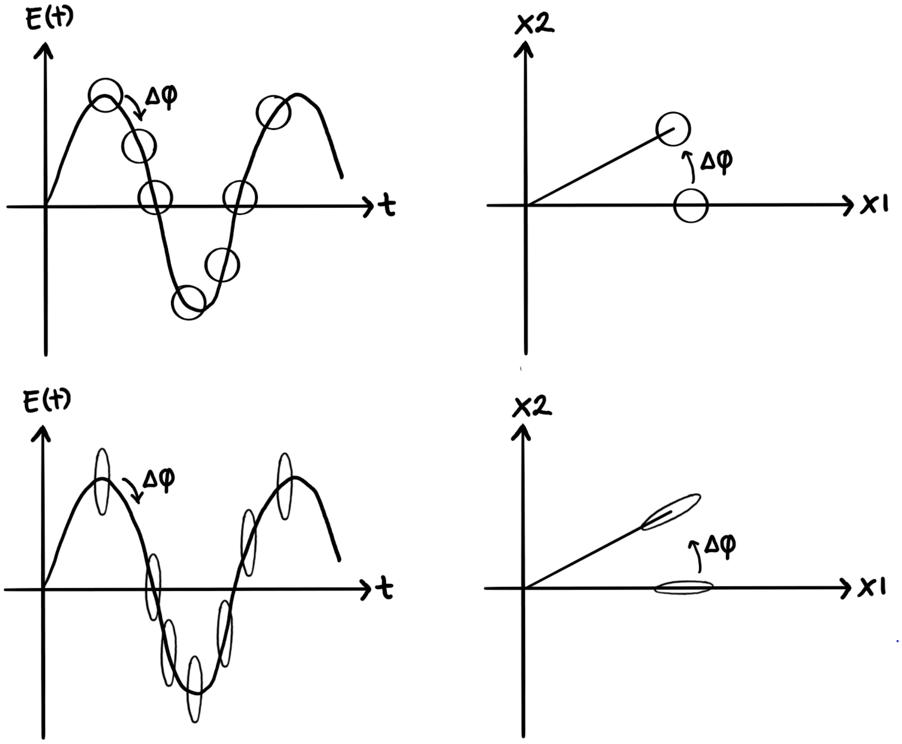

FIG. 2.4: Comparison of the coherent state noise distribution with the squeezed state as the electric field propagates in time. On the left, an electric field, $E(t)$ is shown as it propagates in time (or its phase changes). The solid black line shows the mean field value while the superimposed circle or ellipse represents the noise at that particular time. The top electric field illustrates the coherent state where there is equal noise in the amplitude and phase, while the bottom electric field illustrates a phase squeezed state (there is less noise in the phase than the amplitude). On the right we have the quadrature space depiction of the field (i.e. ball-on-a-stick description). The stick represents the amplitude of the electric field and the ball (ellipse) represents the noise associated with each quadrature. Changes in the phase of the field ($\Delta\phi$) is represented by rotation about the origin.

where $\chi^{(i)}$ is the ith order electric susceptibility. When $E(t)$ is small the polarization response linear with intensity. As $E(t)$ grows, the higher order polarization effects start to create non-negligible effects in the atomic properties. While many applications exploit the $\chi^{(2)}$ nonlinear interaction using second harmonic generation in crystals, it is possible to access the $\chi^{(3)}$ interaction using an atomic vapor. While both $\chi^{(2)}$ and $\chi^{(3)}$ processes may give rise to squeezing via photon pair generation, we will focus on $\chi^{(3)}$ interactions which arise in atomic ensembles. A generic way of writing the Hamiltonian in these systems is [4],

$$H = i\hbar[|E|^2\chi^{(3)}\hat{a}^2 - |E|^2\chi^{(3)}\hat{a}^{\dagger 2}], \tag{2.19}$$

where $|E|^2$ is the strength of the pump, $\hat{a}^\dagger$ is the creation operator and $\hat{a}$ is the annihilation operator. We will explore one of the ways to produce squeezing using a $\chi^{(3)}$ light-atom interaction in Rubidium vapor: *polarization self-rotation.*

Polarization Self-Rotation

Polarization self-rotation (PSR) occurs when elliptically polarized light travels through a nonlinear medium. Since the medium is birefringent the right-handed ($\sigma_+^{(0)}$) and left-handed ($\sigma_-^{(0)}$) polarization components of the light see a different index of refraction. This causes the one polarization to acquire a phase relative to the other, $\sigma_\pm = \sigma_\pm^{(0)} e^{\mp i\phi}$. If you write the electric field in terms of its linear components ($E_x^{(0)}, E_y^{(0)}$), you will see that the acquired phase results in a rotation of the major axis of polarization by ϕ

$$E_x = E_x^{(0)}\cos(\phi) + E_y^{(0)}\sin(\phi) \tag{2.20a}$$

$$E_y = E_y^{(0)}\cos(\phi) - E_x^{(0)}\sin(\phi). \tag{2.20b}$$

For a small initial ellipticity, the maximum rotation, ϕ, expected from this effect can be written as

$$\phi = \epsilon(0)gL, \tag{2.21}$$

where $\epsilon(0)$ is the original elipticity, g is determined by the light intensity and features of the atomic system (discussed further in the next section), and L is the optical path length [43, 3].

Squeezing from PSR

Polarization self-rotation can also produce squeezing. When a strong linearly polarized pump field passes through a $\chi^{(3)}$ medium, the major polarization axis is rotated slightly because there are still vacuum fluctuations (i.e. a very small number of photons) in the orthogonal polarization. More specifically, two photons are absorbed from the pump polarization and then simultaneously emitted into the orthogonal polarization with correlated phase. This is due to the type of Hamiltonian governing these systems as described in Eq. 2.19. The correlations produced result in the quadrature noise distribution changing, i.e. the quadrature is squeezed like discussed in Section 2.6.1. Predicting the level of squeezing was studied thoroughly in [44] where they found the variance of the field to be,

$$\langle \hat{\mathbf{E}}_x(\phi, L)^2 \rangle = \frac{E_0^2}{4}\left(1 - 2gL\sin\phi\cos\phi + g^2L^2\cos^2\phi\right), \tag{2.22}$$

where ϕ is the phase, g is determined by the light intensity and features of the atomic system (discussed further is Section 2.6.2), and L is the optical path length [43, 3]. Figure 2.6.1 shows the normalized variance $(4\langle \hat{\mathbf{E}}_x(\phi, L)^2 \rangle / E_0)$ as a function of phase, ϕ.

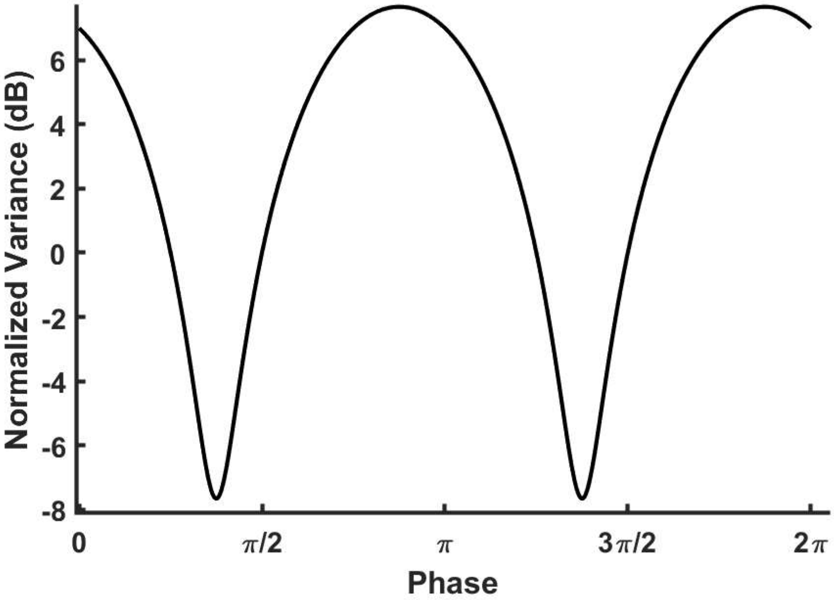

FIG. 2.5: Normalized variance of the squeezed field, with gL=2. Here, shot noise is zero and we can achieve equal amounts of squeezing and antisqueezing.

Estimating g in Rb vapor

We can get a qualitative understanding of where the g parameter arises in our atomic system, by using the model outlined in [45]. Assume a linearly polarized field passes through an optically thick medium. We can think of our linearly polarized field as two circularly polarized fields, σ_+, and σ_- that couple to resonance structure of our medium according to Fig. 2.6. The field is not perfectly linear causing one of the circular components to be slightly stronger. The fields are nearly resonant with $|3\rangle$ and detuned from $|e\rangle$ by Δ. Even though there is no magnetic field, the ground states will experience different ac-stark shifts due to the uneven coupling of the circular field components.

According to [45], we can write the polarization rotation of this system as,

$$\phi = \frac{\gamma\kappa}{2\Delta}\frac{|\Omega_1|^2 - |\Omega_2|^2}{|\Omega(0)|^2}L, \tag{2.23}$$

where γ is the radiative linewidth of the transitions, $\kappa = (3\pi/4)N\lambda^2$, where N is the atomic

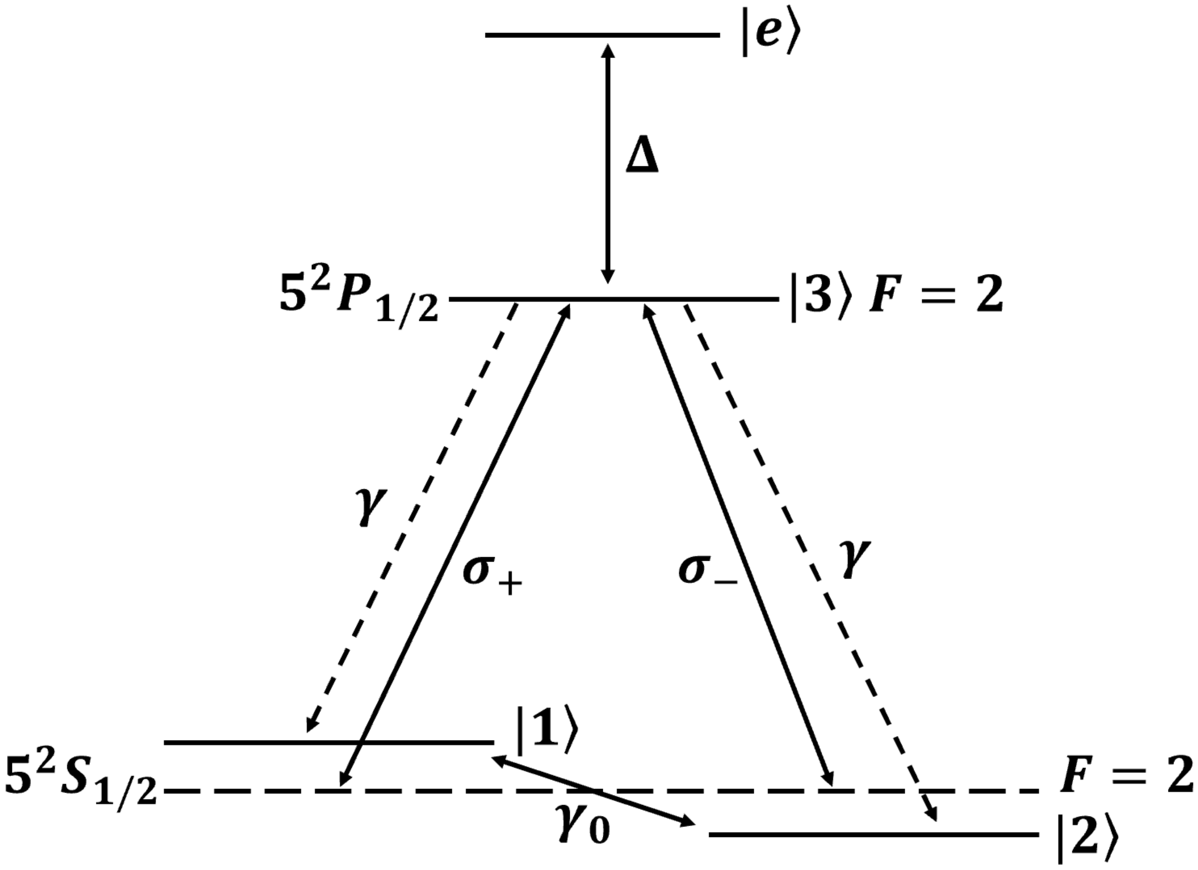

FIG. 2.6: Depiction of energy levels.

density and λ is the wavelength of the field, Ω is the rabi frequency, and L is the path length. Finally, by taking the results found in [46], we see we can write elipticity, ϵ, as,

$$\epsilon \approx \frac{|\Omega_1|^2 - |\Omega_2|^2}{|\Omega(0)|^2}. \tag{2.24}$$

Putting it all together, we can write,

$$\phi = \epsilon g L \tag{2.25}$$

where $g = \frac{\gamma\kappa}{2\Delta}$ just like in Eq. 2.21. While this description of polarization self-rotation doesn't quantitatively reproduce the squeezing levels we see in the experiment, it does give us insight into the atomic processes and allows us to gain intuition around the experimental parameters we can control (power, atomic density, etc.).

2.6.2 Why ^{87}Rb?

^{87}Rb is chosen as the nonlinear medium in this work because it is a well studied, alkali element. This means it only has one valence electron making it hydrogen-like, ideal for atomic experiments since the atomic energy structure is relatively simple. There are two optical transitions connecting the ground states that are commonly called the D1 line (λ = 795 nm) and the D2 line (λ = 780 nm). For the experiments described in the rest of this work, we will use the D1 line which connects the $5^2S_{1/2}$ ground state to the $5^2P_{1/2}$ excited state. Figure 2.7 shows the ground state and excited state of the D1 line and the hyperfine levels and the absorption spectrum of the D1 line. We work at this resonance, particularly the $F_g = 2 \rightarrow F_e = 2$ transition, because relatively strong vacuum squeezing is experimentally produced ($\sim$2.5 dBs).

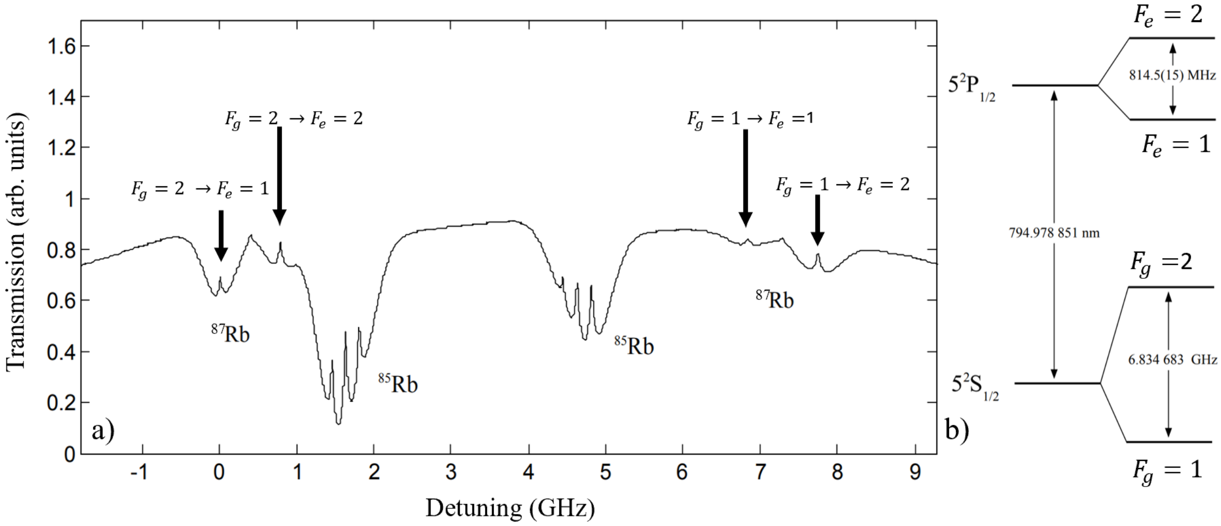

FIG. 2.7: D1 atomic energy levels adapted from [3]. a) shows the saturated spectroscopy transmission through Rubidium, with the ^{87}Rb transitions labeled (ground state→ excited state). b) is a level diagram of the D1 transition in Rb.

2.7 Quantum Detection

Once a squeezed state has been constructed, we will need a phase-sensitive measurement scheme so we can detect both squeezed and anti-squeezed quadratures. To meet this requirement we will use a *homodyne detection* scheme. To create this we need another beam as a phase reference, traditionally called the local oscillator. The local oscillator must be phase-locked to squeezed beam, so we will assume that they both come from the same lasing source.

To understand the system (see Fig 2.8), we will represent the local oscillator as $\alpha_{LO}(t)$, and the squeezed state as $\alpha_{in}(t)$, where

$$\alpha_{in}(t) = \alpha_{in} + \Delta X1_{in} + i\Delta X2_{in} \tag{2.26a}$$

$$\alpha_{LO}(t) = [\alpha_{LO} + \Delta X1_{LO} + i\Delta X2_{LO}]e^{i\phi_{LO}}. \tag{2.26b}$$

We define $e^{i\phi_{LO}}$ as the phase difference between the local oscillator and the squeezed

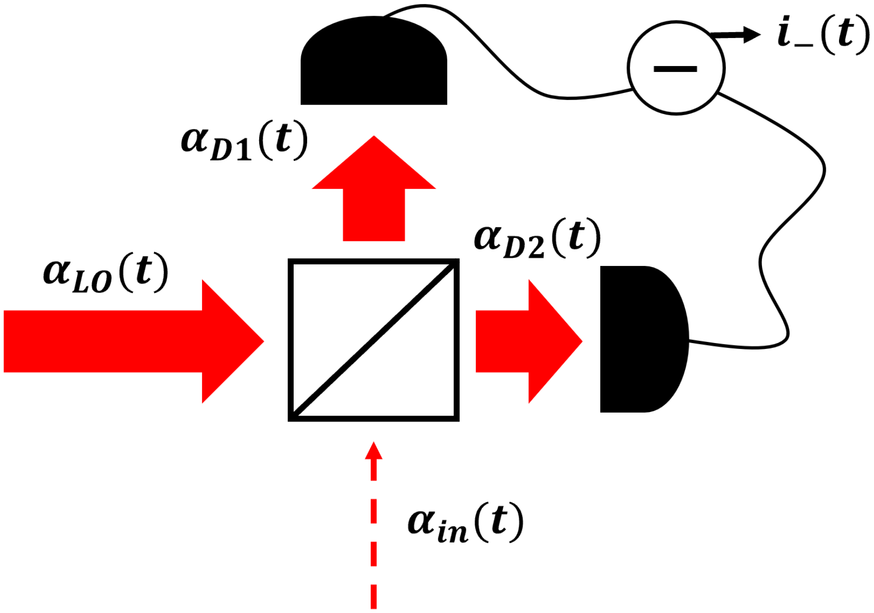

FIG. 2.8: Homodyne detection scheme

vacuum fields and $\Delta X1/X2$ as the noise in each quadrature respectively.

We consider the case when $\alpha_{LO}^2 >> \alpha_{in}^2$. So, when we mix the squeezed field and local oscillator, the local oscillator will dominate the signal. The input on each of the detectors will be $|\overline{\alpha_{D1}}|^2 = |\overline{\alpha_{D2}}|^2 \approx \frac{1}{2}|\overline{\alpha_{LO}}|^2$. We can write

$$\alpha_{D1} = \sqrt{1/2}\alpha_{LO}(t) + \sqrt{1/2}\alpha_{in}(t) \tag{2.27a}$$

$$\alpha_{D2} = \sqrt{1/2}\alpha_{LO}(t) - \sqrt{1/2}\alpha_{in}(t). \tag{2.27b}$$

However, intensities (and photocurrents) are proportional to $|\alpha_{D1/2}|^2$, so the meaningful quantities are

$$|\alpha_{D1}|^2 = \frac{1}{2}[|\alpha_{LO}(t)|^2 + \alpha_{LO}(t)\alpha_{in}(t)^* + \alpha_{in}(t)\alpha_{LO}(t)^* + |\alpha_{in}(t)|^2], \tag{2.28}$$

with a similar expression for $|\alpha_{D2}|^2$. Any α_{in} terms can be disregarded based on our previous assumption leading us to

$$|\alpha_{D1}|^2 = \frac{1}{2}[|\alpha_{LO}|^2 + 2\alpha_{LO}\Delta X1_{LO}(t) + 2\alpha_{LO}(\Delta X1_{in}(t)\cos(\phi_{LO}) + i\Delta X2_{in}(t)\sin(\phi_{LO}))]. \tag{2.29}$$

Similar results can be found for the second detector, leaving the differential current as

$$i_-(t) = |\alpha_{D1}|^2 - |\alpha_{D2}|^2 \approx 2\alpha_{LO}(\Delta X1_{in}(t)\cos(\phi_{LO}) + i\Delta X2_{in}\sin(\phi_{LO})). \tag{2.30}$$

So, in the homodyne detection scheme, only the quadrature terms from the input field (squeezed field) are amplified by the local oscillator contributing to the final signal, and any small noise from the local oscillator is canceled out since it is common to both detectors. We also have control over which noise quadrature we analyze by tuning ϕ_{LO} as needed; $\phi_{LO} = 0 \longrightarrow \Delta X1_{in}$ and $\phi_{LO} = \pi/2 \longrightarrow \Delta X2_{in}$.

Lastly, we can calculate the variance of $i_-(t)$,

$$\Delta i_-^2 = \langle i_-(t)^2\rangle - \langle i_-(t)\rangle^2 \approx 4\alpha_{LO}^2\left((\Delta X1_{in}^2(t)\cos^2(\phi_{LO}) + \Delta X2_{in}^2\sin^2(\phi_{LO})\right) \tag{2.31}$$

Note, cross terms of the form $\Delta X1\Delta X2$ average to zero.

Figure 2.9 shows experimental homodyne results from a squeezed vacuum. Instead of sweeping through all the phases, like in Fig. 2.6.1, we tune our phase between the local oscillator and squeezed vacuum to be either at the minimum noise to measure the squeezed quadrature, or the maximum noise to measure the antisqueezed quadrature.

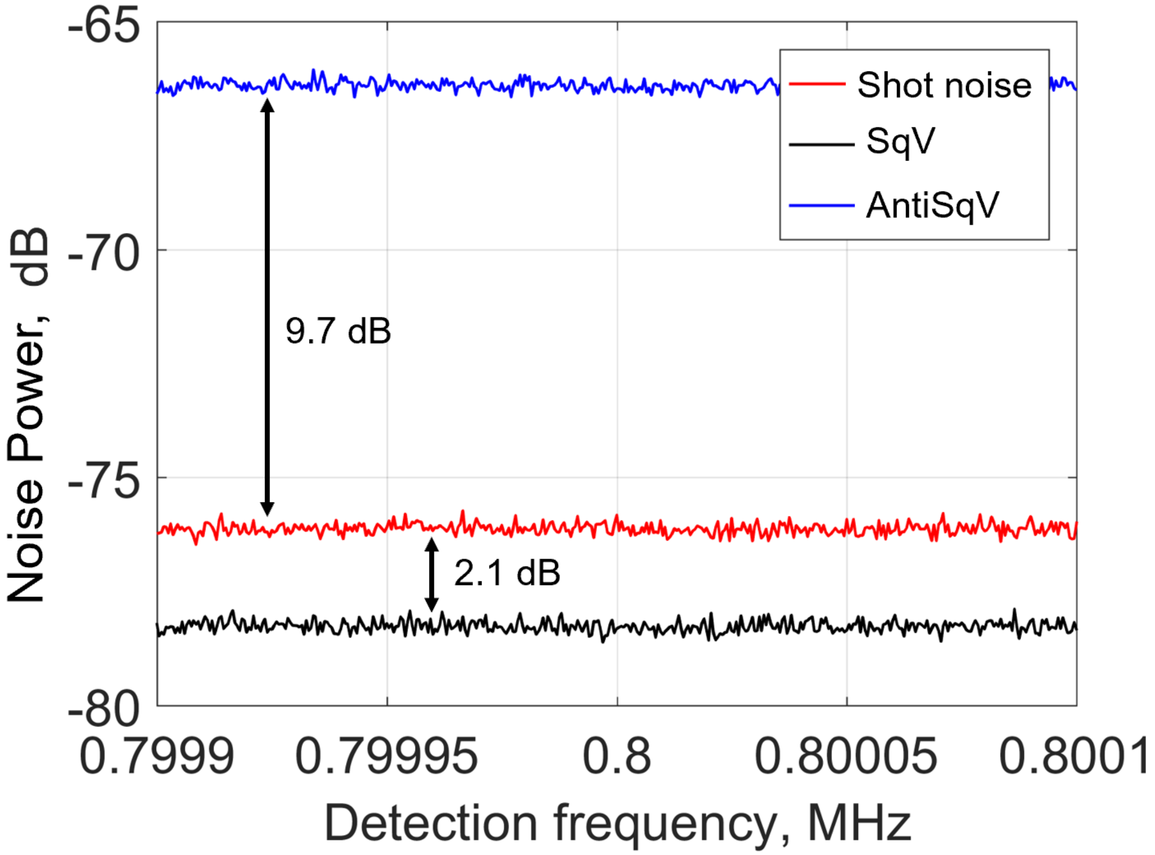

FIG. 2.9: Noise power traces of maximum (antisqueezed) and minimum (squeezed) noise compared to shot noise. We measure -2.1 dB of squeezing and 9.7 dB of antisqueezing.

CHAPTER 3

Theory of Spatial Noise Detection

3.1 Spatial Overlap with the Local Oscillator

In section 2.7, we showed how homodyne detection works. However, there was an underlying assumption that the local oscillator is in the same spatial mode as the input field we are trying to detect. As section 2.2 has shown us though, the spatial distribution of the field can take on many different spatial modes. Recent theoretical work [47] and experimental work [48] shows the possibility of the squeezed stated existing in many spatial modes , i.e. the local oscillator and the input fields do not necessarily have the *same* spatial mode. To take the spatial mode mismatch into account, we define the local and input fields as

$$\alpha_{\mathrm{in,n}}(t) = [\alpha_{in} + \Delta X1_{\mathrm{in,n}} + i\Delta X2_{\mathrm{in,n}}]u_{\mathrm{in,n}}(x,y) \tag{3.1a}$$

$$\alpha_{LO}(t) = [\alpha_{LO} + \Delta X1_{LO} + i\Delta X2_{LO}]u_{\mathrm{LO}}(x,y)e^{i\phi_{LO}}, \tag{3.1b}$$

where u_{LO} and $u_{\mathrm{in,n}}$ are the spatial distributions of the local oscillator and "nth" mode of the input field (which could be the squeezed field), and $\alpha_{\mathrm{in}}(t) = \sum_n \alpha_{\mathrm{in,n}}(t)$.

Similar to before, we assume $\alpha_{\mathrm{LO}}^2 >> \alpha_{\mathrm{in}}^2$ and that each detector ($D1/D2$) can be written as Eq. 2.27. So we can write the intensity at the detectors as,

$$\begin{aligned}|\alpha_{\mathrm{D1}}|^2 = \frac{1}{2}[|\alpha_{\mathrm{LO}}|^2 + 2\alpha_{\mathrm{LO}}\Delta X1_{\mathrm{LO}} + 2\alpha_{\mathrm{LO}}\Delta X2_{\mathrm{LO}}]|u_{\mathrm{LO}}(x,y)|^2 + \cdots \\ + \frac{1}{2}\sum_n [\alpha_{\mathrm{LO}}\Delta X1_{\mathrm{in,n}} - i\alpha_{\mathrm{LO}}\Delta X2_{\mathrm{in,n}}]u_{\mathrm{LO}}(x,y)u_{\mathrm{in,n}}(x,y)e^{i\phi} + c.c.,\end{aligned} \tag{3.2}$$

with a similar expression for $D2$. We can write the differential intensity as,

$$\begin{aligned}i_-(t) &= \int_{\mathrm{A}} \left(|\alpha_{\mathrm{D1}}|^2 - |\alpha_{\mathrm{D2}}|^2\right) ds \\ &= \alpha_{\mathrm{LO}} \int_{\mathrm{A}} \sum_n [\Delta X1_{\mathrm{in,n}} u_{\mathrm{LO}}(x,y)u_{\mathrm{in,n}}(x,y)e^{i\phi} \\ &- i\Delta X2_{\mathrm{in,n}} u_{\mathrm{LO}}(x,y)u_{\mathrm{in,n}}(x,y)e^{i\phi} \ + c.c \ ] \ ds,\end{aligned} \tag{3.3}$$

where we integrate the differential intensity over the detector area, A. We should note that our detectors, $D1$ and $D2$, do not necessarily have to have the same detection area, A. However, we make this assumption since it is standard to use nearly identical detectors in homodyning systems. Collecting like terms together we can write

$$\begin{aligned}i_-(t) = \alpha_{\mathrm{LO}} \int_{\mathrm{A}} \sum_n [\Delta X1_{\mathrm{in,n}} u_{\mathrm{LO}}(x,y)u_{\mathrm{in,n}}(x,y)\cos(\phi) \\ + \Delta X2_{\mathrm{in,n}} u_{\mathrm{LO}}(x,y)u_{\mathrm{in,n}}(x,y)\sin(\phi) \ ] \ ds.\end{aligned} \tag{3.4}$$

3.2 Calculating the Variance

We want to calculate the variance of the current in Eq. 3.4, $V = \langle i_-(t)^2\rangle - \langle i_-(t)\rangle^2$. Similar to the traditional homodyne detector,

$$\langle i_-(t)\rangle^2 = 0 \tag{3.5}$$

$$\langle i_-(t)^2\rangle = \alpha_{\mathrm{LO}}^2 \sum_n [\Delta X1_{\mathrm{in,n}}^2 \cos^2(\phi) + \Delta X2_{\mathrm{in,n}}^2 \sin^2(\phi)] \left| \int_{\mathrm{A}} (u_{\mathrm{LO}}^*(x,y) u_{\mathrm{in,n}}(x,y)\ )\, ds \right|^2, \tag{3.6}$$

with all cross terms averaging to zero since $\Delta X1/\Delta X2$ are not correlated. Calculating the variance of the differential current we see,

$$\begin{aligned} V &= \langle i_-(t)^2\rangle - \langle i_-(t)\rangle^2 \\ &= \alpha_{\mathrm{LO}}^2 \sum_{\mathrm{n}} V_{\mathrm{n}}(\phi) \left| \int_{\mathrm{A}} (u_{\mathrm{LO}}^* u_{\mathrm{in,n}})\, ds \right|^2 \\ &= \alpha_{\mathrm{LO}}^2 \sum_n V_{\mathrm{n}}(\phi) |\mathcal{O}_{\mathrm{n}}|^2. \end{aligned} \tag{3.7}$$

We define

$$\mathcal{O}_{\mathrm{n}} = \int_{\mathrm{A}} (u_{\mathrm{LO}}^* u_{\mathrm{in,n}})\, ds \tag{3.8}$$

as the *overlap* between the local oscillator and the n^{th} mode of the input field over a detector area (A), and $V_n(\phi)$ is the noise $(\Delta X1_n^2 \cos^2(\phi) + \Delta X2_n^2 \sin^2(\phi))$ we are measuring. Note, u_i are part of an orthonormal basis where $\int_{-\infty}^{\infty} u_{\mathrm{n}}^* u_{\mathrm{m}} ds = \delta_{nm}$. We can write the variance normalized as shotnoise, $\tilde{V} = \frac{V_{\mathrm{Exp}}}{V_{\mathrm{SN}}}$, as

$$\tilde{V} = \frac{\alpha_{\mathrm{LO}}^2 \sum_n V_{\mathrm{n}}(\phi) |\mathcal{O}_{\mathrm{n}}|^2}{\alpha_{\mathrm{LO}}^2 \sum_m V_m^{(0)} |\mathcal{O}_{\mathrm{m}}|^2}, \tag{3.9}$$

where $V_m^{(0)}$ is the m^{th} spatial mode of shotnoise. Separating the squeezed and unsqueezed contributions we write,

$$\tilde{V} = \frac{\alpha_{\mathrm{LO}}^2 \sum_s V_{\mathrm{s}}(\phi)|\mathcal{O}_{\mathrm{s}}|^2}{\alpha_{\mathrm{LO}}^2 \sum_m V_m^{(0)}|\mathcal{O}_{\mathrm{m}}|^2} + \frac{\alpha_{\mathrm{LO}}^2 \sum_{n\neq s} V_{\mathrm{n}}^{(0)}(\phi)|\mathcal{O}_{\mathrm{n}}|^2}{\alpha_{\mathrm{LO}}^2 \sum_m V_m^{(0)}|\mathcal{O}_{\mathrm{m}}|^2} \tag{3.10a}$$

$$\tilde{V} = \frac{\alpha_{\mathrm{LO}}^2 \sum_s (V_{\mathrm{s}}(\phi) - V_s^{(0)})|\mathcal{O}_{\mathrm{s}}|^2}{\alpha_{\mathrm{LO}}^2 \sum_m V_m^{(0)}|\mathcal{O}_{\mathrm{m}}|^2} + \frac{\alpha_{\mathrm{LO}}^2 \sum_n V_{\mathrm{n}}^{(0)}(\phi)|\mathcal{O}_{\mathrm{n}}|^2}{\alpha_{\mathrm{LO}}^2 \sum_m V_m^{(0)}|\mathcal{O}_{\mathrm{m}}|^2} \tag{3.10b}$$

$$\tilde{V} = 1 + \sum_s (V_{\mathrm{s}}(\phi) - 1)\frac{|\mathcal{O}_{\mathrm{s}}|^2}{\sum_m |\mathcal{O}_{\mathrm{m}}|^2}, \tag{3.10c}$$

where $V_m^{(0)} = 1$ (normalized shot noise) and V_s is the noise of the squeezed component of the input field. The sum of all the overlaps approaches unity ($\sum_{\mathrm{m}} |\mathcal{O}_{\mathrm{m}}|^2 \to 1$) as $A \to \infty$. When the local oscillator and the squeezed input field are in the same mode and you are looking at the overlap over a small area, A, it can be written as

$$|\mathcal{O}_{\mathrm{s}}|^2 = \left| \int_A u_{\mathrm{LO}} u_{\mathrm{s}} \mathrm{dA} \right|^2 = \frac{\alpha_{\mathrm{LO}}^2 \left| \int_A u_{\mathrm{LO}} u_{\mathrm{LO}} \mathrm{ds} \right|^2}{\alpha_{\mathrm{LO}}^2 | \int_{-\infty}^{\infty} u_{\mathrm{LO}} u_{\mathrm{LO}} \mathrm{ds}|^2} = \frac{I_{\mathrm{A}}}{I_{\mathrm{tot}}}, \tag{3.11}$$

where I_{A} is the intensity in the detection area, A, and I_{tot} is the total intensity since the integral of the oscillator over the detector area effectively calculates the percentage of local oscillator that falls on the detection area. This ratio of intensities can be viewed as a loss.

3.3 The Effects of Loss on the Variance

Up to this point, we have assumed that the squeezed vacuum propagates and mixes with the local oscillator undisturbed. However, if we place an absorbing object into the path of the squeezed vacuum, its transmission, T, will affect the noise we measure. When a squeezed field experiences loss it can be thought of like passing though a beam splitter where a portion of the squeezed field is stripped off and replaced with a coherent vacuum.

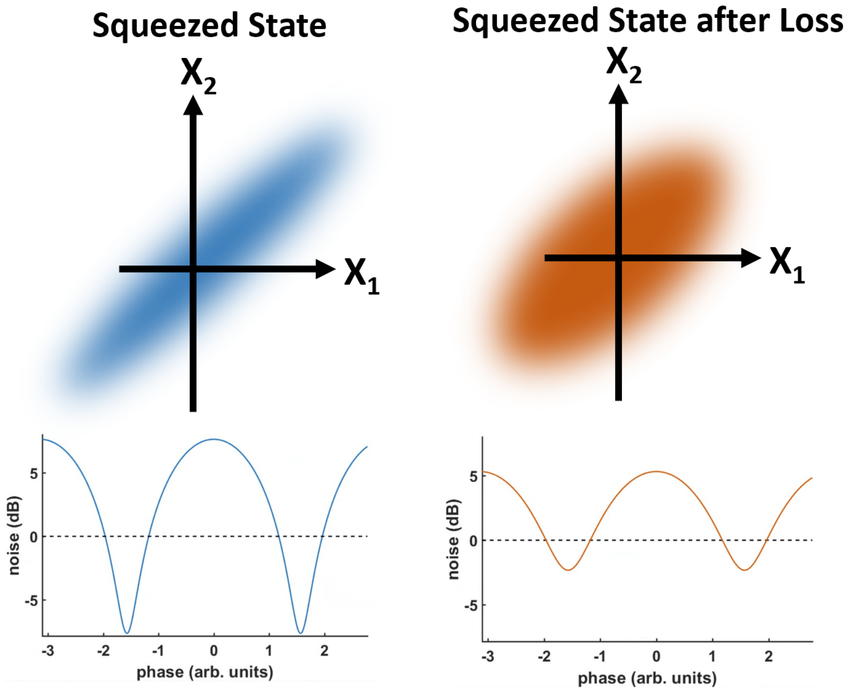

FIG. 3.1: Illustration of how a loss will degrade the squeezing to shot noise. Here, the squeezed state starts with equal amounts of squeezing and antisqueezing (the black dashed line marks the shot noise level). However, after experiencing loss, the squeezing and antisqueezing both degrade towards shot noise.

This causes a reduction in the amount of squeezing and antisqueezing present in the field, bringing the noise distribution close and closer to the shot noise distribution. We can include this loss into our expression for the normalized variance as

$$V = 1 + \sum_s (V_\mathrm{s} - 1) \frac{|\mathcal{O}_\mathrm{s} \otimes T(x,y)|^2}{\sum_m |\mathcal{O}_\mathrm{m}|^2}, \tag{3.12}$$

where $T \in [0,1]$ is the field transmission, $\mathcal{O}$ is the overlap, $\mathcal{O} \otimes T(x,y) = \int_A \left(u^*_\mathrm{LO} u_\mathrm{s} T(x,y)\right) ds$, and V_s is the noise defined in Section 3.2. In other words, $1 - |T|^2$ is the intensity *loss* through the object in the vacuum port.

The squeezed state is extremely sensitive to loss and will quickly degrade to shot noise as shown in Figure 3.1. By understanding how the loss affects the spatial distribution of the quantum noise statistics in our probe, we can use the change in noise statistics as a way to image objects probed with the squeezed vacuum. To extract the transmission map, $|T(x, y)|^2$, and image the object placed in the squeezed vacuum, we can compare the probing field's variance map (V_{Ob}) to the unobscured, empty squeezed vacuum variance map (i.e. $T(x, y) = 1$),

$$V_{\mathrm{empty}}(x, y) = 1 + \sum_s (V_{\mathrm{s}} - 1) \frac{|\mathcal{O}_{\mathrm{s}}|^2}{\sum_m |\mathcal{O}_{\mathrm{m}}|^2} \tag{3.13a}$$

$$V_{\mathrm{Ob}}(x, y) = 1 + \sum_s (V_{\mathrm{s}} - 1) \frac{|\mathcal{O}_{\mathrm{s}} \otimes T(x, y)|^2}{\sum_m |\mathcal{O}_{\mathrm{m}}|^2}. \tag{3.13b}$$

$$\tag{3.13c}$$

Assuming a single squeezed mode and that the transmission does not change over the detection area, A, we can write,

$$V_{\mathrm{Ob}}(x, y) = 1 + (V_{\mathrm{s}} - 1) \frac{|\mathcal{O}_{\mathrm{s}}|^2}{\sum_m |\mathcal{O}_{\mathrm{m}}|^2} T(x, y)^2. \tag{3.14}$$

Now, by subtracting one from Eq. 3.14 and Eq. 3.10, and taking the ratio we find,

$$T(x, y)^2 = \frac{V_{\mathrm{Ob}}(x, y) - 1}{V_{\mathrm{empty}}(x, y) - 1}. \tag{3.15}$$

This method of retrieving the object's transmission map based on noise measurements is the foundation of imaging with quantum noise.

3.4 Effects of Noise Contamination

True degradation of the squeezed field due to losses in the vacuum's path would result in the squeezed and antisqueezed quadratures both approaching shot noise as seen in Section 3.3. However, when parasitic noise contaminates the probing field, several effects

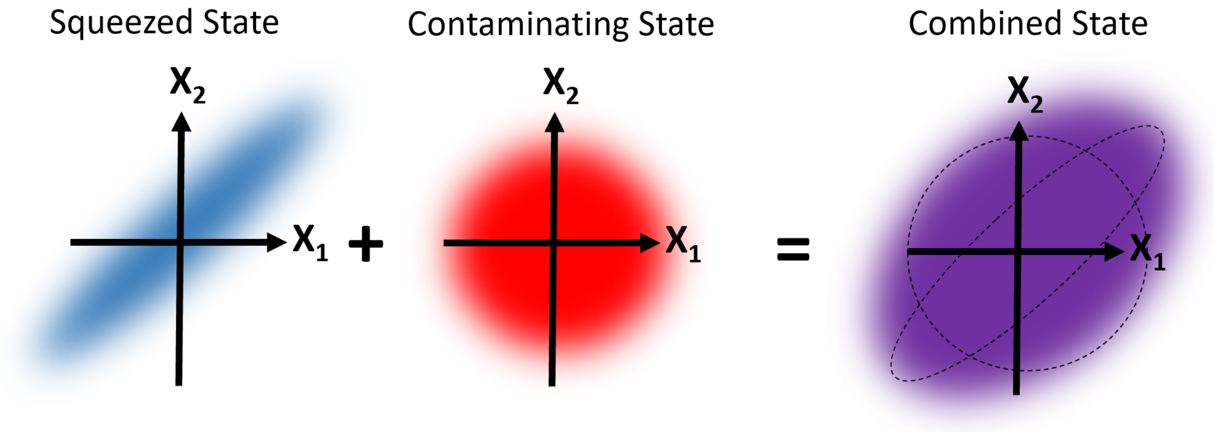

FIG. 3.2: Illustration of how a contaminating field alters the noise distribution of a squeezed state.

may occur that distort the variance. Assuming perfect overlap between the local oscillator and squeezed state, as well as a detector area much larger than the spatial mode of the beam, we can model the squeezed vacuum noise response to change in phase as,

$$V_1(\phi) = V_0 \cos^2(\phi) + \frac{1}{V_0} \sin^2(\phi), \tag{3.16}$$

where $V_0 = e^{2r}$ as defined in Eq. 2.16.

If there is a parasitic noise mode, V_p, contaminating our original squeezed state and overlapping with the local oscillator, the sum of $V_1 + V_p$ results in a new state that has left the antisqueezed quadrature largely unchanged while degrading our squeezed quadrature closer to (or even beyond) shot noise. Figure 3.2 shows the noise ball depiction of a squeezed state and a contaminating state. Figure 3.3 illustrates how the noise of a squeezed state would change under obscured detection, loss in the squeezed field, and the addition of a contaminating noise mode. Understanding how the noise distribution changes with loss or contamination are imperative to exploit the spatial noise properties for imaging since we don't want to confuse loss from an object we want to image with amplified noise contamination. This problem becomes very difficult once you move from a single spatial

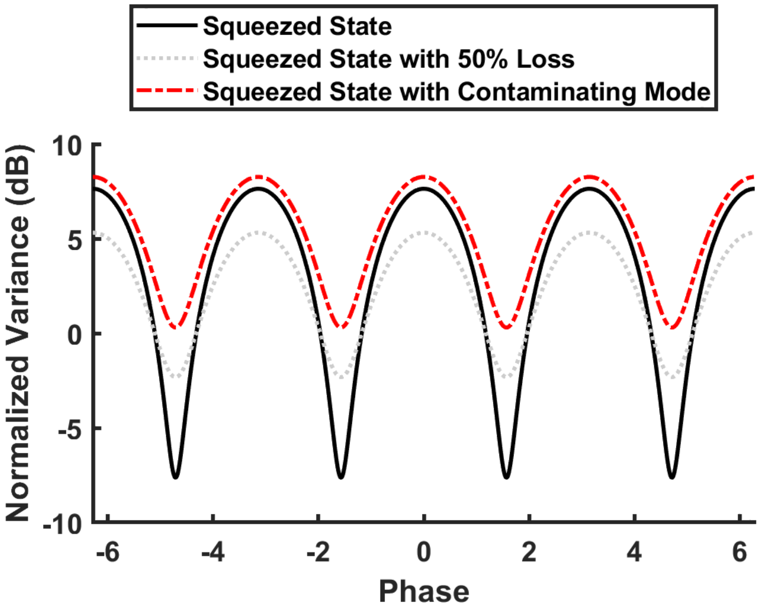

FIG. 3.3: Illustration of noise under different conditions. The solid black curve shows an unobscured squeezed state noise trace (V_1), the light grey dashed line shows the pure squeezed state after experiencing a loss, and the red dotted line shows the squeezed state when a parasite mode ($V_1 + V_p$) is present. The shot noise level is at the zero mark.

mode to multiple spatial modes since each spatial mode may have its own squeezing angle.

CHAPTER 4

Direct Quantum Imaging with a CCD Camera

4.1 Introduction

While traditionally squeezing is used to suppress noise in interferometric measurements, during the past few decades people have also explored using squeezing for imaging. There are several limitations that come into play when imaging: 1) the dark noise level of your camera, 2) the resolution of your imaging system (set by your physical optics or the diffraction limit), 3) the shot noise of your light. Many quantum-based imaging schemes [12, 13, 49, 50, 35] focus on reducing the noise in your image beyond the SNL by suppressing the uncertainty in the photon number using two-mode optical fields which have correlated intensity fluctuations — outperforming its classical counterpart. These are generated through parametric down conversion [51, 52, 53, 54] or four-wave mixing in an atomic vapor [38, 55, 56, 57, 58]. If an object is placed in one of the optical beams, its shape can be recreated with sub-shot-noise accuracy by subtracting the intensity images of the two quantum-correlated beams. However, the average intensity of each beam puts a limit on the acceptable level of the dark noise in your detector, i.e. the average intensity must be larger than the detector dark noise. Typical photon-counting detectors can do this job well but do not readily offer spatial information. CCD cameras on the other hand often present a challenge for imaging weak optical fields due to their relatively slow frame rate (this makes it harder to mitigate low-frequency technical noises) and their intrinsic dark noise [58, 59].

There are several applications that require imaging with low-light illumination where counting individual photons become necessary. The accuracy of such detection is then determined by the photon statistics and by the technical noises, such as laser intensity fluctuations or the detector dark noise, and normally requires a long exposure detection to allow for statistical averaging.

In this chapter, we demonstrate a quantum-based imaging method reliant on analysis of the quantum field variance instead of the photon intensity that enables us to solve the problem of the dark noise at low illumination levels yet having better spatial reconstruction ability than traditional intensity-based measurements. In the presented experiments we use a quadrature squeezed vacuum field, containing very few photons on average. When such field interacts with an opaque object, it is quantum fluctuations in the obstructed zone are replaced with a regular vacuum.

The goal is to record the spatial distribution of the resulting noise quadrature even in the presents of strong dark noise. To do this, we mix the quantum probe with a classical local oscillator field to amplify its quantum noise, realizing a camera-based balanced homodyne detection, allowing us to image the fields with as low as one photon per frame while obtaining spatial details of the object with significantly less acquisition time, see Fig. 4.1. This makes it attractive for photosensitive applications like non-destructive imaging of biological samples [60]. Additionally, we can use an anti-squeezed quadrature, increasing the

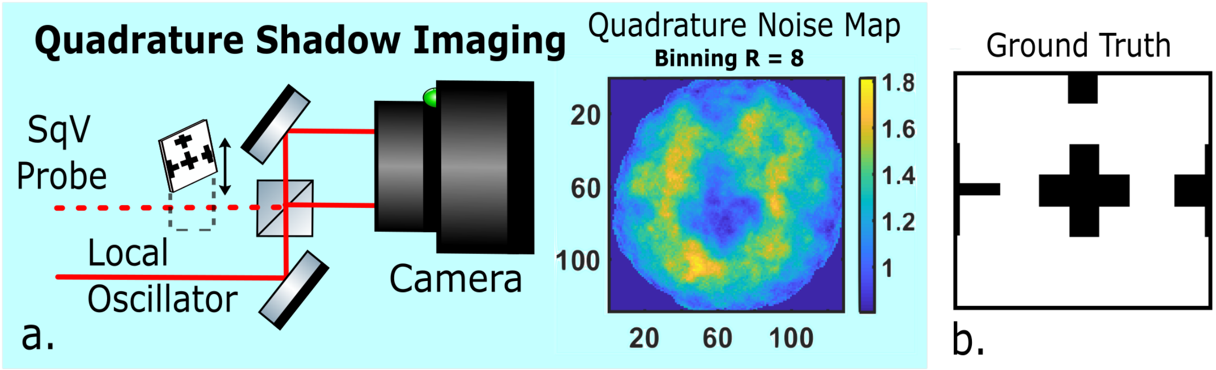

FIG. 4.1: A conceptual representation of the proposed quantum shadow imaging. Both schemes rely on camera images of the probe and reference beams to create the transmission map of an object. However, the quantum shadow method uses the average quantum fluctuations of the probe and reference fields, amplified by a local oscillator. The quantum shadow maps are on a linear scale.

tolerance to optical losses. The key advantage of this scheme is that the squeezed vacuum inherently has very few photons illuminating an object, so in low light conditions, our method outperforms coherent (laser) illumination with the same total number of photons when the detection noise is limited by the camera dark noise (see Figs. 4.6, 4.7, and 4.9).

4.2 Theoretical Framework

The concept of the proposed method is illustrated in Fig. 4.1. A CCD camera detects the number of photons incident on each pixel N on top of its internal dark noise N_d. For a standard intensity measurement, the boundary between a fully illuminated region (the average photocounts $\langle N + N_d\rangle$) and a fully blocked region (the average photocounts $\langle N_d\rangle$) can be distinguished by the difference between these two photocount values. We can sum the dark noise and shot noise counts since they are uncorrelated and estimate the signal-to-noise of intensity measurements as

$$\mathrm{SNR}_t = \frac{\bar{N}}{\sqrt{\bar{N} + 2(\Delta N_d)^2}}, \tag{4.1}$$

where $\bar{N}$ is an average photon number detected, and ΔN_d is the variance of the dark noise counts.

We propose instead to measure the normalized variance, V, of the quadrature $X_\theta = \cos(\theta)X_1+\sin(\theta)X_2$, where $X_1 = a+a^\dagger$, $X_2 = i(a^\dagger-a)$, and $a^\dagger(a)$ is the creation(annihilation) operator for the photon state. In this case, a similar boundary between the light and darkness can be detected via the deviation of the noise variance for the region, illuminated by a quantum probe, from unity - the noise variance of the coherent vacuum. For example, if an experiment uses a squeezed vacuum with the squeezing parameter r, the expected variance values for the squeezed and anti-squeezed quadratures are $V = e^{\mp 2r}$, correspondingly. We can also estimate the noise of such measurement by calculating the variance of the corresponding variance values for such a squeezed vacuum field, yielding the following theoretical signal-to-noise ratio:

$$\mathrm{SNR}_q = \frac{V-1}{\sqrt{2+V^2+V^4}}. \tag{4.2}$$

Note, that for this calculation we can neglect the camera dark noise thanks to the homodyne detection. As a result, we can compare the performance of the two approaches as a ratio of the two signal to noise values for an anti-squeezed vacuum field, and a coherent beam with similar average number of photons $\bar{N} \simeq \sinh^2(r) \ll 1$:

$$\begin{aligned} \frac{\mathrm{SNR}_q}{\mathrm{SNR}_t} &= \frac{e^{2r}-1}{\sqrt{2+e^{4r}+e^{8r}}} \frac{\sqrt{\sinh^2(r)+2(\Delta N_d)^2}}{\sinh^2(r)} \\ &\simeq \sqrt{1+\frac{2(\Delta N_d)^2}{\bar{N}}} \end{aligned} \tag{4.3}$$

It is easy to see that in the limit of the small photon number $\bar{N} \ll 1$, the two method perform equally well in the case of vanishing dark noise; however, if a dark noise becomes comparable with the average photon number, the advantage of the quantum, noise-based measurement becomes more obvious.

To reconstruct the image of the object, we calculate a transmission map $T(\vec{x})$, where $\vec{x}$ is the position of the detection area, traditionally calculated as a ratio of the average photon numbers in probe ($\bar{N}_p$) and reference ($\bar{N}_r$) beams:

$$T_t(\vec{x}) = \frac{\bar{N}_p(\vec{x})}{\bar{N}_r(\vec{x})}. \tag{4.4}$$

However, if the recorded images are overwhelmed by the dark noise, the resulting transmission maps are very noisy. At the same time, we can produce a better quality transmission map from the quantum noise measurements, since our detection method reduces the detrimental effect of the dark noise. We can connect the measured field variance, $V(\vec{x})$ to the object transmission, $|T(\vec{x})|^2$.

We derived equation 4.5 in Section 3.4, but for clarity I reproduced it below. Assuming that both squeezed state and local oscillator are single mode,

$$V(\vec{x}) = 1 + (e^{\pm 2r} - 1)\frac{|\mathcal{O}(\vec{x})|^2}{\sum_m |\mathcal{O}_m(\vec{x})|^2} \times |T(\vec{x})|^2, \tag{4.5}$$

where $\mathcal{O}(\vec{x}) = \int_A u_{\mathrm{LO}} u_{SqV} \mathrm{d}A$ is the overlap between the spatial modes of the local oscillator, u_{LO}, and the squeezed vacuum mode, u_{SqV}, and A is the detection area at location $\vec{x}$. For the reference beam, where the object is removed, we assume $T = 1$ everywhere. For the mode-matched local oscillator and the quantum probe, we arrive at the following expression of the transmission map using measured quadrature noise variance V_p and V_r in the probe and reference beams, correspondingly:

$$|T_q(\vec{x})|^2 = \frac{V_p(\vec{x}) - 1}{V_r(\vec{x}) - 1}. \tag{4.6}$$

Note that our method of transmission calculation is agnostic to the choice of the squeezed or anti-squeezed quadrature. In this experiment, we work with the anti-squeezed quadrature, since it is more robust to the optical losses.

4.3 Experimental Setup

4.3.1 Generating Squeezing

The schematics of the experimental realization of the proposed method is shown in Fig. 4.2. We generate the squeezed vacuum using a squeezer based on the polarization self-rotation in a ^{87}Rb vapor cell [44, 61, 62, 63]. An external cavity diode laser (30 mW, $\lambda \approx 795$ nm), detuned near the ^{87}Rb $5S_{1/2}, F = 2 \rightarrow 5P_{1/2}, F = 2$, passes through an optical isolator and then to an acousto-optical modulator (AOM). The light is coupled into a single-mode optical fiber that acts as a spatial filter so we can work with a clean, single-mode, gaussian beam.

Next, the light passes through a half-wave plate and polarizer that controls the polarization and intensity going into the atomic vapor cell. The polarized pump is attenuated to 7 mW and is focused into the ^{87}Rb vapor cell heated to 65° C, using a 400 mm lens. The cell rests in the trilayer, metal shield to minimize effects from external magnetic fields, and the atomic density is controlled by heating the vapor using a resistive heater wrapped around one layer of the shielding. There the nonlinear interaction described in Section 2.6.1 takes place and a squeezed vacuum is generated co-linearly, but orthogonally polarized, with the pump. A second 200 mm lens columnates the beam.

When the squeezed vacuum propagates unobscured to the homodyne detector, we are able to directly measure the squeezed and antisqueezed quadratures of the field by sweeping the phase between the LO and SqV using a PZT mounted on one of the polarizing beam displacers. Right after the squeezer, we detect -1.5 dB of quantum noise suppression

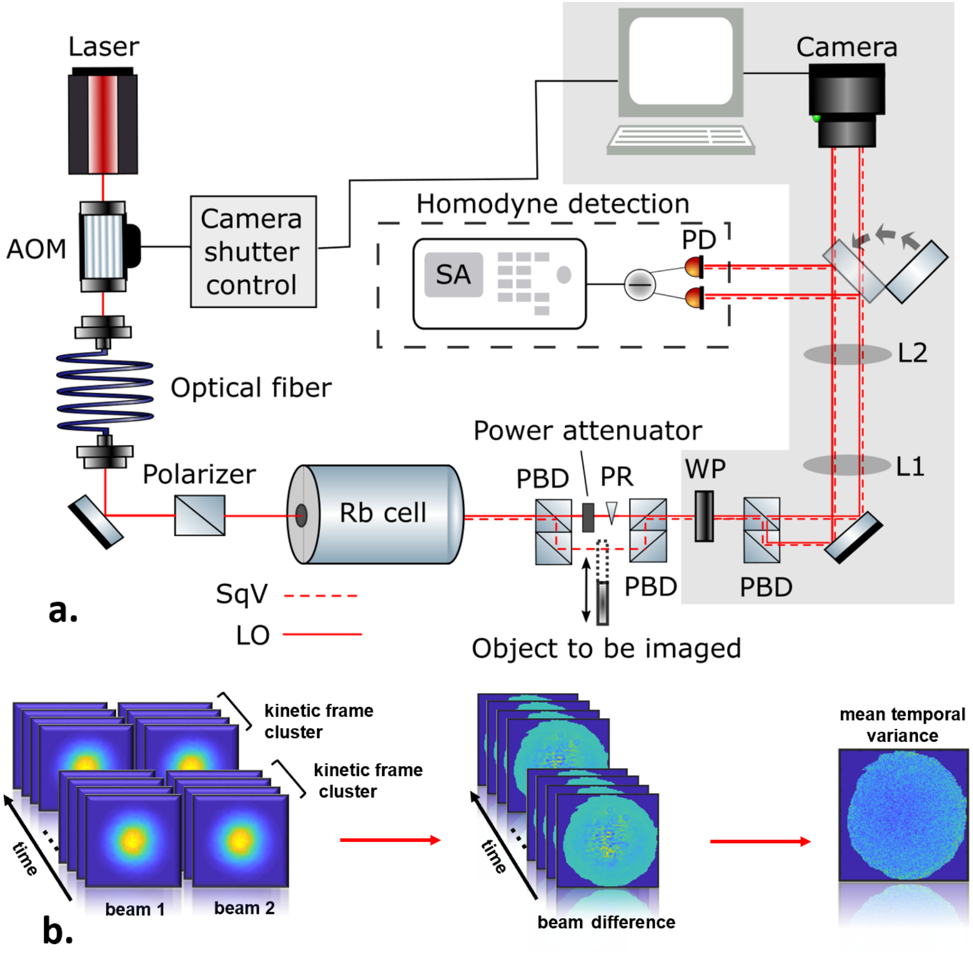

FIG. 4.2: a) Experimental setup with two different detection schemes: traditional homodyne and camera. SqV denotes the squeezed vacuum, LO denotes the local oscillator, PR is phase retarder, AOM is an acousto-optical modulator, and PBD is a polarizing beam displacer. Objects may be placed in the path of the squeezed vacuum where lenses L1 and L2 map the object image onto the camera. PDs are photodiodes, SA is a spectrum analyzer, the camera is connected to a computer. b) pictorial representation of the image analysis done to creat the quantum noise maps

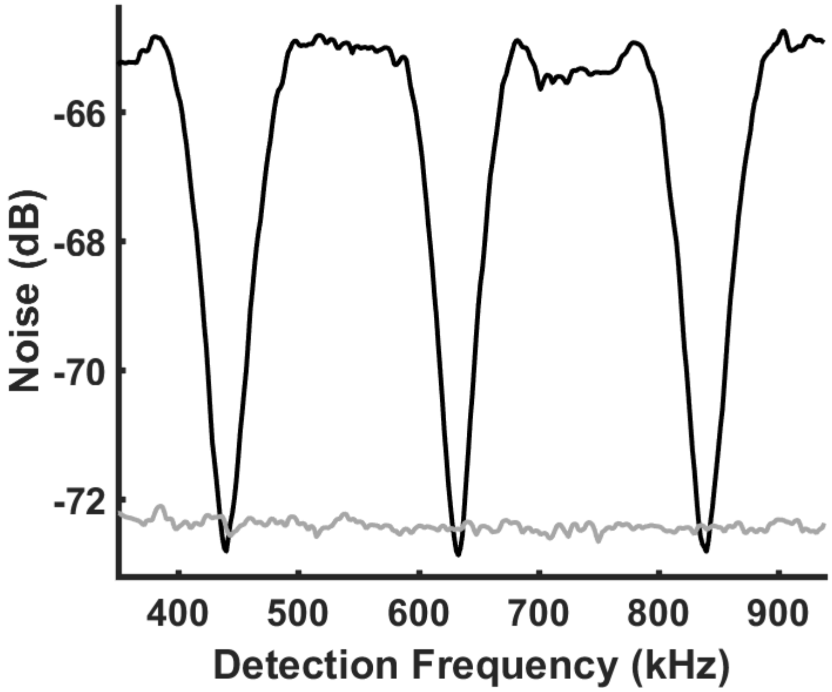

FIG. 4.3: Squeezing measured using a traditional homodyne detector. The gray line shows the shot noise level and the black curve shows the squeezed (minimum noise) and antisqueezed quadratures (maximum noise). We measured -0.5 dBs of squeezing and 7.5 dBs of antisqueezing.

in the squeezed quadrature and 10 dB in the anti-squeezed quadrature. Due to optical losses in the imaging optics (mainly in the uncoated polarizing beam displacers), after the imaging system, we detect (with homodyning photodiodes) only 0.5 dB squeezing and 7.5 dB anti-squeezing at the imaging end Fig. 4.3 shows a typical noise trace from the spectrum analyzer where the gray line is shot noise and the black is the quantum noise as we sweep through the different quadratures.

4.3.2 Camera Operation

We use a Princeton Instrument Pixis 1024 CCD camera for all of the image collection. This camera has a very high quantum efficiency (>95%) which allows us to use the photo counts in our statistical analysis of the quantum noise in our image. In addition, the camera has a very low dark noise of 10 counts per μs.

To avoid camera over-exposure, the pump field is pulsed for only 1 μs during the 544 μs duty cycle using an acousto-optical modulator (AOM). Note that pulsed operation doesn't affect the generation of squeezing (i.e. there are no concerning transient effects) and only keeps the pump from saturating the camera.

4.3.3 Imaging

After the squeezer, the pump and squeezed vacuum (SqV) fields are physically separated using a polarizing beam displacer (PBD). SqV alone passes through the object and then recombines with an attenuated pump field which now serves as a local oscillator (LO) in the imaging balanced homodyning scheme. There is no need for external phase stabilization between the local oscillator and the squeezed vacuum. Because the same pump that is used to generate the SqV is the LO they are phase-locked and the only source of phase instability would come from the interferometer. We minimize those effects by creating the smallest possible arm length (about 6 cm) in the interferometer by using compact polarizing beam displacers. We image the object onto the camera using a 4-f system of lenses (see L1 and L2 in Fig. 4.2).

We obtain quantum-limited statistics from images of the two beams on the CCD camera described in section 4.3.2. This camera can only rapidly capture six frames before having to pause for half a second for data transfer. We discard the first and last frames of the series Thus, we collect four frames, separated by 544μs (synchronized with the pulsed laser) that form "kinetic clusters". To extract the information about the quantum noise variance, we subtract the intensities of the two beams after the final beamsplitter (labeled “1” and “2”) to create an amplified noise map - a 2D analog of the differential photo-currents in a traditional homodyne detection scheme. For most measurements, we

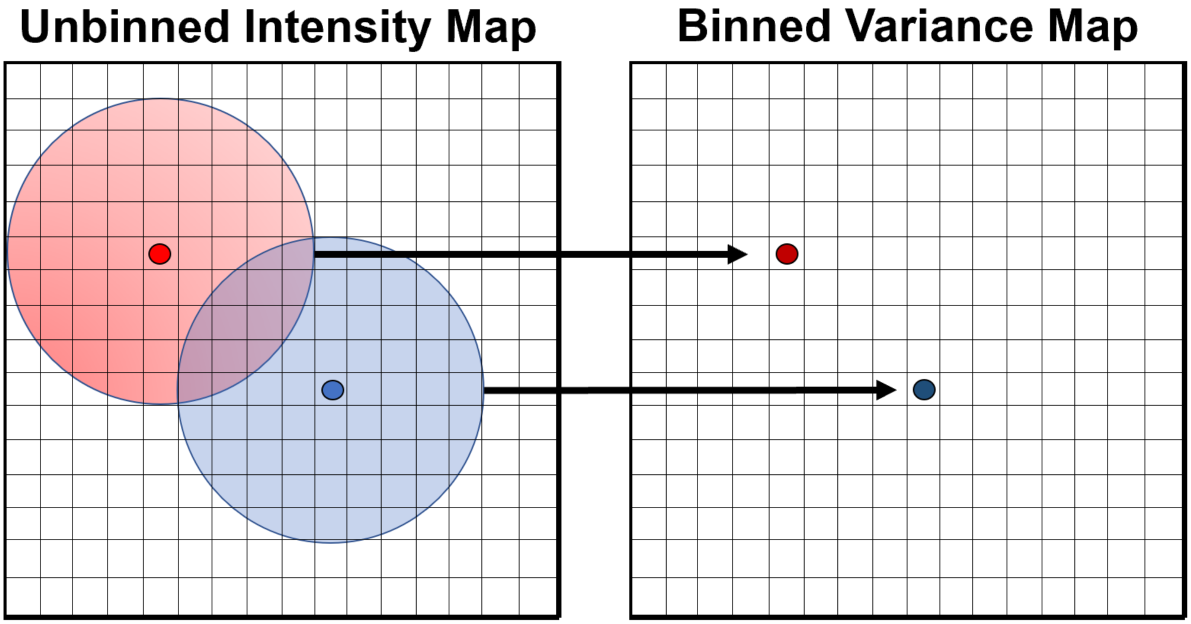

FIG. 4.4: Pictorial illustration of the experimental binning process.

also need to increase the effective detection area, as discussed below. To do that, for each point $\vec{x} = (x, y)$ we sum all the counts in the radius R around it to calculate the total photon counts $N_{1,2}^{(\mathrm{R})}(\vec{x})$ – a process we refer to as "binning" (see Fig. 4.4). Next, we calculate the image of the quantum fluctuations variance $V^{(\mathrm{R})}(x, y)$ normalized to the shot noise and temporally-average over a given kinetic cluster:

$$V^{(\mathrm{R})}(\vec{x}) = \frac{\left\langle \left(N_1^{(\mathrm{R})}(\vec{x}) - N_2^{(\mathrm{R})}(\vec{x}) \right)^2 \right\rangle}{\left\langle N_1^{(\mathrm{R})}(\vec{x}) + N_2^{(\mathrm{R})}(\vec{x}) \right\rangle} \tag{4.7}$$

where the average is taken within the four frames of each kinetic cluster. Finally, we average the variance maps over all the kinetic clusters for a given set of experimental parameters to produce an average normalized quantum noise map of our squeezed vacuum, as seen in the first column of Fig. 4.6.

4.3.4 Squeezed Vacuum Mode Characterization

If the detection area is much smaller than the mode size of the squeezed vacuum, it will be seen as a large loss in the system, and degrade any non-classical noise statistics down to shot noise, as seen in Fig. 4.6 (a). To avoid this, it is necessary to sum the photo counts over multiple pixels (i.e. bin pixels together) in order to match the size of the detection area to the characteristic quantum-mode size inside the squeezed vacuum beam [57], and thus provides more efficient quantum fluctuation detection. For example, Fig. 4.6 (e), (i), and (m) show a clear increase in the measured quantum noise variance, confirming that we have a squeezed mode much larger than the camera pixel size.

We can deduce the number of modes in the images of our unobscured by calculating the mean variance for a particular bin size. Figure 4.5 shows how the mean variance increases consistently as the binning area increases. This suggests that we are working with a single-mode field. If we were dealing with a multimode beam, we would expect the noise to plateau once the mode size matched the bin size.

4.4 Results

To experimentally demonstrate the imaging technique with the squeezed vacuum, we insert a completely opaque rectangle as our mask to block approximately one quadrant of the probe beam as our test object to be inserted only in the squeezed vacuum channel (see Fig. 4.2). Fig. 4.6 shows the examples of measured variance maps for both reference and probe beams for different beam binning. Fig. 4.6 (column four) shows a cross-section of the experimental quantum shadow transmission map at the location of the red line and compares it with the calculated transmission map of an ideal noiseless beam sampled with the same detection area of radius R. As discussed above, when the radius (R) of

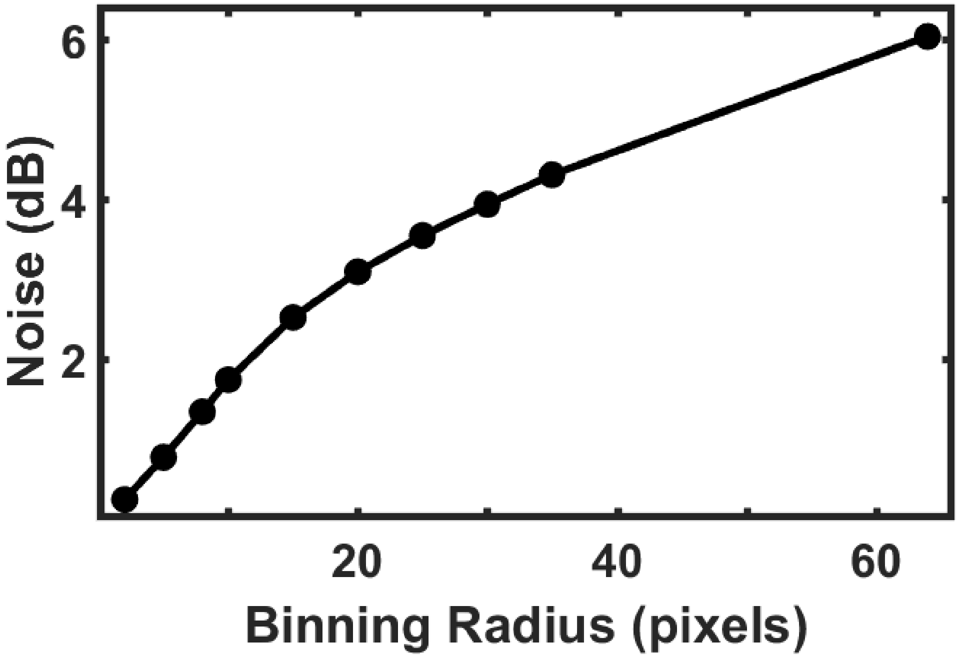

FIG. 4.5: Average binned noise in an image for a given bin size.

the sampling the area is small (top) it is impossible to see the quantum shadow, since the detected quantum statistics is indistinguishable from a shot-noise limited beam [64]. However, as we increase detection area radius (top to bottom rows), the difference in quantum statistics between the blocked and open regions of the mask become more and more pronounced, creating a resolvable "quantum shadow". Such improvement, however, comes with the price of somewhat reduced "sharpness" of the image features. This is because the spatial resolution of the quantum noise maps is inversely proportional to the size of the detection area, while the contrast of the edge is proportional to the detection area. The spatial resolution is also tied to the size of the squeezed mode, as discussed in Eq. (4.5), since the size of the detection area needs to correspond to the size of the mode for the best contrast. Thus, in general, a non-overlapping multimode squeezed field with a small mode size is more attractive for imaging applications, compared to a single-mode optical field. Some information about the mode decomposition of our squeezed vacuum

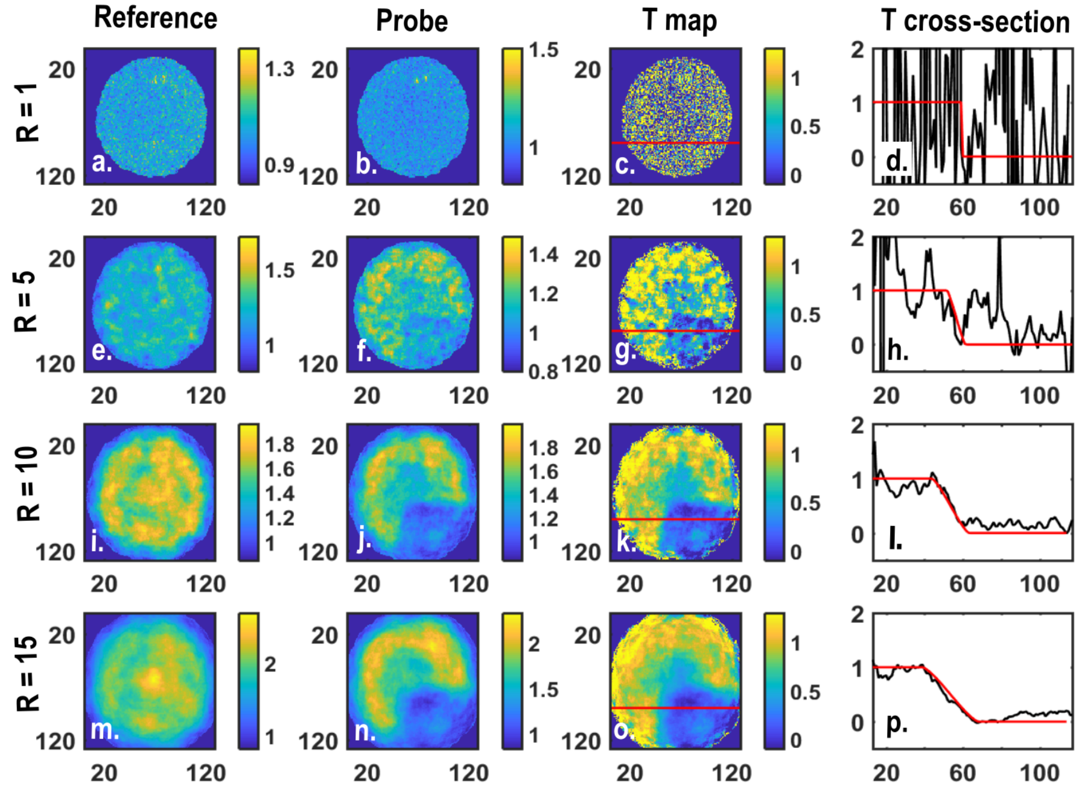

FIG. 4.6: The first column (a, e, i, m) shows the noise maps (defined with Eq. 4.7) of the squeezed vacuum with no objects in the vacuum port. The second column (b, f, j, n) shows the noise maps for the squeezed vacuum with the mask in the vacuum port. The third column (c, g, k, o) shows the transmission map, T, as defined in Eq. 4.6. In the final column, the black line shows transmissions through the mask in the T maps where the red line contrasts the noiseless classical intensity cross-section through the same region for the same detection area. The first row (a, b, c, d) has a detection area with a radius of R = 1, the second row (e, f, g, h) has a detection area of R = 5, the third row (i, j, k, l) has a detection area with a radius of R = 10, and the last row (m, n, o, p) has a detection area with a radius of R = 15. The reference and probe maps are on a dB scale.

field may be gleaned from the first column of images in Fig. 4.6. If our reference beam was in the single-mode matching the LO, we would expect it to have a normalized variance proportional to the overlap parameter of a fundamental Gaussian spatial mode with itself according to Eq. 4.5. However, a clear ring-like structure emerges as we increase the detection area, suggesting the presence of weaker higher-order modes. Nevertheless, our close-to single-mode squeezer demonstrates quite good visibility of the image.

To quantify the quality of our quantum noise images, we calculate the similarity

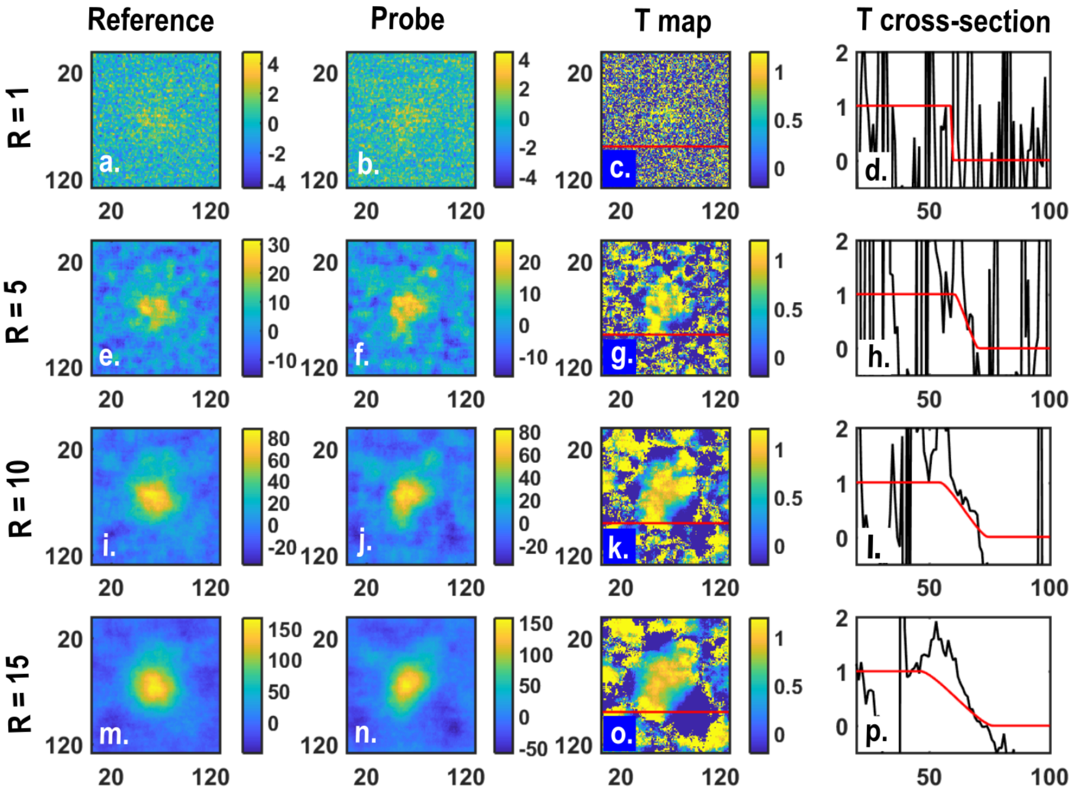

FIG. 4.7: Traditional imaging with 250 photons per frame. The first column (a, e, i, m) shows the ordinary intensity image of the beam with no objects in the port. The second column (b, f, j, n) column shows the intensity images for the beam with the mask in the port. The third column (c, g, k, o) shows the transmission map, T, as defined in Eq. 4.4. In the final column, the black line shows transmissions through the mask in the T maps where the red line contrasts the noiseless classical intensity cross-section through the same region for the same detection area. The first row (a, b, c, d) has a detection area with a radius of R = 1, the second row (e, f, g, h) has a detection area of R = 5, the third row (i, j, k, l) has a detection area with a radius of R = 10, and the last row (m, n, o, p) has a detection area with a radius of R = 15. The reference and probe maps are on a photon count scale.

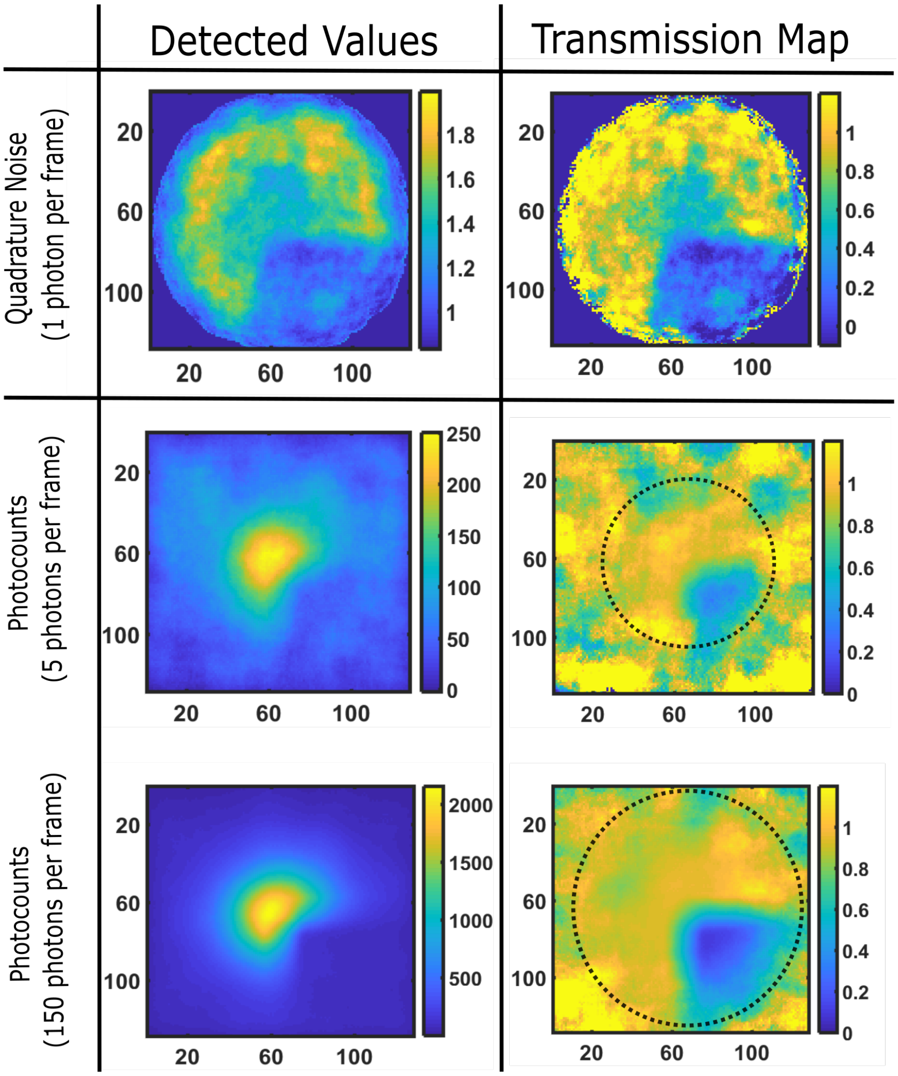

FIG. 4.8: Comparison of the quantum shadow imaging to classical direct intensity imaging. Every image uses statistics from 800 frames, the transmission map utilizes 1600 frames: 800 frames for the shadow and 800 for the reference image. Row one shows the quantum shadow image and transmission map with 1 photon per frame. The classical image and trans- mission map using 5 photons per frame is shown in row two. Similarly, images in row three use 150 photons per frame. The dashed circle encloses points where the optical signal is equal to or greater than the dark noise (SNR ≥ 1). In all cases, the probe and the local oscillator (for the quantum shadow) beams have the same beam full-width half maximum of 38 pixels

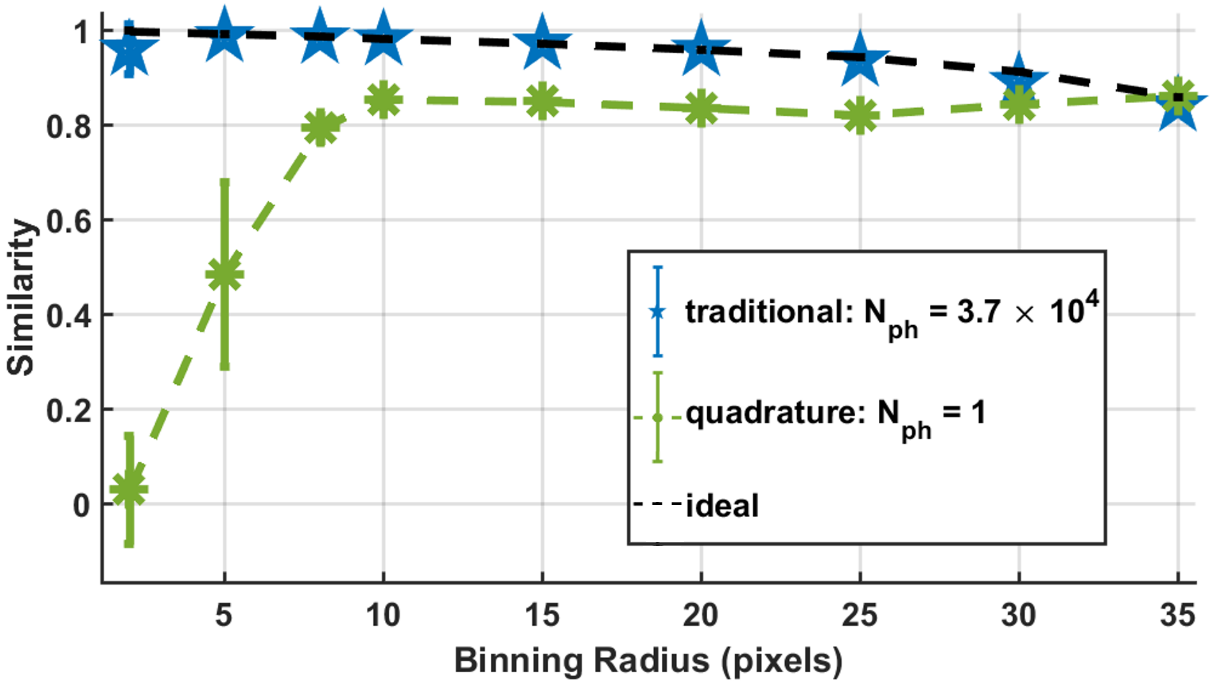

FIG. 4.9: The similarity of our imaging method as a function of detection radius. Each data set corresponds to a different total photon number (N_{ph}) used to illuminate the image. The black dotted line shows the best similarity possible with our method assuming a perfectly noiseless image. We theoretically calculate $N_{\mathrm{ph}}^{\mathrm{quad}} = N_{\mathrm{sq}} \times t_{\mathrm{expo}}/t_{\mathrm{coherence}}$, where $N_{\mathrm{sq}} = 1$ is the number of photons in a squeezed mode with 7.5 dBs of anti-squeezing (assuming a single mode), $t_{\mathrm{expo}} = 2 \times 10^{-6} s$ is the exposure time of a frame and $t_{\mathrm{coherence}} = 2.5 \times 10^{-6} s$ is the coherence time of the squeezing. The similarity was calculated over an 80-pixel span centered around the edge of the mask.

defined as

$$S = \frac{\sum T_{\mathrm{exp}} T_{\mathrm{o}}}{\sqrt{\sum T_{\mathrm{exp}}^2 \sum T_{\mathrm{o}}^2}}, \tag{4.8}$$

where T_{exp} is the experimentally measured transmission, T_{o} is the true object transmission, and the sum is taken for pixels along a path across the image (we use horizontal straight line shown in red in Fig. 4.6). This metric allows us to quantify how well our noise analysis reconstructs the image of an object. To compare this to the traditional imaging method (see Fig. 4.1), we did several measurements with a weak coherent field as illuminating source shown in Fig. 4.7. We can see that the dark noise of the camera dominates the signal (see top row) and even the beam shape is barely resolvable. As we increase the radius of the sample area, the details of the beam become more visible, but even for the radius of 15 pixels, it is hard to see the mask shape.

We see that the quantum noise images have better similarity after a certain binning and overall reflect the mask shape better for significantly lower photon numbers (we estimate that we have about 1 photon per frame in the squeezed vacuum field). This is because we can boost our quantum noise above the dark noise using a homodyne-like detection scheme and our squeezed photons have correlations that allow us to reconstruct the image from the noise using less object illuminating resources (photons). It is difficult to compare the noise shadow imaging method to other quantum imaging methods because they focus on enhancing preexisting techniques and comparing SNRs, but our method has no direct classical counterpart capable to operate at such low illumination and high dark count noise levels.

4.5 Conclusion

In conclusion, we can image an opaque object by illuminating it with a squeezed vacuum. Our scheme can use the anti-squeezed quadrature which makes the whole method more robust against optical and detection losses. We can reconstruct the object by analyzing the quantum noise statistics that change spatially depending on the mode structure of the squeezed vacuum and the object. This has application in any imaging scenario where a high photon number could damage the object, such as biological imaging. Also, the overall scheme is quite simple and outperforms the traditional counterpart even when the allowed number of illuminating photons is larger by a factor of 150.

We also note that this method has the potential to be generalized to other quantum states, e.g. a thermal state since it only depends on the state's deviation from the shot noise. Since our method is based on analysis of the quantum state variance, it is potentially immune to the parasitic illumination by classical light sources for which the quadrature variance is independent of transmission since stray light does not match the local oscillator mode will not contribute to the measured quadrature noise. While we have used a simple opaque object, the method is more general and can be used on semitransparent samples as well. Analyzing such samples is left for future work.

CHAPTER 5

Single-Pixel Imaging for Quantum Fields

Single-pixel imaging is a relatively new, classical imaging technique that allows you to gather spatial information about a scene or object you want to image using only a single-pixel camera, i.e. a photodiode. This form of imaging is very attractive because it has the ability to capture images at high frame rates, at wavelengths outside of current image sensor capabilities, and in three dimensions.

While we have demonstrated noise-based imaging using a camera in Chapter 4, oftentimes there may not be the necessary equipment at the wavelength you wish to interrogate your sample with. Additionally, cameras are quite slow making it is difficult to get useful phase information from them. Single-pixel imaging [65] provides a simple solution to these issues. This technique, developed alongside compressive sensing [66, 67, 68], is a way of sampling an image using only a photodiode (single-pixel camera) and then reconstructing the image. In this chapter, we will explore how to use single-pixel imaging techniques to reconstruct a quantum field.

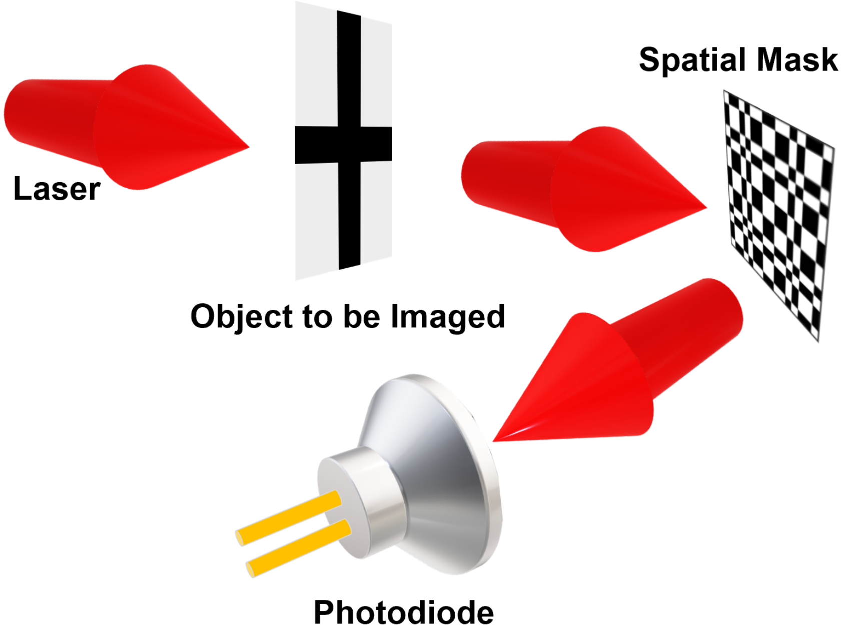

FIG. 5.1: Classical single-pixel imaging setup. A light source illuminates a scene (the "+") and then passes through a spatial filter before being detected on a photodiode.

5.1 Basic Theory of Single-pixel Intensity Imaging

In single-pixel intensity imaging, a light source illuminates a scene and is then collected onto a photodiode using a form of structured detection. One common form of structured detection is raster scanning, where a pinhole scans through the image plane and collects the intensity of the illuminating field. The scene can then be reconstructed, pixel by pixel, based on the intensity measured with the photodiode at each pinhole location. Another form of structured detection involves creating patterns of pixels (sampling masks) and measuring the total intensity of light passing through instead of the intensity from a single pinhole. With a sufficient number of sampling masks, the scene can then be reconstructed by summing the masks weighted by the measured intensity. A basic sketch of the structured detection scheme is shown in Fig. 5.1 and Fig. 5.2.

To classically reconstruct a scene with N total pixels, you are be required to have $M = N$ different patterns. But, the number of masks may be higher ($M >> N$) if your measurements are subject to noise or your sampling set contains non-orthonormal masks [65]. Your number of sampling masks may also be less than the total number of pixels ($M < N$) if your image is sparse in the sampling basis. This is known as compressive sensing since you do not need information about each pixel to reconstruct the image.

For convenience, the most commonly used set of orthonormal patterned masks is the Hadamard modes. We can write our reconstructed signal (field intensity), $\tilde{u}_{\text{in}}(x, y)$, as linear decomposition of the Hadamard modes, $\tilde{u}_{\text{in}}(x, y) = \sum_i w_i H_i(x, y)$. After the probe illuminates the scene, which has an intensity transmission, $T(x, y)$, we can measure the transmitted signal's (field intensity), $\mathcal{S} = \tilde{u}_{\text{in}}(x, y)T(x, y)$ projection onto $H_i(x, y)$ and collect the new set of weights, $w_i = \int_A \mathcal{S}(x, y)H_i(x, y)ds$, associated with the transmitted signal. We approximate this integral as a sum over all the pixels, p,

$$w_i = \sum_p \mathcal{S}(p)H_i(p). \tag{5.1}$$

Finally, we can write the reconstructed transmitted field intensity, $\mathcal{S}$, at every pixel using the Hadamard modes as our sampling set as

$$\mathcal{S}(p) = \frac{1}{\text{M}} \sum_{\text{m}=1}^{\text{M}} w_{\text{m}} H_{\text{m}}(p), \tag{5.2}$$

where M is the number sampled masks, H_{m} is the Hadamard mask, and w_{m} is the photocurrent (i.e. weight) measured for the mask. Fig. 5.2 illustrates the process.

5.2 Classical Field Reconstruction

By using homodyne detection, we can reconstruct the field and move beyond simple intensity reconstruction. We can use a similar analysis to reconstruction the classical

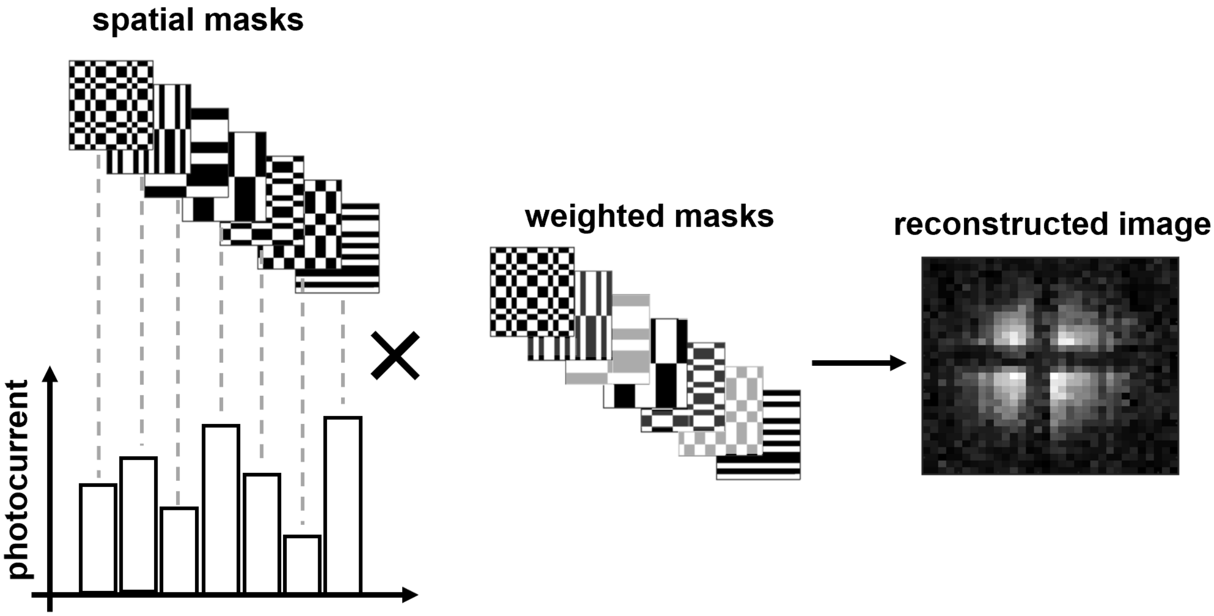

FIG. 5.2: Illustration of classical image reconstruction process. Each mask produces a photocurrent that acts as its weight in the image reconstruction described by Eq. 5.2.

field by analyzing the interference between a weak input field and a local oscillator. In Chapter 3, we derived the differential signal to be Eq. 3.4. Since we are working with a classical field, we can write

$$i_{-}(t) \propto |\mathcal{O}| \cos(\phi), \tag{5.3}$$

where $\mathcal{O} = \int_A (u_{\mathrm{LO}}^* u_{\mathrm{in}})\, ds$ is the overlap of the local oscillator and weak field as defined in Eq. 3.8 of Chapter 3. This can be approximated as the sum, $\mathcal{O} = \sum_m \mathcal{O}_m$, where $\mathcal{O}_m = \sum_p u_{\mathrm{LO}} u_{\mathrm{in}} H_m(p)$, and p are the number of pixels in your Hadamard mask. When the masked local oscillator has a strong overlap with the input field, the differential signal will increase. Since single pixel imaging requires us to weight each basis element (Hadamard mode), we define our weight, $\mathcal{C}_m(\phi)$, according to Eq. 5.3,

$$\mathcal{C}_m(\phi) = |\mathcal{C}_m| \cos(\phi - \phi_m) = i_{-,m} \cos(\phi - \phi_m) \tag{5.4}$$

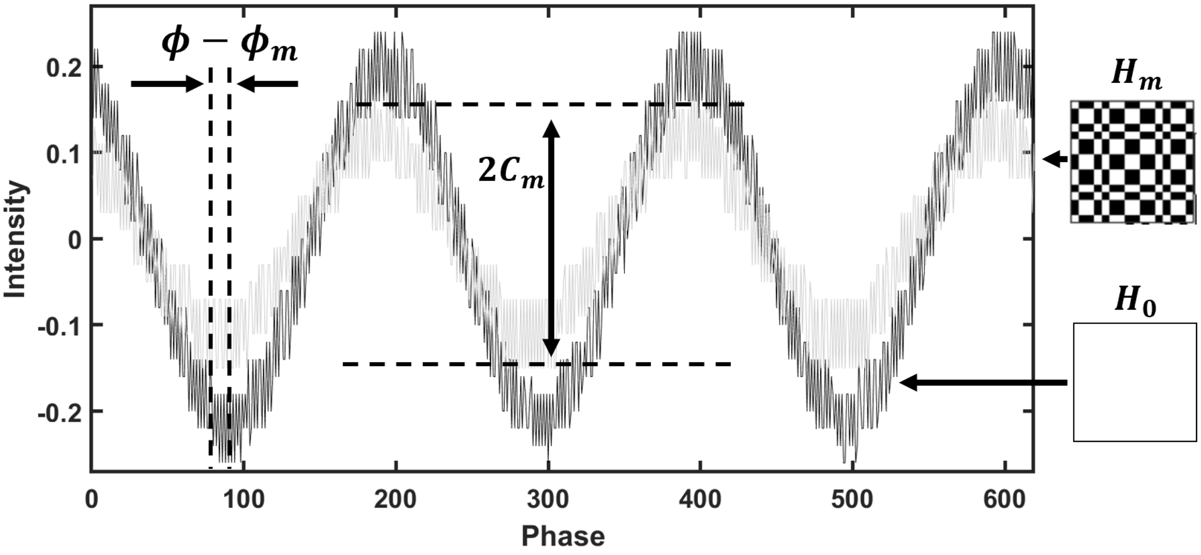

FIG. 5.3: Example of the classical interference fringes in the differential signal, $i_-(t)$, between the local oscillator and the weak input field for two different Hadamard masks.

Figure 5.3 shows an example of the classical interference fringes measured at the output of the interferometer. We should note that although the spatial phase dependance isn't explictly written in $\mathcal{C}_m$, it is implied since the current is a function of the overlap which is spatially dependent.

We take this into account and classically reconstruct our field times the local oscillator, $\mathcal{S} = u_{\mathrm{LO}}u_{\mathrm{in}}$, by the following formula:

$$\mathcal{S}(x,y) = \frac{1}{\mathrm{M}}\sum_{\mathrm{m}=1}^{\mathrm{M}} |\mathcal{C}_m| e^{i\phi_m} H_{\mathrm{m}}(x,y). \tag{5.5}$$

But we approximate it as $\mathcal{S}(p) = \frac{1}{\mathrm{M}}\sum_{\mathrm{m}=1}^{\mathrm{M}} \mathcal{C}_m e^{i\phi_m} H_{\mathrm{m}}(p)$, where p is the pixel of the Hadamard mask. Where H_m is the Hadamard mode, and $\mathcal{C}_m$ is the coefficient determined by the interference between the LO and weak input field, and ϕ is the common phase of the local oscillator phase.

5.3 Single-Pixel Imaging Expanded to Quantum Fields

Single-pixel intensity and field reconstruction using classical light, as shown in Section 5.1 and 5.2, is straightforward, since we can easily measure the weights by monitoring the change in intensity and phase. What happens though when we illuminate the scene with a quantum field? Expanding the idea of single pixel classical field reconstruction to the quantum regime can be useful for many of the same examples discussed in Chapter 4, predominately low-light imaging. If we use the squeezed vacuum to illuminate an object we can then track how the noise changes as a function of the overlap with the local oscillator - very similar to the classical case described in Section 5.2. How do we reconstruct the field, u_{in}, based on quantum noise measurements?

To measure the noise, we need to use a homodyne detector that takes into account the spatial information about the beams like explored in Chapter 3. Note: we realize that we cannot reconstruct u_{in} alone, but rather its product with the local oscillator, $\mathcal{S} = u_{\text{LO}} u_{\text{in}}$. The variance of field can be written as

$$V(\phi) = 1 + \sum_n (V_{in,n}(\phi_n) - 1) |\mathcal{O}_n(x,y) \otimes T(x,y)|^2. \tag{5.6}$$

$V_{in,n}$ is the variance of the n^{th} spatial noise mode of the input probe field, ϕ_n is the phase between the n^{th} probe field mode and local oscillator, $\mathcal{O}(x,y) \otimes T(x,y) = \int_{-\infty}^{\infty} u_{\text{LO}} u_{\text{in}} T(x,y) ds$ is the overlap between the probe, the local oscillator, and T – the transmission of the probe through the scene you would like to image. The overlap will depend on which spatial mode we place on our local oscillator. Also note, since we are collecting all the light, we assume that we are summing over all the overlaps which are measured on an effectively infinite detector ($A = \infty$). This implies $\sum_m |\mathcal{O}|^2 = 1$ (see Section 3.2). We will consider two different cases (1) a single-mode squeezed vacuum with a mode-match local oscillator, and

(2) a multi-mode squeezed vacuum.

5.3.1 Single-mode squeezed vacuum probe with a mode-match local oscillator

Assume there is no object in the probe path, so $T = 1$ everywhere, and we measure the variance of the input probe that is overlapped with the local oscillator. Similar to Eq. 5.3, we can explicitly write the phase dependence of Eq. 5.6 as

$$V_m(\phi) = 1 + (V_{\text{in}}^{(\max)} \cos^2(\phi - \phi_m) + V_{\text{in}}^{(\min)} \sin^2(\phi - \phi_m) - 1)|\mathcal{O}_m|^2, \tag{5.7}$$

(derived in Chapter 3)since we can sweep through ϕ, the common phase of the local oscillator phase, and measure the maximum/minimum of $V_m(\phi)$. Here, the m is the index of the Hadamard mode.

All of the spatial information is encoded in the overlap term

$$\mathcal{O}_m = \int_{-\infty}^{\infty} u_{\text{LO}} H_{\text{m}} u_{\text{in}} ds, \tag{5.8}$$

and approximate the overlap as a sum across all the pixels of the Hadamard mode

$$\mathcal{O}_m = \sum_p u_{\text{LO}}(p) u_{\text{in}}(p) H_m(p). \tag{5.9}$$

For the case with single-mode squeezing and mode matched local oscillator, when $m = 0$,

$$V_0(\phi) = V_{\text{in}}^{(\max)} \cos^2(\phi - \phi_0) + V_{\text{in}}^{(\min)} \sin^2(\phi - \phi_0), \tag{5.10}$$

since the overlap is 1 because is $H_0(p) = 1$. Now we can express $\mathcal{O}$ in terms of our quadrature noise measurements

$$\mathcal{O}_m = \sqrt{\frac{V_m(\phi_m) - 1}{V_0(\phi_0) - 1}} \tag{5.11}$$

Analogous to Eq. 5.4, we define the weight of our reconstructed field as

$$\mathcal{V}_m = |\mathcal{O}_m| = \left[\frac{V_m - 1}{V_0 - 1}\right]^{1/2} e^{i\phi_m/2}. \tag{5.12}$$

Finally we can write the reconstructed the product of our input field and the local oscillator as

$$\mathcal{S}(p) = \frac{1}{\mathrm{M}} \sum_{\mathrm{m}=1}^{\mathrm{M}} \mathcal{V}_{\mathrm{m}} H_{\mathrm{m}}(p) = \frac{1}{\mathrm{M}} \sum_{\mathrm{m}=1}^{\mathrm{M}} \left[\frac{V_m - 1}{V_0 - 1}\right]^{1/2} e^{i\phi_m/2} H_{\mathrm{m}}(p) \tag{5.13}$$

5.3.2 Multi-mode squeezed vacuum

For the multi-mode case, things become tricky. Now, we measure the quadrature noise from the sum of each contributing squeezed spatial mode

$$V_m(\phi) = 1 + \sum_n (V_{\mathrm{in},n}^{(\mathrm{max})} \cos^2(\phi) + V_{\mathrm{in},n}^{(\mathrm{min})} \sin^2(\phi) - 1) |\mathcal{O}(x,y)_{m,n}|^2, \tag{5.14}$$

where $V_{in,n}$ is the noise amplitude for the n^{th} squeezed mode. Using the same procedure as the single mode case, we find

$$\mathcal{O}_{m,n} = \sum_p u_{\mathrm{in,n}} u_{\mathrm{LO}} H_m. \tag{5.15}$$

Its not possible to extract any spatial information about the product of $u_{\mathrm{in}} u_{\mathrm{LO}}$ unless we have n unique measurements, which are not available in our current experiment.

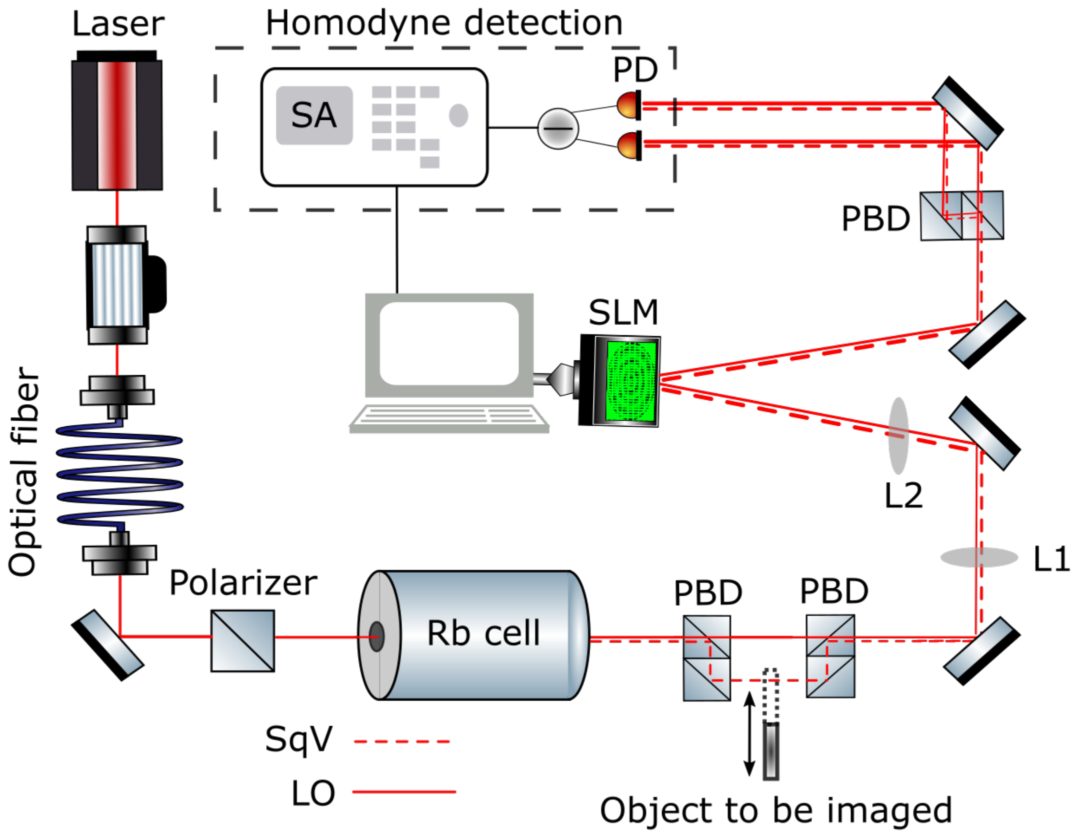

FIG. 5.4: Single-pixel quadrature noise imaging experimental setup. SqV denotes the squeezed vacuum, LO denotes the local oscillator, and PBD is a polarizing beam displacer. Objects may be placed in the path of the squeezed vacuum where lenses L1 (100 mm focal length) and L2 (300 mm focal length) map the object image onto the SLM, PDs are photodiodes, and SA is a spectrum analyzer. We use a PZT controlled by a high voltage supply to change the path length difference in the interferometer. This allows us to tune between the squeezed and antisqueezed quadratures.

5.4 Experimental Setup

To experimentally implement the quantum field reconstruction, we generate squeezing using polarization self-rotation in a cell of rubidium vapor, similar to the experiment in Chapter 4. The squeezed vacuum is separated from the pump using a polarizing beam displacer (PBD) so that it can independently probe a scene and then be spatially overlapped with the pump which now acts as the local oscillator. The two beams are now colinear (see Fig. 5.4 for the complete setup).

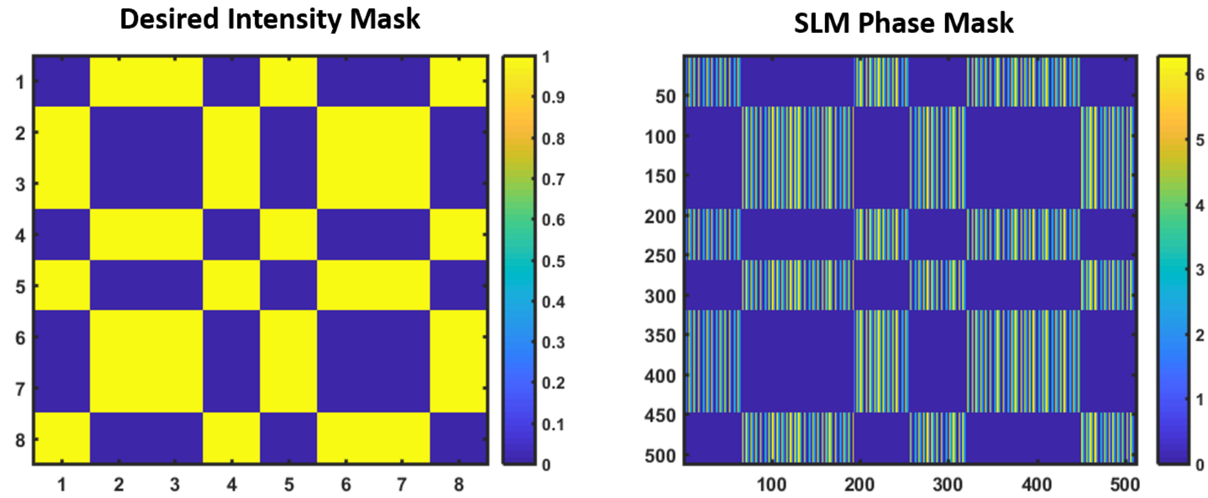

FIG. 5.5: Examples of the intensity mask we wish to impart onto the local oscillator compared to the phase mask we send to the SLM to generate the spatial profile.

Two lenses are used to image the object onto a 512×512 pixel Meadowlark spatial light modulator (SLM) where a spatial intensity mask is placed onto the local oscillator. The SLM works by applying a phase grating across the face of the beam causing portions of the beam to be deflected out of the optical path. Figure 5.5 shows an example of an SLM phase mask for a given intensity mask. Even though both the squeezed vacuum and local oscillator are reflected off the SLM only the local oscillator is affected since the SLM is polarization sensitive and we tune the LO polarization to be the active one. Our noise still obeys Eq. 3.10. Adding a mask to the local oscillator modifies the overlap between the local oscillator and the squeezed probe, and hence will modify the noise we measure on the photodiodes. Figure 5.9 shows an example of the quantum noise for two different spatial masks.

We use the Hadamard modes as our sampling basis [69]. These modes consist of a ±1 tiling generated using the Hadamard matrix. The Hadamard matrix is defined recursively as

$$H'_{i+1} = \begin{bmatrix} H'_i & H'_i \\ H'_i & -H'_i \end{bmatrix}, \tag{5.16}$$

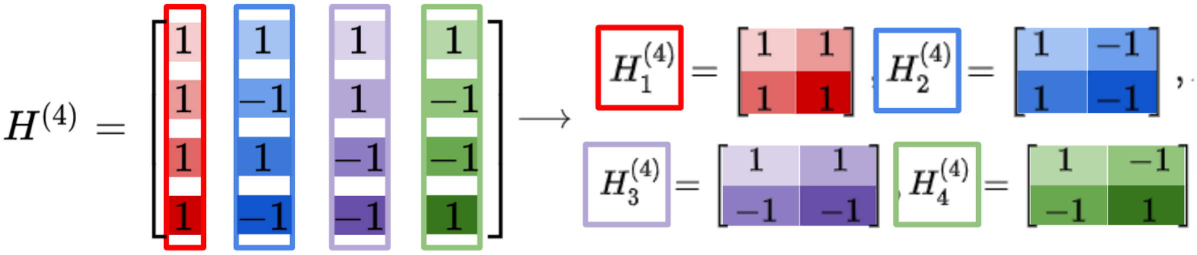

FIG. 5.6: An example of how we used the Hadamard matrix as a generator for our basis elements for a 2x2 image.

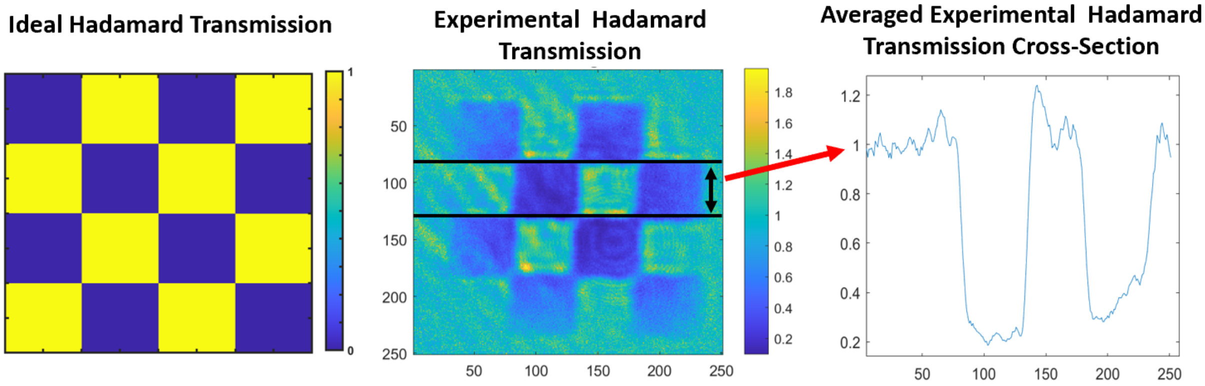

FIG. 5.7: Comparison of the ideal hadamard mode to the experimentally generated hadamard mode.

where $H_1' = [1]$. Each column of the matrix, H_{i+1}', is reshaped into a square matrix which serves as one of the basis elements for the image detection basis. Figure 5.6 shows an example for the 2x2 case.

Experimentally, we cannot generate a ”-1” on our SLM. To circumvent this technical difficulty, we generate a pair of masks ($H_\pm$) which both are tiled to be 0 and 1, but are the inverse of each other so that they subtract to equal a true Hadamard mode, $H_m = H_{m,+} - H_{m,-}$ [65]. We measure the corresponding weight for each mask and use the differential weight in the reconstruction algorithm described in Section 5.2 and 5.3.

The probe and local oscillator are then mixed on a polarizer and sent to a balanced detector. From there, the differential signal is sent to a spectrum analyzer where the quadrature noise is analyzed. A piezo-electric transducer (PZT) controllably changes the

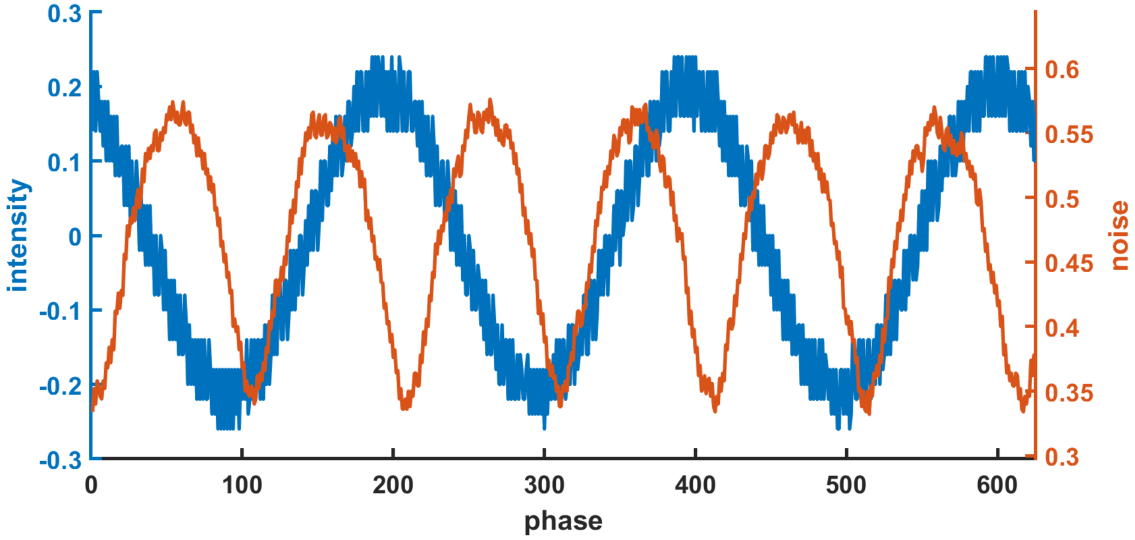

FIG. 5.8: The left axis shows how the intensity changes with phase, while the right axis shows how the noise changes with phase.

path length difference between the squeezed vacuum and the local oscillator allowing us to measure the squeezed or antisqueezed quadrature. We correct for any drift in phase by collecting a reference mask after every 100^{th} mask.

There is also a small amount of classical leakage ($5\ \mu W$) that propagates along with the squeezed vacuum. This allows us to also reconstruct the classical field using single-pixel methods described in Section 5.2 since the interference between the leakage and the local oscillator will depend on the overlap between the two. There is an extra factor of two included in the classical phase term to account for the fact the quantum phase changes as $\cos^2(\phi)$ while the classical phase changes as $\cos(\phi)$. Fig. 5.8 shows experimental measurements of the intensity (Eq. 5.4) and noise (Eq. 5.6) dependence on phase. By sweeping one arm of the interferometer, we can easily track the phase between the weak field and the local oscillator. This allows for a complete reconstruction of the classical leakage field (of course as a product with the local oscillator).

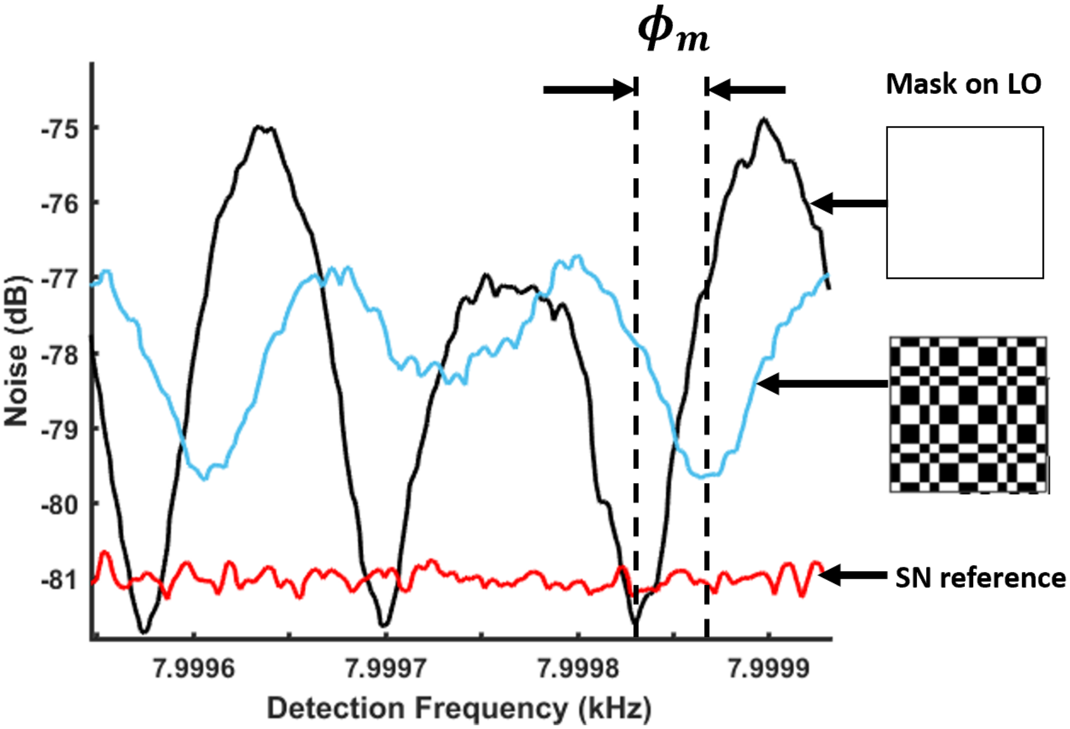

FIG. 5.9: A sample noise power trace as we sweep through the phases for an unobscured squeezed vacuum with a blank mask on the LO (black), an unobscured squeezed vacuum with an example Hadamard mask on the LO (light blue), and the shot noise level for reference (red)

5.5 Reconstructing the Squeezed Vacuum

For illustration, let us assume there are input field two modes. One that is a squeezed mode (V_1) and another a "parasitic" mode (V_2) that adds unwanted noise. With no object in the probe's path, Eq. 5.6 becomes

$$V(x,y) = 1 + (V_1 - 1)|\mathcal{O}_1(x,y)|^2 + (V_2 - 1)|\mathcal{O}_2(x,y)|^2. \tag{5.17}$$

Assuming V_1 is squeezed and V_2 is a thermal state (extra noise distributed equally in each quadrature, i.e. it is phase independent) where $max(V1) > V2 > 1$, we can explicitly write the phase dependence as,

$$V(x,y) = 1 + (V_1^{(\max)}\cos^2(\phi_1) + V_1^{(\min)}\sin^2(\phi_1) - 1)|\mathcal{O}_1(x,y)|^2 + (V_2 - 1)|\mathcal{O}_2(x,y)|^2, \tag{5.18}$$

where ϕ_1 is the phase between the local oscillator and the quantum probe, $V_{1,\max/\min}$ is the maximum/minimum noise in V_1.

As discussed in chapter 3, when there is a parasitic or contaminating mode, it does not affect the antisqueezing quadrature much, but completely overwhelms any squeezing that exists and may even push the minimum noise above the shot noise (see Fig. 3.3). This is what we observed in Fig. 5.9. When we select certain masks, we increase the overlap of the parasitic mode that distorts our squeezing. Knowing this, we can reconstruct our squeezed state by looking at the maximum and minimum noise that exists, as we sweep through our phase for different masks. Reconstructing with the maximum noise ($V^{(max)}$) will give rise to the antisqueezed noise distribution since it has been relatively uneffected by the contaminating noise mode, while using the minimum noise ($V^{(min)}$) will give the parasitic mode (if it exists) since it dominates the low noise signal. We reconstruct the quantum distribution by plugging the max or min variance measured into Eq. 5.13.

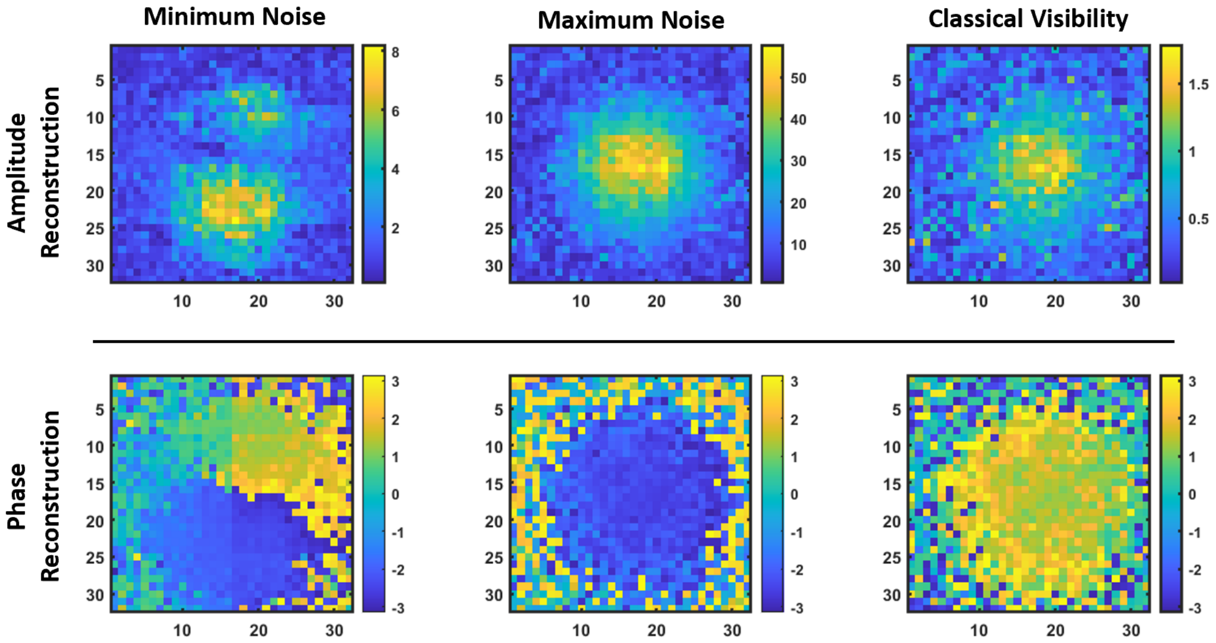

FIG. 5.10: The top row is the amplitude reconstruction of $u_{\mathrm{LO}}u_1$ (maximum noise) or $u_{\mathrm{LO}}u_2$ (minimum noise), and the bottom row is the phase reconstruction. The first column is reconstructed based on the minimum noise, the second column is reconstructed based on the maximum noise, and the third column is reconstructed based on classical interference.

Figure 5.10 shows the phase and amplitude reconstructed images based on the minimum noise, maximum noise, and classical intensity. For the minimum noise reconstruction, you can see that there are two lobes in the intensity and two distinct phases in the phase reconstruction. This looks like the HG_{01} mode. Preliminary studies of dependence on power (see Fig. 5.11 and Fig. 5.12) and temperature (see Fig. 5.13) show the parasitic mode is not strongly coupled to those specific parameters.

Much more work needs to be done to understand the origin of this parasitic mode. Key questions that are remaining include 1) is this parasitic mode squeezed at a different squeezing angle or does it follow some other noise statistics? 2) Are there other modes that we can deconvolve from our reconstructed images? While there is still much to understand about squeezed states, our novel single-pixel quantum imaging technique outline in this chapter can be a useful tool.

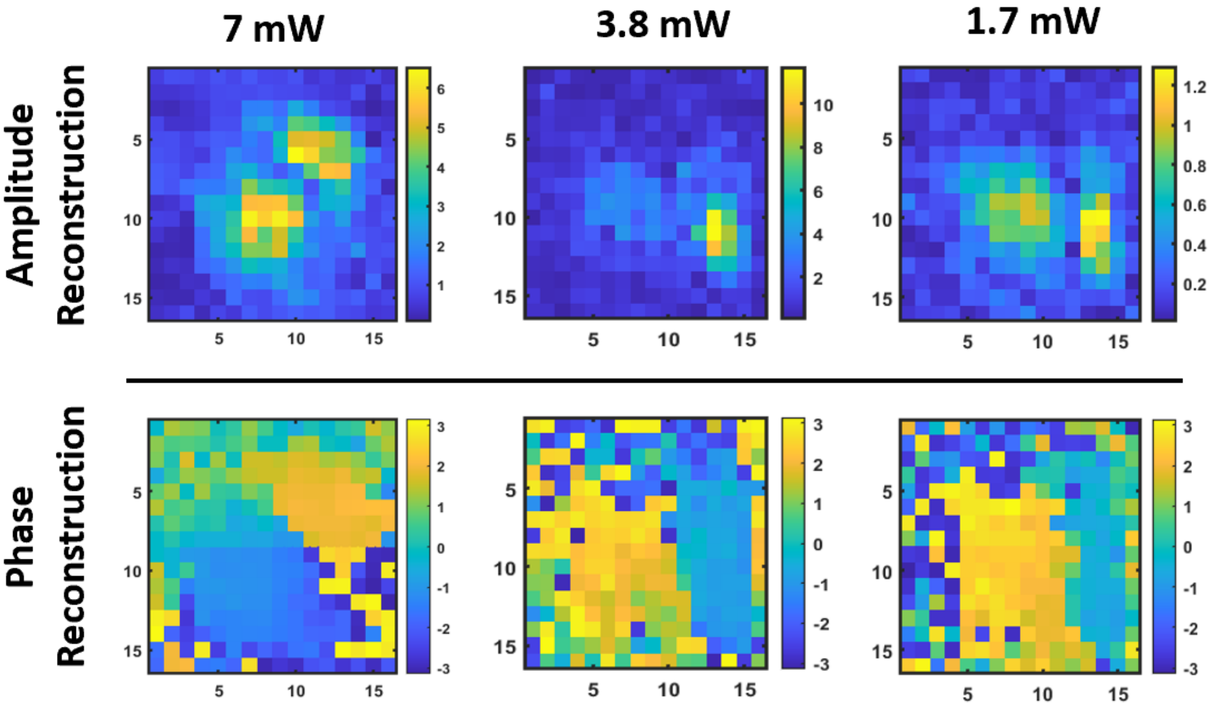

FIG. 5.11: Reconstruction of the $u_{\mathrm{LO}}u_2$ using the minimum noise as the weight for different input pump powers.

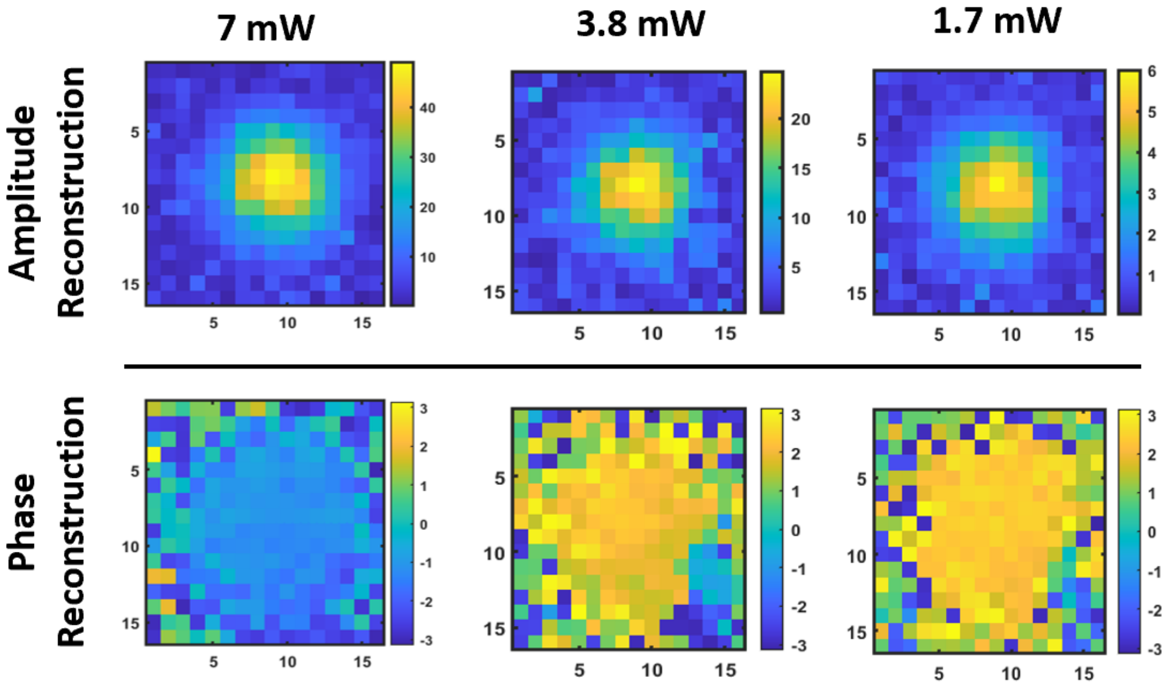
7 mW

3.8 mW

1.7 mW

Amplitude Reconstruction

Phase Reconstruction

FIG. 5.12: Reconstruction of $u_{\rm LO}u_1$ using the maximum noise as the weight for different input pump powers.

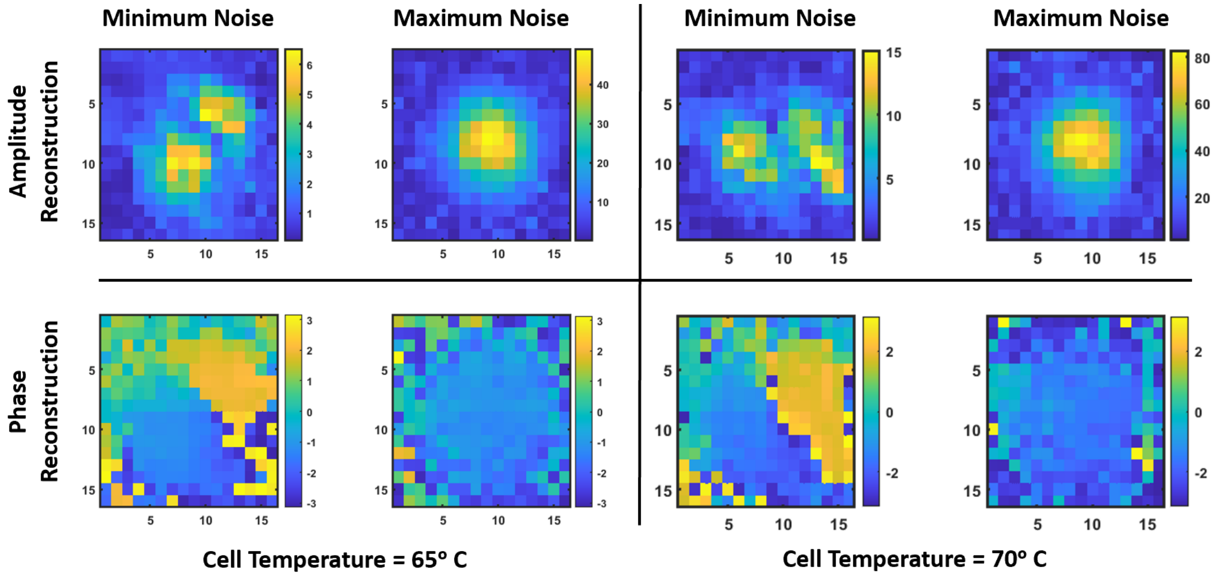
Minimum Noise

Maximum Noise

Minimum Noise

Maximum Noise

Amplitude Reconstruction

Phase Reconstruction

Cell Temperature = 65° C

Cell Temperature = 70° C

FIG. 5.13: Reconstruction of $u_{\rm LO}u_2$ or $u_{\rm LO}u_1$ using the minimum noise or maximum noise as the weight for different cell temperatures.

5.6 Image Reconstruction

In Section 5.3, we assumed complete transmission ($T(x,y) = 1$) everywhere but what if we want to reconstruct an image or scene (3D features) illuminated by the input field (i.e. the squeezed vacuum)? Assuming the single-mode squeezing case, conveniently, not much changes. We can write our input field as, $u_{in}T(x,y)$, so our overlap term becomes

$$\mathcal{O}_m \otimes T(x,y) = \sum_p u_{in}T(x,y)u_{\mathrm{LO}}H_m. \tag{5.19}$$

Our reconstruction method remains the same. We just let $u_{in} \longrightarrow u_{in}T(x,y)$ which means $\mathcal{S} \longrightarrow \mathcal{S}_{object}$ We see we are able to reconstruct the convolution of the input field, local oscillator, and scene transmission. But, if we compare the reconstruction of the field with an object in its path to the empty vacuum case, we remove the contribution from input field and local oscillator and can recover the transmission.

$$T(x,y) = \mathcal{S}_{object}/\mathcal{S} = \frac{u_{in}u_{LO}T(x,y)}{u_{in}u_{LO}}. \tag{5.20}$$

To demonstrate the method's capabilities, we imaged a phase (see Fig. 5.14) and intensity mask (see Fig. 5.15). For our sampling masks, we choose the orthonormal Hadamard modes which are commonly used for single-pixel imaging [69]. We then track the phase and maximum noise from our noise traces. Fig. 5.9 shows an example of what these noise traces look like. For the squeezed vacuum, and no mask on the local oscillator (i.e. it has its natural Gaussian shape), we can measure $\sim$ 0.7 dBs of squeezing and 6 dBs of antisqueezing. When we place a Hadamard mask onto the local oscillator, we modify the overlap term in Eq. 3.10, resulting in a different maximum and minimum noise and a different phase.

For the phase reconstruction, a simple 3-section mask with each portion containing a

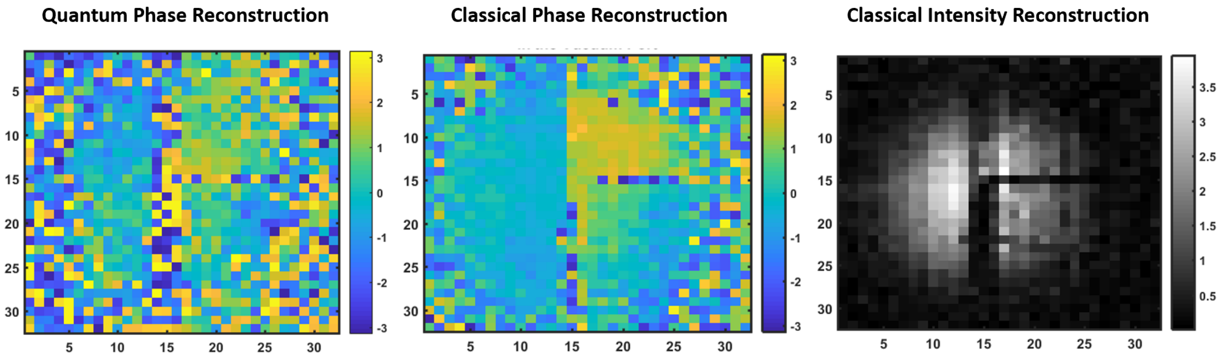
Quantum Phase Reconstruction

Classical Phase Reconstruction

Classical Intensity Reconstruction

FIG. 5.14: Left to right: quantum phase reconstruction of 3-section phase mask, and classical phase reconstruction. The z-axis denotes the phase (π, π). The final image shows the classical amplitude reconstruction of the phase mask.

different phase was placed into the center of the squeezed vacuum. We then reconstructed the intensity and phase using our classical procedure (Eq. 5.5) to have an idea of where the three-phase region was in the beam. Taking the real part of $\mathcal{S}(x, y)$ gives us the amplitude map, and taking the imaginary part gives us the phase map. To generate the quantum phase map, we follow the quantum procedure (Eq. 5.13) and look at the imaginary part. We can distinctly see the three-phase regions in both the classical and the quantum image reconstruction (see Fig. 5.14). The same procedure is used to generate the amplitude maps shown in Fig. 5.14 and Fig. 5.15. In both cases, the quantum image was sampled with approximately 10 orders of magnitude fewer photons.

5.7 Conclusion

We developed and experimentally demonstrated a proof-of-concept single-pixel imaging scheme that reconstructs a product of the input field and local oscillator. While it is not possible to reconstruct the input field alone, we do know a great deal about the local oscillator field and can make some simple claims about the object transmission we are imaging when we are in the single-mode regime. We have been able to reconstruct simple phase and intensity masks and will explore more complicated phase masks, as well as stan-

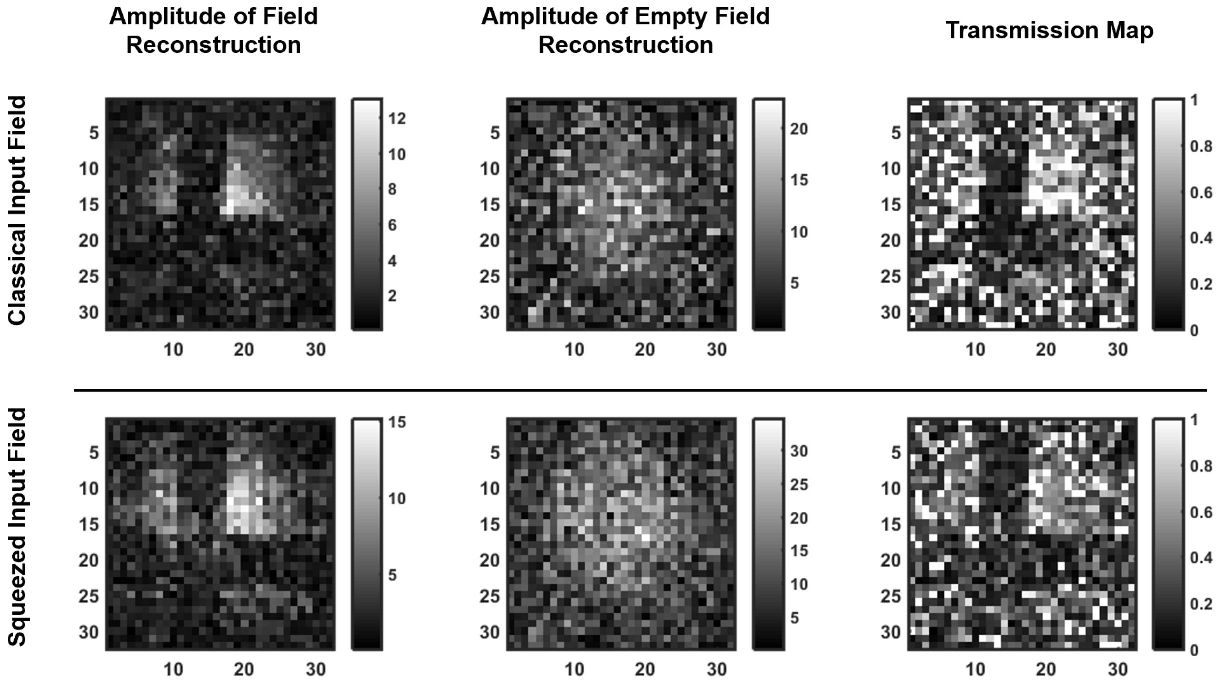

FIG. 5.15: Top row: Classical reconstruction. Bottom row: Quantum reconstruction using the antisqueezed quadrature. Left to right: amplitude reconstruction of a ”+” in the vacuum port, amplitude reconstruction of the empty vacuum port, and the transmission map generated by the ratio of the first two.

dard resolution targets to further benchmark our system again current imaging systems. Challenges that remain include laser detuning stability, interferometer phase stability, and increasing the amount of squeezing in our system for enhanced imaging results. We also want to further explore the origin of the contaminating noise mode to see how we might be able to reduce/remove it.

CHAPTER 6

Dispersion Enhanced Laser Frequency Response

Up to this point, we have only been discussing how to use the nonclassical properties of light for imaging — particularly ones that are generated using nonlinear processes in rubidium. But, using the same nonlinearities in ^{87}Rb we can also generate a host of useful light-atom interactions that can benefit the world of metrology beyond imaging. In this chapter, we will explore how four-wave mixing in ^{87}Rb can enhance lasing frequency response to cavity length changes. The following work was published in [70].

6.1 Applications of Dispersion Enhanced Lasers

We show how to control the response of the lasing frequency to the laser cavity length change on demand — allowing for either dramatic enhancement or suppression. The resonant frequency link to the cavity round trip path is the foundation for optical precision measurements such as displacement tracking, temperature sensing, optical rotation tracking [71], gravitational wave sensing [72], and refractive index change sensing [73]. In other applications, the laser provides a stable frequency reference, such as precision interferometry [74], optical atomic clocks [75], and distance ranging [76], where the sensitivity of the lasing frequency to the cavity path length change should be reduced. Our findings allow for improved laser-assisted precision metrology and potentially make lasers less bulky and immune to the environmental changes in real-world applications.

6.2 Dispersive Cavities

The addition of a dispersive medium to a cavity modifies its frequency response [77] to the geometrical path change (dp) according to

$$df_d = -\frac{n}{n_\mathrm{g}} \frac{dp}{p_\mathrm{tot}} f_0 \ , \tag{6.1}$$

where f_0 is the original resonant frequency, $p_\mathrm{tot} = p_e + p_d n$ is the total optical round-trip path of the cavity, p_d is the length of the dispersive element, p_e is the length of the empty (non-dispersive) part of the cavity, n is the refractive index, and n_g is the generalized refractive group index given by

$$n_\mathrm{g} = n + \frac{n p_d}{p_\mathrm{tot}} f_0 \frac{\partial n}{\partial f}. \tag{6.2}$$

We define the pulling factor (PF) as the ratio of dispersive to empty (non-dispersive, $n_\mathrm{g} = n$) cavity response for the same path change

$$\mathrm{PF} \equiv \frac{df_\mathrm{d}}{df_\mathrm{e}} = \frac{n}{n_\mathrm{g}}. \tag{6.3}$$

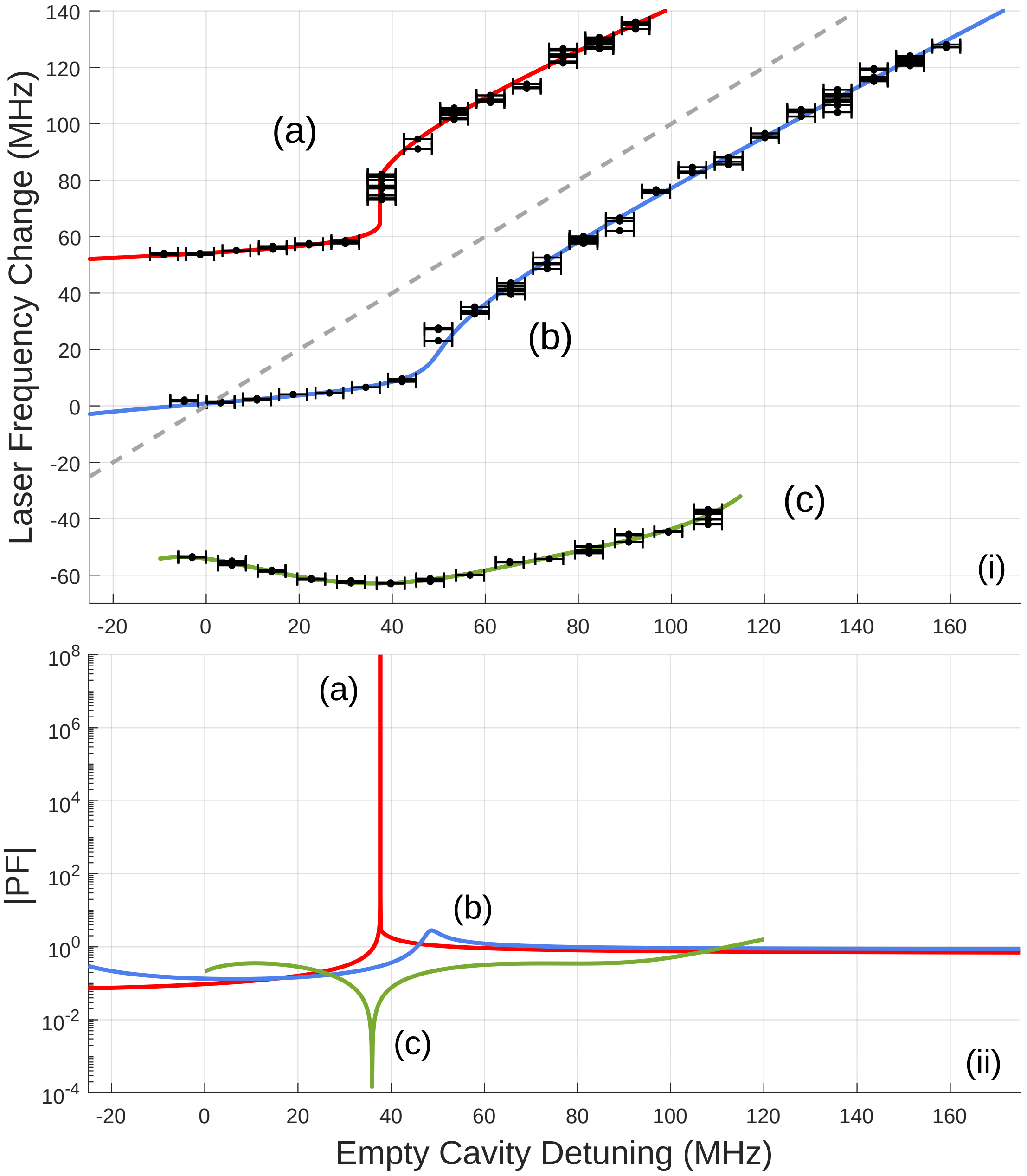

FIG. 6.1: (i) is the experimental lasing frequency dependence on empty cavity detuning (round trip path change) in (a) bifurcating regime with estimated ultra high PF$> 10^8$, (b) high pulling regime with PF$= 2.7\pm0.4$, (c) enhanced stability regime where $|\text{PF}| < 0.2$ crossing 0. The solid lines (a and b) show our best fits of the laser frequency dependence using the model described by Eq. 6.4; the (c) line is the polynomial fit of the 5th degree. The straight dashed line shows the PF$= 1$ dependence (i.e. for an empty cavity). (ii) is the PF calculated based on the fits presented in (i).

The PF is the figure of merit for the enhancement of the cavity response relative to *canonical* lasers or passive cavities operating in the weak dispersion regime with $n_\mathrm{g} = n$.

We tune the PF by several orders of magnitude in the range from -0.3 to at least 10^8 (see Fig. 6.1), by tailoring the refractive index of our lasing medium. This is the first demonstration of ultra-high and tunable PF in the laser.

Due to the Kramers-Kronig relationship the negative dispersion is accompanied by local absorption, so it is not surprising that so far the $PF > 1$ regime was experimentally demonstrated only in passive, non-lasing cavities [78, 79, 80] with PF$=363$. For active cavities, Yablon *et al.* [81] *inferred* a PF~ 190 via analysis of the lasing linewidth. The increased stability regime (PF< 1) was demonstrated in lasing [82] cavities with the smallest being PF$= 1/663$ [83]. Superradiant ("bad-cavity") lasers, where an atomic gain line is much narrower than a cavity linewidth, exhibit ultra-low PF$< 10^{-6}$ [84, 85]. Our empty cavity linewidth is about 13 MHz and the atomic gain linewidth is at least 100 MHz (see Fig. 6.1), so we operate in the "good-cavity" regime unlike work reported in [84, 85].

6.3 Theory

Similar to [86], we present a simple model of the transmission or amplification spectral line where the index of refraction has the dependence:

$$n(f) = 1 + \epsilon \frac{\gamma \Delta f}{\Delta f^2 + \gamma^2}, \tag{6.4}$$

where ϵ is the resonance strength, Δf is the detuning from the medium resonance frequency (f_m), and γ is the resonance width, since $n(f) - 1 \ll 10^{-5}$ for a vapor filled cavity. For

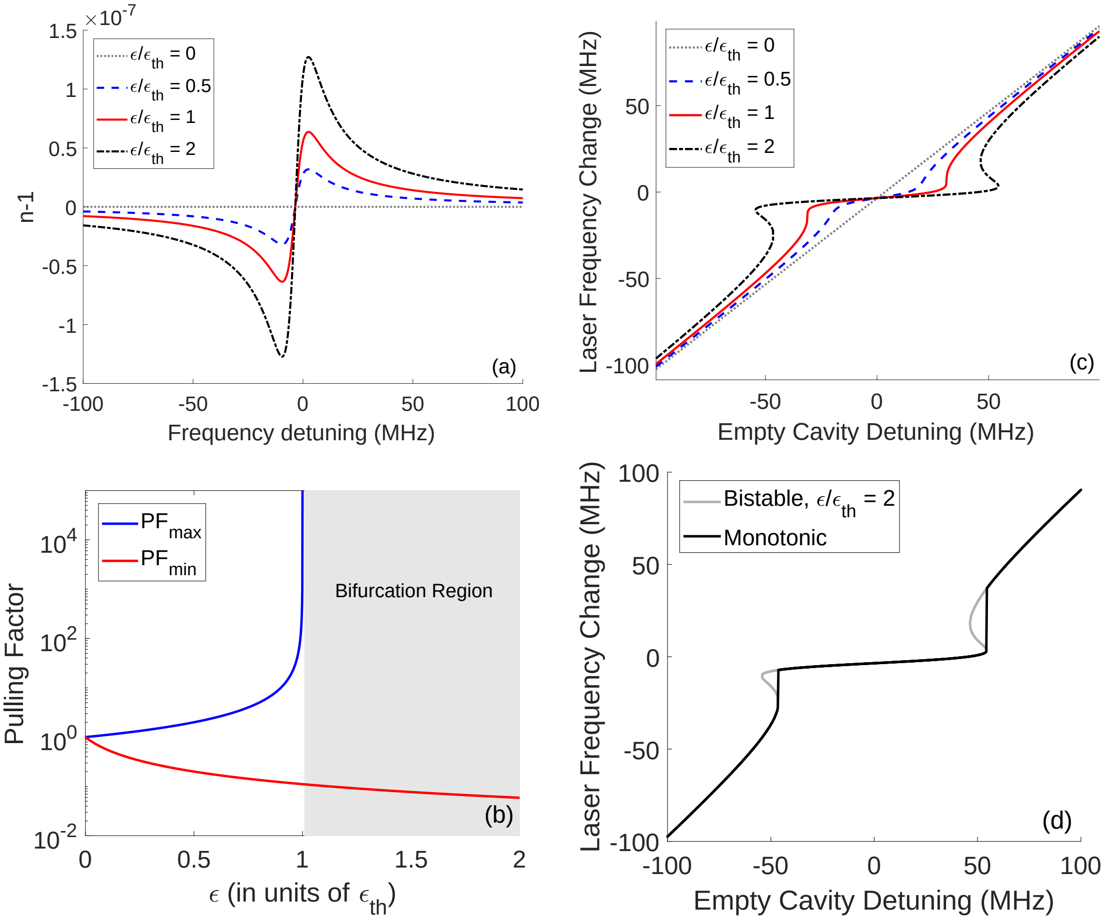

FIG. 6.2: (a) Refractive index change $(n-1)$; (b) dependence of maximum and minimal achievable PF on resonance strength; (c) laser frequency change and (d) bifurcating behavior as functions of detuning (or cavity path change). For all figures, γ is set to 6 MHz.

transmission or gain resonances with $\epsilon > 0$, the minimum and maximum PF are

$$\mathrm{PF}_{\mathrm{max}} = \frac{1}{1 - \epsilon/\epsilon_{\mathrm{th}}} \quad \text{at} \quad \Delta f = \pm\sqrt{3}\gamma, \tag{6.5}$$

$$\mathrm{PF}_{\mathrm{min}} = \frac{1}{1 + 8\epsilon/\epsilon_{\mathrm{th}}} \quad \text{at} \quad \Delta f = 0 \tag{6.6}$$

where

$$\epsilon_{\mathrm{th}} = \frac{8\gamma}{f_{\mathrm{m}}} \frac{p_{\mathrm{tot}}}{p_{\mathrm{d}}} \tag{6.7}$$

is the bifurcating threshold resonance strength.

The analysis of the dispersion (Eq. 6.4) and its influence on the resonant frequency of the cavity and PF is shown in Fig. 6.2. As expected, the amplification line has positive dispersion on resonance (see Fig. 6.2a). Positive dispersion is associated with a large and positive group index, which results in weak dependence (low pulling factor) of the lasing frequency on the cavity path change (empty cavity detuning), as shown in Fig. 6.2b. Away from resonance, the dispersion is negative leading to high PFs, as shown in Fig. 6.2b. The stronger the amplification (ϵ) the smaller the $\mathrm{PF}_{\mathrm{min}}$ is at the center of the resonance, as shown in Fig. 6.2b. Consequently, the $\mathrm{PF}_{\mathrm{max}}$ continuously grows and reaches infinity at $\epsilon = \epsilon_{\mathrm{th}}$ where the resonant frequency bifurcates (see Fig. 6.2b).

To track dependence of the cavity resonant frequency on the cavity path length, we solve:

$$p_{\mathrm{tot}} = m\frac{c}{f_d}, \tag{6.8}$$

where m is the fixed mode number and c is the speed of light in vacuum. In the experiment, it is easier to track the empty cavity detuning (i.e. resonance frequency change, Δf_{e}), which is directly linked to the cavity path change via Eq. 6.1 with $n_{\mathrm{g}} = n$. The resulting dependencies are shown in Fig. 6.2c.

If the negative dispersion is strong enough, the group index could be negative. This would lead to negative PF and to negative dependence of the lasing frequency on the cavity detuning (see line corresponding $\epsilon = 2\epsilon_{\text{th}}$ in Fig. 6.2c). This behavior is nonphysical, since it corresponds to a bifurcation [86]: multiple lasing frequencies for the same cavity detuning. Consequently, the laser would 'jump' to avoid negative PF region and preserve the monotonic behavior, as shown in Fig. 6.2d and experimentally in Fig. 6.1(i)a.

The most important conclusion from the amplifying line analysis is that high pulling (response enhancement) regions exist slightly away from the *gain* resonance. The precursor of such a regime is a reduced sensitivity region in close vicinity to the resonance. The off-resonance behavior was overlooked in the literature, while it actually provides the road to high PF. Away from the amplification resonance, the system still has enough gain to sustain lasing, and yet it still has large negative dispersion (see Fig. 6.2a). As detuning from the resonance increases, the dispersion becomes negligible, PF approaches unity (see Fig. 6.2c and experimental data in Fig. 6.1 a and b), amplification drops and eventually lasing ceases.

6.4 Experimental Setup

To experimentally demonstrate the modified lasing response to the cavity path change, one needs a narrow gain line to achieve the highest positive dispersion. We utilized the N-level pumping scheme depicted in Fig. 6.4. The theory and preliminary experimental study of this arrangement are covered in references [82, 87, 88]. The strong pumping field Ω_1 creates a transmission line for the field α due to electromagnetically induced transparency. However, the Ω_1 field alone is not enough to create the amplification. To create the gain for the α field, we apply another strong repumping field (Ω_2). There is also gain for the β

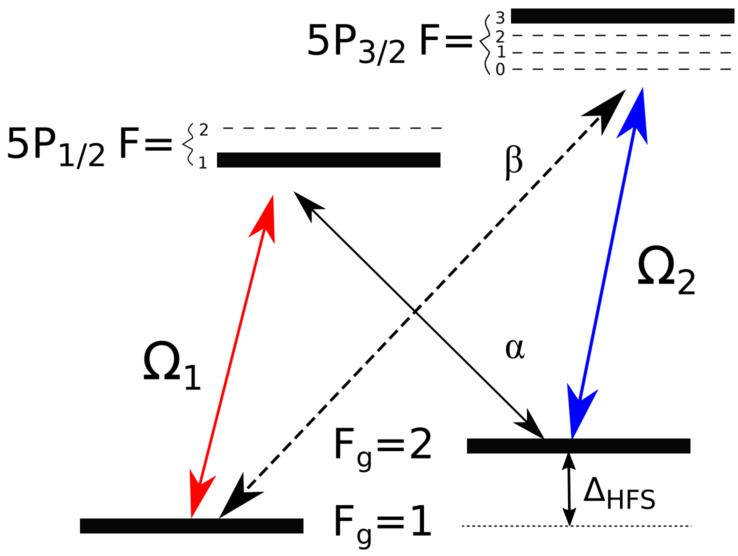

FIG. 6.3: Schematic diagram of interacting light fields and relevant ^{87}Rb levels.

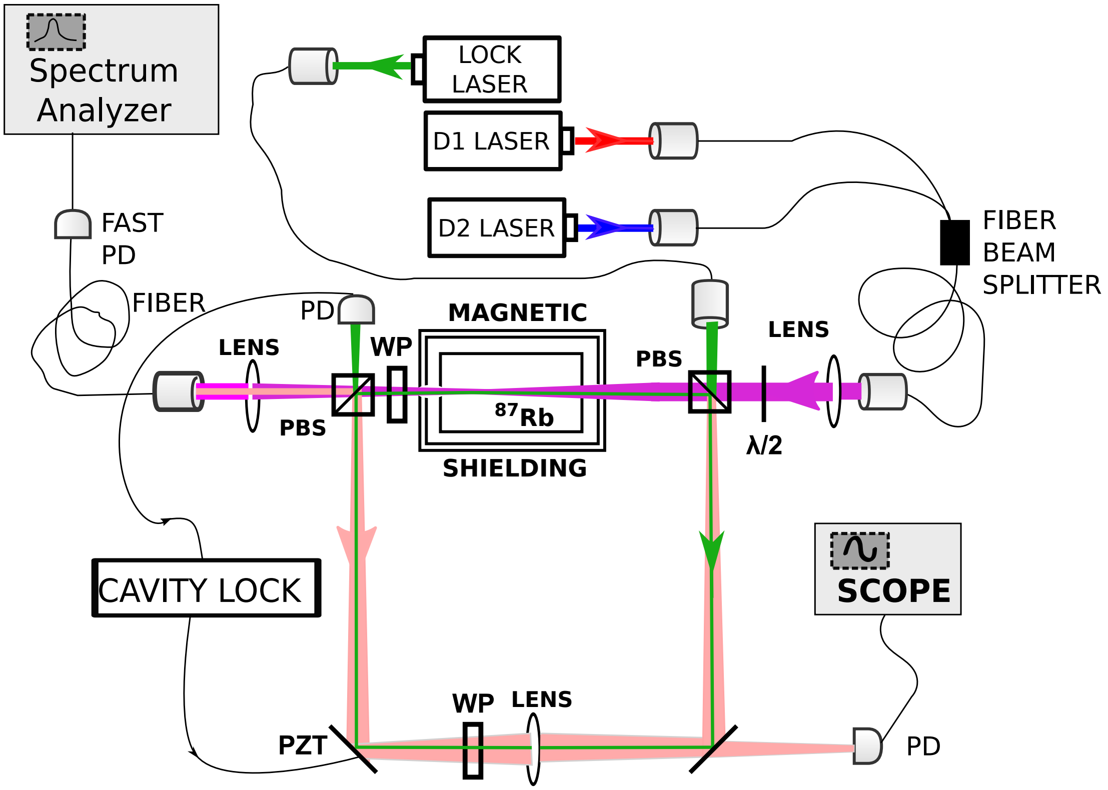

FIG. 6.4: Schematic diagram of the setup. Labels are: PD is photo detector, WP is wave plate, $\lambda/2$ is half wavelength wave plate, PBS is polarizing beam splitter, and PZT is piezoelectric transducer.

field, which completes the four-wave mixing arrangement of fields Ω_1, Ω_2, α, and β. But the cavity is tuned to sustain lasing only for α.

Our lasing cavity is similar to the one used in [82]. The ring cavity is made of two polarizing beam splitters (PBS) and two flat mirrors. The round trip path of the cavity is 80 cm. A 22 mm long Pyrex cylindrical cell with anti-reflection coatings on its windows is placed between the two PBSs and filled with isotopically pure ^{87}Rb. The cell is encased in a 3-layer magnetic shield and its temperature is set to 100 degrees C. The optical stability of the cavity is increased by adding a 30 cm focal length lens placed between the two mirrors. This lens also places the cavity's mode waist inside the ^{87}Rb cell.

To produce experimental data sets (a) and (b) shown in the Fig. 6.1, two pump lasers are tuned near D1 (795 nm) and D2 (780 nm) corresponding to Ω_1 and Ω_2 fields in Fig. 6.4. The pump fields are coupled to a fiber beam splitter and amplified by a solid-state tapered amplifier to powers ranging between 100 mW for the set (a) and 170 mW for the set (b), and then injected into a ring cavity through a polarizing beam splitter (PBS). The D1 laser is tuned 700 MHz below the $5S_{1/2}\mathrm{F_g}{=}1 \rightarrow 5P_{1/2}\mathrm{F}{=}1$ transition, and D2 is set to 500 MHz below the $5S_{1/2}\mathrm{F_g} = 2 \rightarrow 5P_{3/2}\mathrm{F}{=}3$ ^{87}Rb transition, as seen in Fig. 6.4. They provide amplification for fields α and β, which are generated orthogonal to pump fields polarization. Only the α field resonantly circulates in the cavity, since the pumps exit the cavity via the second PBS and β is kept off-resonance with the cavity.

Since the D1 pump laser is fixed, the beat note of the pump (Ω_1) and the lasing field (α) with its frequency close to ^{87}Rb hyperfine splitting ($\Delta_{\mathrm{HFS}} \approx 6.8$ GHz) is related to the frequency of the ring cavity laser and allows us to monitor the dispersive laser frequency change (Δf_d). We control the cavity length by locking it to an auxiliary laser (called the locked laser) with a wavelength of 795 nm that is far detuned from any atomic resonances and senses a "would be empty" (dispersion-free) cavity detuning (Δf_e). This lock laser beam counter propagates relatively the pump beams and the lasing field to avoid contaminating the detectors monitoring the ring cavity lasing. Two wave plates (WP) are placed inside the cavity. One is to spoil the polarization of the lock field and allow it to circulate in the cavity. The other rotates the lasing field polarization by a small amount. This allows it to exit the cavity and mix in with the pump field on the fast photodetector.

6.5 Key Results

The maximum response has the lower bound of $\mathrm{PF}_{\mathrm{max}} = 1.1 \times 10^8$ at the 90% confidence level for the data set (a), shown in Fig. 6.1. The upper bound for $\mathrm{PF}_{\mathrm{max}}$ is infinity since the data set belongs to the bifurcating regime. However, one can smoothly approach this limit by carefully controlling the cavity detuning as our analysis shows in Fig. 6.1(ii)a. The $\mathrm{PF}_{\mathrm{min}}$ range is (0.08 to 0.10) for this data set.

We can avoid bifurcation by increasing the pumps' powers (i.e., we increase γ via power broadening), as shown in the data set (b) of Fig. 6.1. This data demonstrates $\mathrm{PF}_{\mathrm{max}}$ in the range (2.3 to 3.2). Also, the range of detuning with $\mathrm{PF} > 1$ is wider. To estimate confidence bounds, we use the modified smoothed bootstrap method [89].

We are able to make our dispersive laser insensitive to its path change, as shown in data set (c) of Fig. 6.1. We tune the D1 laser to 400 MHz above the $5S_{1/2}\mathrm{F_g}{=}1 \rightarrow 5P_{1/2}\mathrm{F}{=}1$ transition, and keep D2 at 500 MHz below the $5S_{1/2}\mathrm{F_g} = 2 \rightarrow 5P_{3/2}\mathrm{F}{=}3$ ^{87}Rb transition, while maintaining combined pump power at 95 mW. Assuming a smooth dependence on the empty cavity detuning, the PF at the bottom of the U-like curve is exactly zero, as the laser frequency decreases and then increases, while the cavity path (the auxiliary laser detuning) changes monotonically. Our model governed by Eq. 6.4 cannot explain the arching behavior, since it does not account for the dependence of the dispersion on the lasing power. However, a more complete the model which solves density matrix equations of the N-level scheme predicted such a possibility [82].

There is an ongoing debate whether or not the modified cavity response leads to improved sensitivity (signal to noise ratio) of path-change sensitive detectors. However, laser-based sensors in certain applications might benefit either from enhanced PF>1 (for example gyroscopes [77]) or reduced PF<1, since sensitivity, i.e. the ratio of the response to the lasing linewidth (uncertainty), scales as 1/PF [84, 90]. The tunability and the versatility of our system allows us to probe either case.

6.6 Conclusion

In conclusion, we achieved about 10^8 increase of the laser response to the cavity-path length change relative to canonical lasers. We also can significantly reduce the response, making our laser vibration insensitive. These findings broadly impact the fields of laser sensing and metrology, including laser ranging, laser gyroscopes, and laser frequency standards.

CHAPTER 7

Conclusions and Outlook

In this dissertation, we studied how to use nonclassical states of light, squeezed light in particular, to image using very few photons. We took a more detailed look at homodyne detection, by taking into account the spatial profiles of the optical fields. This allows us to understand how to measure the spatial distribution of quantum noise. We experimentally demonstrated a way to measure squeezed light with a camera and then used the technique to image a knife-edge.

From there we expanded the method beyond the limitations of the camera by implementing a single-pixel detection scheme. Not only does this method allow us to get around functional limits imposed by a camera (like permissible probing wavelengths), but it also allows us to easily track the phase and amplitude of our quantum noise. This opens the door to 3-d imaging since objects of different depths would have our probe acquire a different phase.

Finally, we studied how to use ^{87}Rb in an optical cavity as a tunable dispersive medium. By using four-wave mixing in rubidium to generate lasing in the cavity, we were able to control the optical frequency response to cavity path length change and either make it very sensitive or completely insensitive. This work has implications for a host of optical metrology tools including: optical gyroscopes, range sensing, and temperature sensing.

Moving forward, there are many interesting questions that can be answered. With regards to imaging, further exploration is needed to understand the source and nature of contaminating noise modes as well as how the spatial modes of the squeezed state can be manipulated. In the single-pixel setup, a detailed study of how it can be implemented for 3-d imaging via phase detection and what the limits of the depth resolution are is still needed.

BIBLIOGRAPHY

[1] M. Gilaberte Basset, F. Setzpfandt, F. Steinlechner, E. Beckert, T. Pertsch, and M. Gräfe, Laser & Photonics Reviews **13**, 1900097 (2019), https://onlinelibrary.wiley.com/doi/pdf/10.1002/lpor.201900097 .

[2] Wikipedia contributors, "Transverse mode — Wikipedia, the free encyclopedia," (2021), [Online; accessed 23-February-2022].

[3] T. S. Horrom, *Experimental Generation and Manipulation of Quantum Squeezed Vacuum via Polarization Self-Rotation in Rb Vapor*, Ph.D. thesis, College of William&Mary, Williamsburg (2013).

[4] H.-A. Bachor and T. C. Ralph, *A Guide to Experiments in Quantum Optics*, 2nd ed. (Wiley-VCH, USA, 2004).

[5] C. Gerry and P. Knight, *Introductory Quantum Optics* (Cambridge University Press, 2005) pp. 152,153.

[6] M. O. Scully and M. S. Zubairy, *Quantum Optics* (Cambridge University Press, Cambridge, UK, 1997).

[7] V. Giovannetti, S. Lloyd, and L. Maccone, Science **306**, 1330 (2004), https://www.science.org/doi/pdf/10.1126/science.1104149 .

[8] J. Harms, Y. Chen, S. Chelkowski, A. Franzen, H. Vahlbruch, K. Danzmann, and R. Schnabel, Phys. Rev. D **68**, 042001 (2003).

[9] J. Aasi and *et al.*, Nature Photonics **7**, 613–619 (2013).

[10] D.-Q. Xu, X.-B. Song, H.-G. Li, D.-J. Zhang, H.-B. Wang, J. Xiong, and K. Wang, Applied Physics Letters **106**, 171104 (2015), https://doi.org/10.1063/1.4919131 .

[11] G. Lemos, V. Borish, and G. e. a. Cole, Nature **512**, 409–412 (2010).

[12] M. Genovese, Journal of Optics **18** (2016).

[13] Y. Shih, IEEE Journal of Selected Topics in Quantum Electronics **13**, 1016 (2007).

[14] R. Brown and R. Twiss, Nature **177** (1956), https://doi.org/10.1038/177027a0.

[15] R. J. Glauber, Phys. Rev. **130**, 2529 (1963).

[16] H. J. Kimble, M. Dagenais, and L. Mandel, Phys. Rev. Lett. **39**, 691 (1977).

[17] H. P. Yuen and J. H. Shapiro, Opt. Lett. **4**, 334 (1979).

[18] C. M. Caves, Phys. Rev. D **23**, 1693 (1981).

[19] D. F. Walls, Nature **306**, 141 (1983).

[20] R. E. Slusher, L. W. Hollberg, B. Yurke, J. C. Mertz, and J. F. Valley, Phys. Rev. Lett. **55**, 2409 (1985).

[21] R. M. Shelby, M. D. Levenson, S. H. Perlmutter, R. G. DeVoe, and D. F. Walls, Phys. Rev. Lett. **57**, 691 (1986).

[22] L.-A. Wu, M. Xiao, and H. J. Kimble, J. Opt. Soc. Am. B **4**, 1465 (1987).

[23] S. F. Pereira, M. Xiao, H. J. Kimble, and J. L. Hall, Phys. Rev. A **38**, 4931 (1988).

[24] R. E. Slusher, B. Yurke, P. Grangier, A. LaPorta, D. F. Walls, and M. Reid, J. Opt. Soc. Am. B **4**, 1453 (1987).

[25] C. F. McCormick, V. Boyer, E. Arimondo, and P. D. Lett, Opt. Lett. **32**, 178 (2007).

[26] V. Boyer, A. M. Marino, and P. D. Lett, Phys. Rev. Lett. **100**, 143601 (2008).

[27] M. Mehmet, S. Ast, T. Eberle, S. Steinlechner, H. Vahlbruch, and R. Schnabel, Opt. Express **19**, 25763 (2011).

[28] Y. qing Li and M. Xiao, Opt. Express **2**, 110 (1998).

[29] U. L. Andersen, T. Gehring, C. Marquardt, and G. Leuchs, Phys. Scr. **91** (2016).

[30] Y. Zhang, M. Menotti, K. Tan, and et al., Nat COmmmun **12** (2021), 10.1038/s41467-021-22540-2.

[31] H. Vahlbruch, M. Mehmet, K. Danzmann, and R. Schnabel, Phys. Rev. Lett. **117**, 110801 (2016).

[32] R. Slusher and B. Yurke, Journal of Lightwave Technology **8**, 466 (1990).

[33] A. Christ and et al, Journal of Lightwave Technology **14** (2012).

[34] A. M. Marino and C. R. Stroud, Phys. Rev. A **74**, 022315 (2006).

[35] T. G. . M. J. P. Paul-Antoine Moreau, Ermes Toninelli, Nature Review **1** (2019).

[36] H. Defienne, M. Reichert, J. W. Fleischer, and D. Faccio, Science Advances **5**, eaax0307 (2019), https://www.science.org/doi/pdf/10.1126/sciadv.aax0307 .

[37] T. Gregory, P.-A. Moreau, E. Toninelli, and M. J. Padgett, Science Advances **6** (2020), 10.1126/sciadv.aay2652.

[38] V. Boyer, A. M. Marino, R. C. Pooser, and P. D. Lett, Science **321**, 544 (2008).

[39] M. Lahiri, R. Lapkiewicz, G. B. Lemos, and A. Zeilinger, Phys. Rev. A **92**, 013832 (2015).

[40] S. Töpfer, M. G. Basset, J. Fuenzalida, F. Steinlechner, J. P. Torres, and M. Gräfe, Science Advances **8**, eabl4301 (2022), https://www.science.org/doi/pdf/10.1126/sciadv.abl4301 .

[41] S. L. Cuozzo, P. J. Barge, N. Prajapati, N. Bhusal, H. Lee, L. Cohen, I. Novikova, and E. E. Mikhailov, "Low-light shadow imaging using quantum-noise detection with a camera," (2021), arXiv:2106.00785.

[42] P. J. Barge, Z. Niu, S. L. Cuozzo, E. E. Mikhailov, I. Novikova, H. Lee, and L. Cohen, "Weak thermal state quadrature-noise shadow imaging," (2022), arXiv:2202.02231.

[43] S. M. Rochester, D. S. Hsiung, D. Budker, R. Y. Chiao, D. F. Kimball, and V. V. Yashchuk, Phys. Rev. A **63**, 043814 (2001).

[44] A. B. Matsko, I. Novikova, G. R. Welch, D. Budker, D. F. Kimball, and S. M. Rochester, Phys. Rev. A **66**, 043815 (2002).

[45] I. Novikova, A. B. Matsko, V. A. Sautenkov, V. L. Velichansky, G. R. Welch, and M. O. Scully, Opt. Lett. **25**, 1651 (2000).

[46] I. Novikova, A. B. Matsko, and G. R. Welch, Journal of Modern Optics **49**, 2565 (2002).

[47] L. Zhang, V. Boyer, and M. O. Scully, Phys. Rev. A **105**, 023725 (2022).

[48] M. Zhang, *Study of Spatial Structure of Squeezed Vacuum Field*, Ph.D. thesis, College of William&Mary, Williamsburg (2017).

[49] I. R. Berchera and I. P. Degiovanni, Metrologia **56**, 024001 (2019).

[50] C. A. Pérez-Delgado, M. E. Pearce, and P. Kok, Phys. Rev. Lett. **109**, 123601 (2012).

[51] O. Jedrkiewicz, Y.-K. Jiang, E. Brambilla, A. Gatti, M. Bache, L. A. Lugiato, and P. Di Trapani, Phys. Rev. Lett. **93**, 243601 (2004).

[52] G. Brida, L. Caspani, A. Gatti, M. Genovese, A. Meda, and I. R. Berchera, Phys. Rev. Lett. **102**, 213602 (2009).

[53] S. Walborn, C. Monken, S. Pádua, and P. Souto Ribeiro, Physics Reports **495**, 87 (2010).

[54] G. Brida, M. Genovese, A. Meda, and I. R. Berchera, Phys. Rev. A **83**, 033811 (2011).

[55] A. Kumar, H. Nunley, and A. M. Marino, Phys. Rev. A **95**, 053849 (2017).

[56] M. Edgar, D. Tasca, and F. e. a. Izdebski, Nature **3** (2012).

[57] M. W. Holtfrerich and A. M. Marino, Phys. Rev. A **93**, 063821 (2016).

[58] A. Kumar and A. M. Marino, Phys. Rev. A **100**, 063828 (2019).

[59] A. Kumar, H. Nunley, and A. M. Marino, Phys. Rev. A **98**, 043853 (2018).

[60] M. A. Taylor, J. Janousek, V. Daria, J. Knittel, B. Hage, H.-A. Bachor, and W. P. Bowen, Phys. Rev. X **4**, 011017 (2014).

[61] E. E. Mikhailov, A. Lezama, T. W. Noel, and I. Novikova, Journal of Modern Optics **56**, 1985 (2009), arXiv:0903.3156 .

[62] M. Zhang, R. N. Lanning, Z. Xiao, J. P. Dowling, I. Novikova, and E. E. Mikhailov, Phys. Rev. A **93**, 013853 (2016).

[63] M. Zhang, M. A. Guidry, R. N. Lanning, Z. Xiao, J. P. Dowling, I. Novikova, and E. E. Mikhailov, Phys. Rev. A **96**, 013835 (2017).

[64] E. S. Matekole, S. L. Cuozzo, N. Prajapati, N. Bhusal, H. Lee, I. Novikova, E. E. Mikhailov, J. P. Dowling, and L. Cohen, Phys. Rev. Lett. **125**, 113602 (2020).

[65] G. M. Gibson, S. D. Johnson, and M. J. Padgett, Opt. Express **28**, 28190 (2020).

[66] D. Donoho, IEEE Transactions on Information Theory **52**, 1289 (2006).

[67] E. J. Candes and T. Tao, IEEE Transactions on Information Theory **52**, 5406 (2006).

[68] M. F. Duarte, M. A. Davenport, D. Takhar, J. N. Laska, T. Sun, K. F. Kelly, and R. G. Baraniuk, IEEE Signal Processing Magazine **25**, 83 (2008).

[69] X. Yu, R. Stantchev, F. Yang, and et al., Sci Rep **10** (2020).

[70] S. L. Cuozzo and E. E. Mikhailov, Phys. Rev. A **100**, 023846 (2019).

[71] W. W. Chow, J. Gea-Banacloche, L. M. Pedrotti, V. E. Sanders, W. Schleich, and M. O. Scully, Rev. Mod. Phys. **57**, 61 (1985).

[72] B. P. Abbott and *et al.* (LIGO Scientific Collaboration and Virgo Collaboration), Phys. Rev. Lett. **116**, 061102 (2016).

[73] Y. X. N. Jiyang Li, Haisha Niu, Optical Engineering **56**, 050901 (2017).

[74] D. Martynov and *et al*, Phys. Rev. D **93**, 112004 (2016).

[75] A. D. Ludlow, M. M. Boyd, J. Ye, E. Peik, and P. O. Schmidt, Rev. Mod. Phys. **87**, 637 (2015).

[76] Y.-S. Jang and S.-W. Kim, Int. J. Precis. Eng. Manuf. **18**, 1881 (2017).

[77] M. S. Shahriar, G. S. Pati, R. Tripathi, V. Gopal, M. Messall, and K. Salit, Phys. Rev. A **75**, 053807 (2007).

[78] G. S. Pati, M. Salit, K. Salit, and M. S. Shahriar, Phys. Rev. Lett. **99**, 133601 (2007).

[79] D. D. Smith, H. A. Luckay, H. Chang, and K. Myneni, Phys. Rev. A **94**, 023828 (2016).

[80] D. D. Smith, H. Chang, P. F. Bertone, K. Myneni, L. M. Smith, and B. E. Grantham, Opt. Express **26**, 14905 (2018).

[81] J. Yablon, Z. Zhou, M. Zhou, Y. Wang, S. Tseng, and M. S. Shahriar, Opt. Express **24**, 27444 (2016).

[82] D. T. Kutzke, O. Wolfe, S. M. Rochester, D. Budker, I. Novikova, and E. E. Mikhailov, Opt. Lett. **42**, 2846 (2017).

[83] J. Yablon, Z. Zhou, N. Condon, D. Hileman, S. Tseng, and S. Shahriar, Opt. Express **25**, 30327 (2017).

[84] J. G. Bohnet, Z. Chen, J. M. Weiner, D. Meiser, M. J. Holland, and J. K. Thompson, Nature **484**, 78 (2012).

[85] M. A. Norcia, J. R. K. Cline, J. A. Muniz, J. M. Robinson, R. B. Hutson, A. Goban, G. E. Marti, J. Ye, and J. K. Thompson, Phys. Rev. X **8**, 021036 (2018).

[86] Z. Zhou, J. Yablon, M. Zhou, Y. Wang, A. Heifetz, and M. Shahriar, Optics Communications **358**, 6 (2016).

[87] E. E. Mikhailov, J. Evans, D. Budker, S. M. Rochester, and I. Novikova, Optical Engineering **53**, 102709 (2014).

[88] N. B. Phillips, I. Novikova, E. E. Mikhailov, D. Budker, and S. Rochester, Journal of Modern Optics **60**, 64 (2013), arXiv:1205.2567 .

[89] B. Efron and R. Tibshirani, *An Introduction to the Bootstrap* (Chapman and Hall/CRC, 1994).

[90] C. Henry, IEEE Journal of Quantum Electronics **18**, 259 (1982).

VITA

Savannah Cuozzo

Savannah was born and raised in Tampa, FL. Upon graduating high school in 2014, Savannah decided to pursue a career in physics. She attended the University of South Florida for her undergraduate studies where she completed a B.S. in physics and B.A. in mathematics. Savannah chose to pursue a Ph.D. in physics in the fall of 2017 at William & Mary, in Williamsburg, VA and conducted research in the field of experimental quantum optics under the guidence of Eugeniy Mikhailov which focused on developing quantum-enabled low-light imaging schemes. During her time at Willaim & Mary Savannah was awarded the Virginia Space Grant Consortium Graduate Fellowship to study dispersion enhanced tunablity in optical cavities. Savannah also served the Optica (formerly OSA) student chapter president for two years where she worked with fellow officers and members to organize career seminars and local outreach opportunities.